Lehigh University
Lehigh Preserve

Theses and Dissertations

1985

Edge detector performance on tomography images /

Victor Calderon
Lehigh University

Follow this and additional works at: https://preserve.lehigh.edu/etd

 Part of the Electrical and Computer Engineering Commons

Recommended Citation
Calderon, Victor, "Edge detector performance on tomography images /" (1985). *Theses and Dissertations*. 4583.
https://preserve.lehigh.edu/etd/4583

This Thesis is brought to you for free and open access by Lehigh Preserve. It has been accepted for inclusion in Theses and Dissertations by an authorized administrator of Lehigh Preserve. For more information, please contact preserve@lehigh.edu.

EDGE DETECTOR PERFORMANCE ON TOMOGRAPHY IMAGES

by

Victor Calderon

A Thesis

Presented to the Graduate Committee

of Lehigh University

in Candidacy for the Degree of

Master of Science

in

Electrical Engineering

Lehigh University

1985

This thesis is accepted and approved in partial fulfillment of the requirements for the degree of Master of Science.

Sept 15, 1985
(date)

Bruce D Fitzhenry
Professor in Charge

Eric L. Thompson
Chairman of Department

Table of Contents

Abstract 1

1. History of Tomography and Edge Detection 2

2. Tomography Project Objectives 4

3. Tomography Gauge Computer Model 5

3.1 Computer Simulation Model 5

3.2 Noise and Error 7

4. Tomography Reconstruction 12

4.1 Computer Program Description 12

4.2 Reconstruction Region 15

5. Reconstructed Images 17

6. Image Processing for Tomography 19

6.1 Edge Detection 19

6.2 Histogram 21

6.3 Contrast and Topologic Region Filtering 22

6.4 Contour Following 24

6.5 Image Restoration 26

6.6 Surface Interpolation 27

7. Experiments 28

7.1 Introduction 28

7.2 Median Filtering 29

7.3 Edge Operators 30

7.3.1 Gradient Vector 30

7.3.2 Radial Difference 30

7.3.3 Roberts 31

7.3.4 Prewitts 31

7.3.5 Multi-sized Laplacian 32

7.4 Interior Operators 32

7.4.1 Min-Max Product 32

7.4.2 Maximum Difference Operator 34

7.4.3 Chow and Kaneko 35

7.4.4 Histogram Segmentation 36

7.5 Median Filter Presmoothing 37

7.6 Experimental Results 38

8. Conclusions 43

References 45

Appendix A. Graphs of Image *i* 51

Appendix B. Graphs of Image *ii* 77

Appendix C. Graphs of Image *iii* 97

Vita 102

List of Figures

Figure A-1:	"I" Beam Without Noise	52
Figure A-2:	Histogram	53
Figure A-3:	Web Center Profile	54
Figure A-4:	Web Transaxial Profile	55
Figure A-5:	Flange Center Profile	56
Figure A-6:	Four Level Quantization	57
Figure A-7:	Web Center Profile	58
Figure A-8:	Median Filtered, 3 X 3 Window	59
Figure A-9:	Median Filtered, 5 X 5 Window	60
Figure A-10:	Median Filtered, 7 X 7 Window	61
Figure A-11:	Gradient Vector Operator	62
Figure A-12:	Histogram	63
Figure A-13:	Web Center Profile	64
Figure A-14:	Thresholded Image	65
Figure A-15:	Thresholded Web Center Profile	66
Figure A-16:	Radial Difference Operator	67
Figure A-17:	Histogram	68
Figure A-18:	Web Center Profile	69
Figure A-19:	Thresholded Image	70
Figure A-20:	Thresholded Web Center Profile	71
Figure A-21:	Roberts Operator	72
Figure A-22:	Histogram	73
Figure A-23:	Web Center Profile	74
Figure A-24:	Thresholded Image	75
Figure A-25:	Thresholded Web Center Profile	76
Figure B-1:	"I" Beam With Poisson Noise	78
Figure B-2:	Histogram	79
Figure B-3:	Web Axial Center Profile	80
Figure B-4:	Flange Axial Center Profile	81
Figure B-5:	Discrete Fourier Transform	82
Figure B-6:	Median Filtered, 3 X 3 Window	83
Figure B-7:	Web Center Profile	84
Figure B-8:	Flange Center Profile	85
Figure B-9:	Discrete Fourier Transform	86
Figure B-10:	Median Filtered, 5 X 5 Window	87
Figure B-11:	Histogram	88
Figure B-12:	Web Center Profile	89
Figure B-13:	Discrete Fourier Transform	90
Figure B-14:	Median Filtered, 9 X 9 Window	91
Figure B-15:	Discrete Fourier Transform	92
Figure B-16:	Max-Min Product Image	93
Figure B-17:	Histogram	94
Figure B-18:	Web Center Profile	95
Figure B-19:	Histogram Segmentation,Web Center Profile	96

Figure C-1: Cylinder Without Noise 98
Figure C-2: Histogram 99
Figure C-3: Diametrical Cross Section Profile 100
Figure C-4: Discrete Fourier Transform 101

Abstract

The objective of this study was to find an accurate edge locating method for sampled tomography type images. The test images were computer simulated tomography images of a steel "I" beam without photon radiation noise, an "I" beam with Poisson radiation noise injected, and a steel bar with Poisson photon noise. These images were processed by edge enhancement operators and thresholding techniques. The operators that were tried were Roberts, Radial Difference, Gradient, Maximum Difference, Unsharp Mask, and Chows. The effect of Median filter preprocessing with these operators were also investigated.

Using the aprior knowledge of object's approximate dimensions to select threshold value from image histogram proved to give the best results of tried techniques.

Chapter 1
History of Tomography and Edge Detection

The tomography formula was developed by the radioastronomer Ronald N. Bracewell in 1956 to help identify regions of the Sun which emitted microwave radiation. His integral formula was not computationally practical until the advent of the computer. Since then several different algorithms and data collection sensors have been developed for its solution. The tomography scanner has undergone five generations[1] of development. Starting from a slow single source, single detector gauge moving in discrete linear paths to a fast multiple source and multiple detector gauge rotating in a continuous circular arc.

In 1968, methods for biomolecular imaging were develop independently from earlier imaging work, using an electron microscope at various angles. In 1972, EMI LTD introduced an X-ray computer assisted tomography scanner for medical applications. By 1984, the National Institute of Health was using tomography to make a three dimensional moving image of the heart's blood reservoirs and could detect abnormal heart movement due to areas of inelastic heart tissue which cannot be diagnosised even with open heart surgery.

Image processing has been evolving steadily throughout the evolution of the computer. Because of the large amount of data that needs to be process, the computer is also a necessary tool. In 1971, M. H. Hueckel published one of the first articles on edge detection. His detector overlayed seven digital orthonormal templates on a circular pixel neighborhood to determine edge presents along with edge type and orientation. It was both time consuming and

inaccurate, but showed the potential of the field.

Today the two fields of image processing and tomography have been incorporated and have grow tremendously under the direction of the medical instrumentation industry. Now there exist equipment that can detect the three dimensional position of a brain tumor and optimally guide a surgical cryogenic probe to its location minimizing healthy tissue damage. This kind of accuracy can take an hour of processing time, but with continual hardware development, parallel array processors for example, and image algorithm research, tomography for real time industrial process control can be realized.

Chapter 2
Tomography Project Objectives

I had the privilege to work for three months on a tomography development project at Homer Research Laboratories of Bethlehem Steel Corporation. The goals set by Bethlehem Steel Corporation for their gauge were to take a cross-section image of a moving two-hundred foot rolled beam every two seconds or every thirty feet. The steel bar had to be radiated, and at the same time, detector counts from the previous radiation had to be read into the reconstruction algorithm, reconstructed and the resultant image had to be processed to extract the beams edges and dimensioned to within thirty-two thousandths of an inch. With this accomplished, a real time feedback loop can be implemented to adjust the roller spacing for process control and for total line automation.

Chapter 3
Tomography Gauge Computer Model

3.1 Computer Simulation Model

The Bethlehem Steel Corporation, Homer Research Laboratories' developed Fortran computer program was used to simulate a forth generation tomography gauge and their Fortran tomography reconstruction program to create test images. Actual gauge images were not used in experiments because gauge had recently been built and all the hardware problems had not yet been resolved. Also any gauge design parameters that experimenter might want to change would be much easier and less expensively done in computer model than on hardware. The simulated gauge was composed of a rotating, ten revolutions per minute, ring inside another stationary ring. The rotating ring had a thirty-four inch radius and was holding a thirty REM, radioactive Barium 137 source pellet, which emitted 660 KeV gamma photons. The strong intensity of the source was chosen to reduce Poisson noise associated with emission and detection of photons. The high energy of the source guarantees that no detector experiences a zero count from the source at any time no matter what the cross sectional area of the steel object. The forty-two inch radius, stationary ring held one-hundred and twenty-eight photomultiplier tubes equally spaced for gamma ray detection. Both the source and the detectors were inset into their steel rings to columnate the gamma rays to reduce Compton scattered false counts. But image blurring still occurred due to the three inch diameter, finite aperture of the columnating holes.

The output of the gauge model was a 512 x 128 two dimensional array.

The second index number was the number of photodetectors in the gauge. The first index number corresponds to the number of divisions or sampling intervals into which a one-hundred and twenty degree arc was divided. The arc was traced out when the source moved diametrically across from a detector. With an object in the gauge, the object would eclipse the source with respect to a detector and the object's shadow or photon count would be sampled and recorded in discrete arc intervals. The time averaged detector output current when the source was tracing an interval would be assigned to the source's center position in the tracing interval. Linear interpolation was then used in the reconstruction program to determine shadow values between interval centers. The average current was calculated by integrating the current verses time plot using a charging capacitor.

Therefore, there will be five-hundred and twelve shadow function samples per detector. Using the polar arc intervals centered on the ring's perimeter to sample the shadow functions for each of the one-hundred and twenty-eight detector positions, causes space-variant blurring in the reconstruction region. Imagine wheel spokes radiating outward from each of the one-hundred and twenty-eight equally spaced positions around a ring. The overlapping spokes would divide the reconstruction region into unequal-area, irregular-shaped, sampling polygons. Even though there is polar symmetry with respect to the reconstruction region's center and resolution increases as you move toward center, this necessitates the use of heuristic edge detection experimentation.

Therefore increasing either of the array's indexes would increase the resolution of the image. Once these numbers have been set, there is nothing that can be done in the reconstruction algorithm to increase this upper bound

on resolution, only reduce it.

The gauge computer model ran on an IBM 3081 using single precision variables. The steel gauge outputs its detector current to charging capacitors through a ten bit A/D converter and the two dimensional array values are assigned by a Motorola 68000 processor.

3.2 Noise and Error

Photon radiation noise was added to the individual photodetector counts in each shadow function fan increment as the last step of the gauge model. The photon noise was modeled as Poisson noise which is characteristic of both source emission noise and photomultiplier detection noise. The mean and variance of the noise was assumed to be the original count and the square root of the original count respectively. This makes the noise distribution non-stationary with respect to the other detectors and dependent on image object size. The greater the object size, the less photons will reach the detectors, so the mean and variance decrease while the percentage error increases. The net effect of all of this is that the noise will appear the greatest in the object's center and decreases as you move outward into the background area. And the larger the object, the more noise the image will contain.

For original counts less than twenty, the Poisson noise was modeled by a skewed binomial distribution. The original count was divided by one-hundred, and an interval between zero and one was divided into one-hundred sections. One-hundred trials were then run to see if a uniformly distributed random number generator, using the Power Residue Method, could fall inside the lowest section. The number of times this happened was the new assigned count. If the new count was zero, the number of trials and section size was changed by a

factor of ten. This continued until a positive count was acquired.

For counts greater than nineteen, the Poisson distribution was approximated by the normal gaussian, scaled by the square root of the original count and shifted by the original count. The central limit theory was used to created the normal gaussian by adding the results of twelve trials of the uniformly distributed random generator between zero and one. If the count was negative or zero, the process was repeated giving the method a bias error.

A subtle source of space-variant error inherent in the fourth and fifth generation gauges are partial volume effect. It is caused by the exponential equation relating the source intensity to the detector received intensity. The average received intensity while the source is tracing an interval is assumed to be the only parameter determining the average absorption density in that interval. Imagine a section of a pie with the source moving along the pie's outside arc and the detector located at the pie's vertex. Put a small object that can fit inside the pie section near the source. In this position, this object can only block or absorb a relatively small number of source photons from the detector. But as the object is moved closer to the detector, away from the source, the object can block or absorb more of the photons from the detector. Until the objects gets close enough to the pie's vertex and the detector to potential block, or absorb all the source photons from the detector. Thus even though the object's dimensions, or absorption density has not changed, it appears to the detector that it has because the detector has no way of knowing that the object was being moved. The other detectors in the gauge can help to determine if the object was moved, but not very well. Bracewell's equation requires an infinite number of detectors around the perimeter of the gauge. The

manageable number of one-hundred and twenty detector is far less than infinite. Thus this paradox in density and the uncertainty in position causes space-variant degradation. This degradation will become visible in the image when the detector values are used in the non-linear exponential radiation transmission equation which is the first step in the computer reconstruction algorithm and the error becomes magnified as it gets introduced further along in the algorithm.

Mathematically the problem is that the photon transmission equation is

$$I = I_0 * \exp(- \int u_l(x,y)\ dl)$$

where u_l is the linear attenuation coefficient. The total number of photons detected as a region is being scanned is represented by the equation

$$I_{TOTAL} = \int I\ ds = \int I_0 * \exp(-\int u_l(x,y)\ dl)\ ds$$

where ds represents the infinitesimal paths the detector and the source move together in fixed time intervals to scan a region. The average absorption density is

$$\text{Average Absorption Density} = \iint u_l(x,y)\ dl ds$$

This can be derived from the total photon count I_{TOTAL} by moving the ds integral symbol inside the exponential function and the negative sign. The average linear attenuation coefficient is derived by dividing the average absorption density by the region's area, $\iint dl ds$, but all the regions have the same area, so this reduces the division operation to a scaling function and is not done to save time. Since there is a 1-to-1 relation between the linear attenuation coefficient and the region's density in my simple single object images, the image is created by plotting absorption density values. The following average absorption density equation models the detector moving in a parallel and equal distance with the source, but in the fourth generation gauge,

the detector is stationary, giving greater weight to a delta area near the detector than the source. This error source can be remedied by paying closer attention to your differentials and transforming them into polar coordinates. This complicates reconstruction algorithm though and is not done.

Since the source and detector columnating aperture has finite area, the photon beam does not cut a planar cross-section across the object, but actually averages a slice of the object. This causes the transverse axial dimension to contribute to partial volume detector count distortion also[2].

There exist a second type of partial volume error which can cause up to a forty percent error in linear attenuation coefficient evaluation[3]. It is a result of oversimplifying an analog function when implemented in the digital domain. Two paragraphs ago it was written that the average absorption density was synthesized in the total detector count, I_{TOTAL}, equation by moving the ds integral symbol inside the exponential function. But this is mathematically incorrect because the exponential function is not linear. The rate of change of the negated exponential function increases as the input goes to zero, giving a higher weight to low value inputs than higher valued. This means the low density areas in a scanned region have a disproportionate higher influence on a region's average absorption density than high density areas. The motivation for again using a fallacy is the resulting straight forward algorithm to calculate the scan region's average absorption density from the region's detector count and the aprior source brightness whose value is always being updated. Using simple algebra

$$\text{Average Absorption Density} = -\ln\left(I_{TOTAL}/I_0\right)$$

is derived. The error can be interpret as using the region's arithmetic average

density when its weighted average density should be used.

The computer model did not modeled the image blurring caused by the beams motion through the gauge, nor did it consider the mis-assigned detector counts caused by Compton scattering.

Chapter 4
Tomography Reconstruction

4.1 Computer Program Description

The Homer Laboratories' tomography reconstruction computer program had the ability to input the detector array values generated by the actual gauge or by the gauge computer simulation program. The physical measurement that a photomultiplier tube makes is the number of photons that are transmitted through the steel beam along the line between the photon source and the tube. This is described mathematically by the equation

$$I = I_0 * \exp(- u * l)$$

where I_0 is the number of photons emitted by the source in the detector's direction along the line of length, l , where the density per unit length is u along that line. This is actually a line integral equation, written in section 3.2, summing the product of infinitesimal length intervals along the line and the interval's density. But since the steel object is assumed to have a uniform density of 1.4 and the air surrounding the object is assumed to have a density of zero, the integral reduces to the above form.

Bracewell's tomography formula[4, 5, 6] essentially says that with a multi-infinite number of line density integrals covering the region in all angular directions, this is enough information to determine the density at any point in the region. My use of the term multi-infinite is to describe that an infinite number of lines, all parallel to each other, filling a geometric plane would not be enough to satisfy the formula. All possible parallel line planes are needed where the parallel lines in one plane would be infinitesimally rotated with

respect to the parallel lines in any other plane, and all the differently constructed planes are congruent with the object's cross sectional reconstruction plane. To illustrate the point, if you placed a source and a detector diametrically across from each other on a ring's perimeter, and the ring was rotated one revolution, the line between the source and detector would cut a plane containing enough information for only the point in the ring's center to be reconstructed. It is for this reason that the high speed computer had to be invented before tomography became popular.

A fourth generation gauge attempts to get a sampling of these line integrals by viewing the object from a fixed detector and moving the radiation source behind the object so the object eclipses the source and the detector's photon readings are sampled at predetermined source positions throughout the eclipse. If the number of detector sample readings are increased, the amount of image blurring is reduced. The detector readings can be plotted to create a profile or shadow function that was casted on the detector. This function is high-pass filtered with respect to source-to-detector positioning. This filter is similar to the Laplacian. This de-emphasises the shadow's center region and gives negative values to some of the shadow's edge. This allows the shadow profiles to be backprojected across the reconstruction region and summed together, keeping track of detector geometric relationship, to give high net values to points inside the object's boundary. The algorithm used by Homer Laboratories incorporated back-projected, convoluted, Radon filtered shadow profiles. There is research going on today to mathematically manipulate Radon filtering equation so the high-pass filtering part of the algorithm can be both better implemented in the digital domain, and modified to help compensate for

the image degradation and artifacts due to the finite number of detector shadow functions used. Once again the more detectors there are, the less image blurring occurs, but also another phenomena occurs from not using the infinite number of detectors called for. The image will have artifact radiating out from the object's corners into the background region. This is caused by not having enough backprojected detector shadows which would contain negative values to reduce the artifacts height down to the background level in the summation. If their heights are not kept low enough, then they will greatly complicated the object edge finding and dimensioning processing.

So after each detectors shadow function has been filtered, any image point in the reconstruction region can be independently evaluated. All that needs to be found is the vector geometry of the image point with respect to each detector. The point's position in the detector's filtered shadow function is determined and the function's value at that position is weighted by distance between the image point and the detector. This weighted value is added to the weighted values from all the other detectors to given a net value which is assigned to that image point.

To reiterate, the maximum special resolution is determine by the number of detectors and the number of shadow function samples per detector. If either number is decreased, then the spacial resolution will decrease and using a finer image reconstruction pixel grid will not improve it. As previously stated, experimenting with the shadow function filtering operator can change artifact height, image DC value, and contrast distance between object and background, but cannot decrease the edge transition region or blur below a minimum. As an analogy, after a camera's lens blurs a photo, using finer resolution film

quality will not restore the image.

4.2 Reconstruction Region

The tomography reconstruction algorithm was modified to create a cartesian pixel grid in place of Homer Laboratories' polar pixel grid. The cartesian grid does not lose resolution as you increase the distance from the grid's center and interpolating image values between pixels is easier as opposed to the polar grid.

The reconstruction region was circular with a fifteen inch radius. A square, two hundred and fifty-seven per side, pixel grid was overlayed over the reconstruction region. This gave a resolution of 0.1167 inches between pixel centers. This created sixty-four thousand reconstruction pixels. The pixels outside the circular gauge reconstruction region were assigned zero density. These pixels plus the ones just inside the fifteen inch reconstruction region were ignored by the edge finding algorithms so the regions border edge would not interfere with the object's edge detection.

The large number of image pixels used could be circumvented by using first a much courser pixel grid, finding the object location with a crude global thresholding technique, and then calculating as many pixel values, only in the object's region, to achieve the desired resolution for accurate dimensioning. This is all contingent on the direct evaluation of Bracewell's tomography point function equation and not using an iterative reconstruction algorithm, allowing the calculation of points inside the reconstruction region to be independent of one another. An on-line image processing algorithm could be put in the program to create an adaptive resolution. This approach would greatly reduce the reconstruction and the edge finding processing times.

The pixels values were the direct solution of Bracewell's tomography equation calculated on an IBM 3081 mainframe computer using single precision.

Chapter 5
Reconstructed Images

Three test images were reconstructed for operator evaluation. They are listed below and can be viewed on pages 65, 91, and 111.

i) "I" beam with no photon Poisson noise added; flange, web, and thickness dimensions equal to 4.0, 8.0, and 1.0 inches respectively

ii) "I" beam with photon Poisson noise added; flange, wed, and thickness dimensions equal to 4.0, 8.0, and 1.0 inches respectively

iii) Bar with 3.0 inch diameter

All the images have high object slope contrast and low peak value artifacts. Global thresholding the image would have no problem identifying object. The image of the "I" beam with no noise added shows an excellent example of artifacts radiating outward and increasing in high from the object's corners seen at the four corners of the beam. The artifacts are very low due to the number of photodetectors in model. If the number were divided in half, the artifact height could increase as high as three-fourths the object's height and of coarse the object slope would decrease. The beam's flanges can be seen as right and left pillars and the web as a panel between the flanges. The "I" beam with noise added is almost the same as without noise due to the usage of a high intensity source, but it has a pillar jutting out of the middle of the web and is sightly asymmetrical while without noise image is completely symmetric with respect to the X-axis and Y-axis zero lines. The web distortion is in the object center where Poisson noise will have the greatest effect since the detector counts are the lowest from this region. The bar image is easily identifiable with artifacts radiating outward in circular symmetric fashion. Poisson noise

probably effects this image very little because of its small cross sectional size.

The histograms following each image have the characteristic bimodal distribution as expected for bilevel type images. The modals' coefficient value position are near the bilevel values of actual image, 0.0 and 1.4. The area under the modals is representative of the unequal object to background area. The variance of the background modal is three or fourth time greater due to artifacts increasing in height as they radiate outward from the step density perturbation source.

The cross sectional views of the density image can be viewed on pages 67 through 69, 93 through 94, and 113. Views 67 and 93 are along the center axis of the web. Page 68's view is of the web center transaxial cross section. Views on page 69 and 94 are along the center axis of the right flange. The flange top plateau region is bowed in the centered which is known as the "volcano" effect[7] and is due to the finite width of the photon beam. View 113 is through the center of the bar. Page 95 and 111 are the Discrete Fourier Transforms of the images which is an indication domain's coefficients.

The images hereafter will be refer to as image *i*, image *ii*, and *iii* as listed in the first paragraph.

Chapter 6
Image Processing for Tomography

6.1 Edge Detection

Most digital edge operators involve the subtraction of pixel values in a neighborhood and assign the summation of all subtractions to the neighborhood center pixel. It seems that every possible combination of adding and subtracting pixel values in a two by two and a three by three neighborhood has been tried. Many edge operator matrixes have been derived by starting with an analog function that enhances or gives high values to steep slope regions in a surface. The function is mimiced by a digital template or matrix impulse response operator with little mathematical rigor. This approach introduces image low-pass spacial filtering due to the distance between image grid samples and the size of the operator matrix.

To imitate the analog operator, the operator's impulse function is determined and then sampled to create a convolution matrix. Sometimes a one dimension function is mimiced and the resulting one dimensional vector is just repeated in the operator matrix to create a two dimensional square convoluting matrix. Or a square matrix is created by placing a vector horizontally in a matrix filled with zero's and then placing it vertically in another zero matrix. The two matrixes are then summed to create the operator matrix. A matrix template may be modified by increasing values of elements that are closer to the templates center element for two different reasons. The first reason being to give greater weight to direct, center pixel neighbors under the assumption that they have greater correlation with the center pixel than do the indirect

neighbors. And the second reason is to mold the operator matrix window function from a sharp truncated window to one whose truncation is gradual like the Gaussian, Blackman, Bartlett, etc. windows to reduce Gibb's ringing artifacts in the output image. The matrix elements may finally be scaled by a constant so the output image does not acquire an additional DC offset from the operator.

Another approach using matrixes is to use orthonormal matrixes whose element values are similar or match the values found in an ideal image window containing the feature you are searching for. These templates are also shifted across the image, but viewed as cross-correlating the template and the image. To test for each possible feature angular orientation with respect to the grid, a rotated set of templates have to cross-correlated making this approach computationally expensive. Each template will have its own output image and they will have to be combined in some fashion to generate a resultant image.

Although there are many edge detectors and processing methods[4, 5, 8], when any are used alone, none are consistently satisfactory for precision edge identification. The detectors performance is both imaging device type and image scene type dependent. The general technique of edge enhancement followed by an edge pixel selection criteria is heuristic in nature. Each method must be "tuned" by trial-and-error procedures with a set of test pictures. Usually, the resulting performance can only be measured, not predicted. The edge fitting approach, although mathematically formulated, suffers from many of the same defects. Additionally, both methods fail to cope effectively with noise. To deal with theses facts of life, using a number of better edge operators, processed in parallel, combining their outputs in a weighted sum fashion, then global

thresholding the resultant image should give excellent results. The newly developing fuzzy set theory[9, 10] may replace the weighted sum calculation if warranted or simply using a logical AND and OR operator equation on the pixel edge vote from each edge operator may be all that is necessary.

Another approach of using multiple parallel processing is to use the same detector, changing its neighborhood size, multiplying together the pixel values of each output, and then global thresholding the product image. The larger neighborhoods will be immune to short edges or artifacts, and high frequency noise. The smaller neighborhoods will not degrade the image while it is processing it, thereby retaining a sharply define edge. The amount of image low-pass filtering is directly proportional to the number of elements in the convoluting matrix. And since no filter has a perfect frequency step curve, the larger neighborhoods will be introducing further edge blurring degradation[8]. Only sharp, prominent edges will rank high under both matrix size types creating an extremely enhanced product value. By choosing a detector possessing an algorithm whose output can be piped directly into the next larger neighborhood convolution calculation, you can forego the more expensive parallel processing hardware without increasing the processing time by the power of the number of neighborhoods.

6.2 Histogram

Graphing the distribution of pixels that fall into a criteria or measurement range is used extensively in image processing. The intensity or pixel image value and some aprior knowledge about the image can be used to find a threshold value to segment the image into general features does an acceptable job for most image types.

Single object images are especially adapted to this type of processing. The gray level histogram is bimodal and by selecting a threshold value any were between the modals will give good object proximity.

Using additional processing time, histograms of different image characteristic such as X and Y coordinates, output of one or more edge operators, and a statistic measurement can be combined to form a multivariant histogram[4]. The resultant multidimensional surface may then have a peak or valley that can be identified as unique to the object and using the aprior object area, perimeter, Euclidean distance from ideal image, etc. the surface feature can be thresholded to accurately identify object location.

6.3 Contrast and Topologic Region Filtering

To fight against artifact and noise pollution in an image, the image pixels can be filtered, ignored, or flagged from any further processing at either the edge operator's input or output images.

Filtering at the image input is essentially data compression and will allow using a higher resolution pixel grid without adding process time. Several one dimensional contrast ratio test have been formulated. The most popular is Weber's Fraction[11, 12]

$$(I_1 - I_0)/I_0$$

where $I_0 < I_1$. The number of pixels separating I_0 and I_1 can be a function of imaging device bandwidth or in other words object-background spacial transition width. This will further discriminate against reconstruction artifacts which usually have much wider edge transition regions than the object's edge. Or image can be divided into regions and one region tested against the other to

identify potential regions containing an edge. This regional evaluation can be use by the tomography reconstruction point function algorithm to determine if region should be further sampled to gain finer resolution. Therefore reconstruction time would not be wasted on edgeless regions, but still allowing high resolution to important image regions.

To determine the Weber number threshold value, the image maximum and minimum can be found by coursely sampling the reconstruction pixel grid, and then taking a percentage of their difference to subtract from the maximum value to be used as I_1 and to add the percentage difference to the minimum grid value to be used as I_0. If histogram analysis is already being used on the input image, then the upper modal pixel value could be used as I_1 and the lower modal pixel value could be used as I_0 to calculate greater-than threshold value criteria.

Another pixel input selection criteria, also using the pixel intensity values, will filter out any pixels whose value does not fall in the valley region in the image's bimodal histogram. The boundaries of the selection valley can be defined by subtracting the upper and lower modal intensity values, and taking a percentage of the difference to add-to and subtract-from the lower and upper modals, respectively. This method will not filter out high peak value reconstruction artifacts, caused by using two small a number of gauge photodetectors, and whose pixel values will fall into the histogram selection valley.

After the edge operator is processed there exist another opportunity to improve edge enhancement results. The histogram of the output images can be generated and a global image threshold value can be determined by using aprior

knowledge of how many edge pixels would be in ideal object perimeter. Cumulatively adding histogram pixels, starting at high end of the graph, and stopping when a aprior value is reach will give a threshold value. The average position of all the pixels above the threshold can be found to approximate the object's center. Using aprior knowledge of size of object, an outer and depending on the object's shape an inter rectangle can be defined, where all edge pixels outside or inside rectangles, respectively, are flagged as false edges. It would only require grid row and column addresses to decide if edge pixel should be flagged. After the end of the flagging procedure, again cumulatively adding new pixels to replace the flagged ones in histogram to achieve the aprior edge count and reduce edge fragmenting which plaques simplistic global thresholding.

This last above object locating and region filtering technique can also be used on the edge operator's input image as another technique for data compression. Instead of using aprior knowledge of object's perimeter and thresholding the edge enhancement histogram, object's aprior known area is used to threshold the input image's intensity histogram. All other procedures remain the same except there will be no inter-rectangle boundary.

6.4 Contour Following

Contour following can be applied at two different steps in edge detection. It can be used after an edge operator, tracing operator's ridge peak contour. Or it can be used to search original image and draw edge contour, eliminating the need for an edge enhancement operator. There exist many curve tracing techniques which many perform viable edge finding. They possession the desirable feature of concentrating process time on only edge region and ignoring

the rest of the reconstruction region. This method suffers from many indetermine cases causing the algorithm to come to a halt. This can be remedied with sophisticated searching techniques which will increase the time cost function.

Four to eight matching template correlation tests or a $\arctan(F_y/F_x)$ function of some directional gradient operators are normally used to provide an angle, with respect to last contour branch, that the contour should proceed. Another contour searching technique is to use an edge operator that performs well when used across the entire image, demonstrating that it is robust with respect to specific noise and degradations. The operator will then be used only on pixels that are candidates to be selected as the next node in the contour path, instead of globally processed.

Another advantage of curve tracing is its ability to take advantage of the fact that the tomography reconstruction algorithm is a point function. By first performing very course pixel grid reconstruction, and then global thresholding the image. The object can be located among the artifacts by using aprior statistical values, producing a seed pixel. The object edge can be searched for with "amoeba-like" pseudo legs to test possible branch paths. The node values are image values calculated on-line with the tomography algorithm. Branch path are interpreted as object boundary. The branch length and angle with respect to last branch may be adaptive using previous found test node values, branch angles, and aprior knowledge of object shape. For instance, branch length should be short for tracing object boundary when believed to be approaching boundary corner and long when tracing boundary representing flat area on object. Testing of nodes three or fourth ahead with decision criteria can be

done before determine if a node is actually a correct choice of edge path[13, 14]. Of course the more sophisticated the adaptive and decision criteria are the slower the curve tracing will occur. But the more sophistication used, the better path-edge accuracy along with minimal image grid sampling.

By performing a histogram on image and using only middle valued pixels as total set of node candidates, a test band about the object's border will be the only pixels considered as node candidates. This will afford an extreme amount of data compression before the edge operater is used. Noise pixels that pollute the middle of the histogram will not be operated on because they will probably not be within branch decision distance of path head node. You can even go as for as doing histogram analysis on local neighborhoods of node candidates for path decision making.

6.5 Image Restoration

No images were preprocessed with any restoration techniques before edge detector for the following reasons. The driving force behind these techniques is to minimize or maximize the Mean Square Error, Schwartz's metric, Cross-Correlation, Absolute Difference, or some other pixel gray level criteria. Two concurrent pixel gray levels are compared from the actual image to some aprior ideal image. This would be useful to eliminate artifacts but not space-invariant blurring given the short preprocessing time interval. Instead of gray or intensity level examination, some metric incorporating geometric and topological properties is what is necessary to lead to precision object dimensioning. Such an approach might be to use an above mentioned intensity metric, but giving significantly greater weight to middle valued intensity pixels, which is the super set of the image's edge pixels.

6.6 Surface Interpolation

The goal of edge detectors are to locate precisely the actual object's edge, in this case, for precision object dimensioning. To do this from a digitized image requires interpolation of the edge operator output image. The interpolation process will be hampered by missing or false information in the form of smeared, fragmented, and offset edges[15]. Several surface fitting techniques were reviewed including Scan-Line Coherence, B-spline, Hermite, and Bezier in hopes that it would lead to a more precise edge location in the detector's output image for a given reconstruction grid resolution than linear interpolation affords. In the limited literature[5, 16] reviewed, nothing was found computationally fast enough worth trying, but this still leaves empirical statistical analysis to possibly improve locating object's edge between operator identified edge pixels.

Chapter 7
Experiments

7.1 Introduction

Topologically the scene that is being reconstructed and process has three parts: exterior, boundary, and interior. The operators in my experiments identified by individual pixels the boundary or the interior.

The figure of merit used to quantify operator performance was to take the number of operator identified edge pixels given that it was an edge pixel in the actual image, and ratio the count to the total number of edge pixels in the actual image, Identified/Actual. This merit measures the ability of the operator to identify actual edges correctly and is labeled Identified/Actual. The other figure of merit used was to count the number of edge pixels in actual image given that they were identified by operator, and ratio count to the total number of operator identified pixels, Actual/Identified. This merit measures false identification or operator susceptibility to noise, artifacts, and image degradation, and is labeled Actual/Identified. In the above explanation, the word edge may be replaced by interior depending on operator type. The above two ratios are transformed to percentage and added giving a perfect performance of two-hundred percent.

7.2 Median Filtering

It is no secret that edge detectors produce false edge pixels when confronted with high frequency noise. To reduce this problem the image can be pre-processed with a low-pass filter, but this blurs the image further, increasing the distance between the real and the reconstructed images.

Tukey's Median Filter 1971 technique[17, 18, 4] was chosen to be tried from the multitude of linear and non-linear filters because of consistent favorable reviews it received. Experiments show that taking the median value in a neighborhood and assigning its value to the neighborhood's center pixel blurs the objects sharp edges very little, but still does the equivalent noise reduction of other operators.

The effects of median nonlinear filtering on tomography artifacts can be seen on pages 72 through 74. The window size increases from 3 X 3, to 5 X 5, to 7 X 7 in each image *i*). For image *i*), the effects of 3 X 3, 5 X 5, and 9 X 9 windows are shown on pages 96 through 99, 100 through 103, and 104 through 105, respectively. A 9 X 9 filtering window is needed before a significant artifact reduction is achieved. The 5 X 5 filtered web center profile, page 102, compared to the original, page 93, shows no apparent slope reduction while reducing noise and artifact height. Reviewing pages 95, 99, 103, and 105 shows filter influence on all areas of the frequency domain.

Instead of using a two dimensional neighborhood template, the filter processing time can be significantly decreased by using a one dimensional neighborhood and running the filter along each pixel row and then each column. Median filtering loses very little effectiveness under this technique and its performance even improves by not rounding object corners as much[17].

7.3 Edge Operators

7.3.1 Gradient Vector

This edge operator has two convolution vectors to model the gradient in the X and then the Y direction.

1) 1 -1 2) 1

-1

It will not low-pass filter or blur the image as much as larger size operators and can be programmed for fast row and column scan processing. The Euclidean and the absolute metrics were used to combine the two vector outputs in image *i*). The Euclidean was used only on the other two images.

Page 75 is the output image of the operator on image *i* showing it sensitivity to background artifacts. Page 77 shows its relatively high peak for the web cross-section profile close to the Web's slope. Page 78 shows pixels that were identified as an edge after thresholding the edge histogram. Only the artifacts extending from the flanges are falsely identified. These could easily be identified by an object's topological metric and removed.

7.3.2 Radial Difference

1) 0 -1 0 2) 0 0 0 3) 0 0 0 4) 0 0 0

0 1 0 -1 1 0 0 1 -1 0 1 0

0 0 0 0 0 0 0 0 0 0 -1 0

The absolute values of the four resultants are added to give the operator output. The operator is effectively the pixel's gradient operator with its direct neighbors and the Euclidean metric is replace with the faster absolute value calculation. The number of pixels between the gradient elements can be

empirically increased for best results.

Graphs on page 83 and 84 and experimental results, section 7.6, show that this operator is sensitive to tomography artifacts and noise and performs poorly. Perhaps using a higher adjusted threshold value would improve results. Page 82 shows good web edge height in thresholded web center profile.

7.3.3 Roberts

1) $\begin{matrix} 1 & 0 \\ 0 & -1 \end{matrix}$ 2) $\begin{matrix} 0 & -1 \\ 1 & 0 \end{matrix}$

This operator's output is the sum of the absolute values of the two convoluting matrixes. It is basically the gradient vector run diagonally across the pixel grid. Since its operating pixels are farther apart, its low-pass cut-off frequency will be a factor of 1.4 lower than the gradient vector operator.

This operator is sensitive to artifacts from both flange and web sections of the "I" beam as seen on page 88. This operator might also perform better using a higher threshold value as can be seen on page 87 which has excellent web edge peaks.

7.3.4 Prewitts

1) $\begin{matrix} 1 & 0 & -1 \\ 1 & 0 & -1 \\ 1 & 0 & -1 \end{matrix}$ 2) $\begin{matrix} -1 & -1 & -1 \\ 0 & 0 & 0 \\ 1 & 1 & 1 \end{matrix}$

This operator has two convolution matrixes. One to detect the X component of the edge and the other for the Y component. They are the result of stretching the Gradient Vector operator and then repeating the vector to fill out a 3 X 3 matrix. Its overall performance was fifty percentage points better

than the one dimensional vector model. It identify more actual edge points. Its larger window is better adapted to the image's edge slope value.

This operator's performance was averaged. A follow up experiment would be to replace the direct neighbors with the value of two. This gives greater weight to image points closest to the assignment pixel. This is known as the Sobel operator and has good reviews[15, 19].

7.3.5 Multi-sized Laplacian

The Laplacian edge operator was not tried because of several bad reviews [20, 21, 22] it received. The algorithm which sums the one dimensional Laplacian of different size windows which are on one side of the evaluation pixel and subtracts the net of the sum of different sized Laplacians on the other side of the evaluation pixel[8] was tried. For the "I" beam image without noise, the figure of merits were both less than five percent. Good results were expected from this type of technique. Either the interpretation or the author's publication of the formula were faulty, so it was not used on any other images.

7.4 Interior Operators

7.4.1 Min-Max Product

This operator takes the minimum and maximum values in a 2 X 2 window and assigns their product to the output pixel.

By experiment it was found that this algorithm performs well for steel tomography images. The algorithm acts similar to a quantization level transformation function. Operator images are graphed on pages 106 through 109 and the coefficient values have been translated by -0.4 . Referring to the center web profiles, page 67 and 108 of image *i*), this method almost eliminates

background area artifacts and not only preserves, but increases slope value by increasing contrast.

The operator is essential the quadratic operator and its second derivative about X equal to one is the desirable characteristic. First it enhances the plateau regions by increasing the plateau height in a non-linear manner. And bilevel images are enhanced without noticing the non-linear distortion. Second, the actual image background coefficient is zero and the troublesome artifacts are mostly in the region added to the zero mean value. All artifact values of less than one will be reduced in value by their own value. Thus the smaller the pixel level, the more it will be reduced to zero which is where the majority of pixels fall. Artifacts will very rarely exceed the value of one or more than a third of the object high. Third, the artifacts or noise with negative coefficients values will be compressed the same to the zero axis and reflected about the zero axis corraling them with the positive pixels further reducing high frequency background area noise and artifact deviations. Fourth, the object transition region exceeds one and the value of one will map into itself, so the object's width will be confined and preserved. Fifth, the original image above one will be non-linearly stressed and much easier for other operators to process. And sixth, the background-object transition is usually gradually changing with the second derivative going from zero, to positive, to zero, to negative, to positive, to zero again. The quadratic operator has a linearly changing first derivative and nearly matches the image edge slope to keep output image transition interval from broading inspite of the plateau contrast increase. Coefficient values on the slope less than one, or in the positive second derivative range will be increasingly forced to zero as its input image approaches zero and coefficient

values greater than one-half will have the delta interval increasingly amplified.

A major drawback to this operator for tomography is the linear increasing slope above one or in the object plateau. Pixel noise error will be more than doubled which can be seen on pages 67 and 108. The crevasse between the flange and web triples and as stated in section 3.2, the objects interior is where Poisson noise will have the greatest percentage error. Instead of using the two extreme values in the operator window, the two other values could be used taking advantage of Median type filtering to reduce this problem.

After using the quadratic operator the image is ready for either global thresholding or edge detector processing. It may be advantageous to always translate and scale image so it falls into the desired region for processing with this quadratic type operator.

7.4.2 Maximum Difference Operator

This operator was tried on image *i*), but results were poor, 70% total, so it was not tried on any other test images because results would only get worse in the presence of noise. The minimum pixel value in a 2 X 2 window is subtracted from the maximum value in the same window[6]. This is a busyness type operator[23] that is normally used in image segmentation to find a boundary line between textured regions.

7.4.3 Chow and Kaneko

This method[24, 4] models the image intensity, in this case attenuation coefficient , histogram as two overlapping gaussian curves. A histogram segmentation threshold is chosen which minimizes the probability error of pixel object-background assignment. The threshold selection equation is

$$\text{Threshold} = (u_B+u_O)/2 + \text{STD}^2/(u_B - u_O)*\ln(P_O/P_B)$$

For the two gaussian means, the bimodal peak values were used. Usually the minimum mean squared error evaluation between the modals and possible gaussian curves are used to determine the variance parameters. It was assumed that the variances for both modals were equal and the parameter was estimated from the histogram. This was a gross simplification since the histogram for all the images, on pages 66, 92, and 112, had the lower modal twice the width as the upper modal. The variance was calculated using the actual variance of the curve to the left of the lower peak value, using the lower peak value as the mean, and the curve to the right of the upper modal peak, using the upper peak as the mean. This allowed both modals to influence the variance value. The aprior probability of background or object was assign using area ratio of actual object to reconstruction region.

The calculated threshold value fell between the aprior area count and the valley minimum in each test image giving good merit values.

7.4.4 Histogram Segmentation

This method simply plots the image absorption coefficient histogram and segments the histogram in two using some segmenting criteria. The upper histogram contains the object pixels and thresholding image with segmenting value will identify image object pixels in the bilevel image.

The histogram was quantized into three hundred and ten levels, ranging from -1.0 to +2.09. The number of quantization levels were chosen because of the simplicity of the algorithm needed to determine which level an arbitrary pixel value should be entered.

Several histogram plots have been made; see pages 66, 92, and 112, showing the expected bimodal shape of a bilevel, single object image. The image's background pixels are cumulated around the pixel absorption value of 0.0 and the object pixels are gathered around the absorption value of 1.3 and 1.4 . The background modal dwarfs the object modal due to the ratio of the object area to total pixel reconstruction grid area. Others have tried to take the Fourier Transform of the curve to exact edge information, but were not able to obtain worthwhile results.

The aprior calculation of the number of pixels that would fall inside the object boundary for a perfectly rolled object was used. Starting with the high valued pixel end of the histogram, cumulatively pixel counts were added toward the low end until the ideal count was reached.

The histogram's bimodal peaks, minimum valley, and aprior ideal pixel count have all been used for global thresholding. Also tried was the unweighted average of these. The histogram is continuously sprinkled with high frequency local peaks and valleys. Arithmetic averaging was used on the curve to create

an identifiable unique minimum between the histograms two modals. The window sizes of five and twenty-three elements were used for the "I" beam and bar histograms, respectively. The aprior area and peak values were again derived after filtering. The following values were then calculated by combining the area and valley minimum values, the two modal peak values, and the area, valley minimum, and the two modal peak values. The large filter window needed for the bar image caused erroneous results. Graphs on page 70 and 71 shows the results of quantizing the beam image into pixels 1) less than lower modal peak, 2) between lower modal peak and aprior area count threshold, 3) between aprior area count threshold and upper modal peak, and 4) greater than upper modal peak. Page 71 shows the quantized plateaus through the web center. The third highest plateau represents the web width and is accurate.

The two modal peak threshold values have equal total merit values for all the images. Therefore, there exists a maximum figure of merit threshold value between these points. It is still open for investigation to find a formula to locate this point.

7.5 Median Filter Presmoothing

A 5 X 5 widowed Median Filter was used to reduce the image noise. Pages 100 through 103 can be compared with pages 91 through 95 to qualify the amount of filtering on the "I" beam. Then the Gradient Vector, Radial Difference, Roberts, Prewitts, Multi-size Laplacian, Min-Max Product, and Chows operators were used on the test images to see if their performance would improve. Neither of the noise injected image's had significantly improved figure of merit values.

7.6 Experimental Results

The following three tables list the experimental results of the three test images. The two figure of merits described in section 7.1 are given for each operator along with the merit's quotient represented as a percentage. The two percentages are summed in the total column and a perfect score is two hundred percent. The fourth table summarizes the results from the noise injected test images of the second and third tables. The two percent totals are added to give the quantitative values and a perfect score of four hundred. These values are divide into three equal size categories of poor, average, and good to give a relative qualitative value. Also this table list the IBM 3081 virtual and real processor times in seconds it seconds it took to run the operators on the cylinder image. This indicates comparative operator processing speed, but with special hardware and algorithm recoding, times can be greatly improved.

Table 7-1: Image *i*) "I" Beam without Poisson noise

OPERATOR	IDENTIFIED/ACTUAL	I/A %	ACTUAL/IDENTIFIED	A/I %	TOTAL %
Edge Identifiers					
Gradient Vector					
Euclidean Dist	175/520	34	175/265	66	100
Absolute Value	163/520	31	163/268	61	92
Radial Diff	256/520	49	256/556	46	95
Roberts	176/520	33	176/264	67	100
Prewitts					
Euclidean Dist	288/520	55	288/518	56	111
Absolute Value	310/520	60	310/528	59	119
Multi-Laplacian	24/520	5	24/524	5	10
5x5 Median Filter					
2X2 Gradient	183/520	35	183/263	70	105
Radial Diff	302/520	58	302/514	59	117
Roberts	183/520	35	183/262	70	105
Prewitts	304/520	59	304/526	58	117
Multi-Laplacian	36/520	7	36/527	7	14
Interior Identifiers					
Min-Max Product	280/1115	25	280/280	100	25
Maximum Diff	380/1115	34	380/1071	36	70
Chows	965/1115	87	965/981	98	185
Histogram Threshold					
Object Area	993/1115	89	993/1029	97	186
Lower Peak	192/1115	17	192/192	100	117
Upper Peak	192/1115	17	192/192	100	117
Average Filter 5					
Object Area	989/1115	89	989/1025	97	186
Lower Peak	244/1115	22	244/244	100	122
Upper Peak	244/1115	22	244/244	100	122
Valley Min	731/1115	66	731/731	100	166
Area-Valley	847/1115	76	849/851	100	176
Lower-Upper	961/1115	86	961/977	98	184
Area-Low-Up-Min	871/1115	78	871/880	99	177
Median Filter					
3X3	1006/1115	90	1006/1035	97	187
5X5	1013/1115	91	1013/1037	98	189
7X7	1009/1115	91	1009/1049	96	187
5X5 Median Filter					
Min-Max Product	202/1115	18	202/202	100	118
Chows	991/1115	89	991/1001	99	188

Table 7-2: Image *ii*) "I" Beam with Poisson noise

OPERATOR	IDENTIFIED/ACTUAL	I/A %	ACTUAL/IDENTIFIED	A/I %	TOTAL %
Edge Identifiers					
Gradient Vector	161/520	31	161/260	62	93
Radial Diff	279/520	54	279/532	52	106
Roberts	169/520	33	169/260	65	98
Prewitts	303/520	58	303/518	59	117
Multi-Laplacian	14/520	3	14/526	3	6
Unsharp Mask					
3X3	3/520	1	3/593	1	2
7X7	34/520	7	34/518	7	14
9X9	41/520	8	41/521	8	16
5X5 Median Filter					
Gradient Vector	354/520	68	354/1245	28	96
Radial Diff	321/520	62	321/524	61	123
Roberts	176/520	34	176/262	67	101
Prewitts	310/520	60	310/532	58	118
Multi-Laplacian	30/520	6	30/566	5	11
Interior Identifiers					
Min-Max Product	322/1115	29	322/322	100	129
Chows	983/1115	88	983/1005	98	186
Histogram Threshold					
Object Area	983/1115	88	983/1005	98	186
Lower Peak	228/1115	20	228/228	100	120
Upper Peak	228/1115	20	228/228	100	120
Average Filter 5					
Object Area	995/1115	89	995/1033	96	185
Lower Peak	272/1115	24	272/272	100	124
Upper Peak	272/1115	24	272/272	100	124
Valley-Min	733/1115	66	733/733	100	166
Area-Valley	881/1115	79	881/885	100	179
Lower-Upper	983/1115	88	983/1003	98	186
Area-Low-Up-Min	944/1115	85	944/957	99	184
Median Filter					
3X3	1005/1115	90	1005/1029	98	188
5X5	1015/1115	91	1015/1039	98	189
7X7	1002/1115	90	1002/1029	97	187
5X5 Median Filter					
Min-Max Product	200/1115	18	200/200	100	118
Chows	1011/1115	91	1011/1033	98	189

Table 7-3: Image *iii*) Bar with Poisson noise

OPERATOR	IDENTIFIED/ACTUAL	I/A %	ACTUAL/IDENTIFIED	A/I %	TOTAL %
Edge Identifiers					
Gradient Vector	78/148	53	78/82	95	148
Radial Diff	148/148	100	148/165	90	190
Roberts	78/148	53	78/88	89	142
Prewitts	148/148	100	148/164	90	190
Unsharp Mask					
3X3	20/148	14	20/248	8	22
7X7	20/148	14	20/140	14	28
5X5 Median Filtered					
Gradient Vector	75/148	51	75/81	93	144
Radial Diff	148/148	100	148/172	86	186
Roberts	78/148	53	78/88	89	142
Prewitts	148/148	100	148/172	86	186
Interior Identifiers					
Min-Max Product	268/517	52	268/268	100	152
Chows	509/517	99	509/509	100	199
Histogram Threshold					
Object Area	517/517	100	517/527	98	198
Lower Peak	292/517	56	292/292	100	156
Upper Peak	292/517	56	292/292	100	156
Average Filter 23					
Object Area	517/517	100	517/517	100	200
Lower Peak	0/517	0	0/0	0	0
Upper Peak	0/517	0	0/0	0	0
Valley-Min	509/517	99	509/509	100	199
Area-Valley	517/517	100	517/517	100	200
Lower-Upper	505/517	98	505/505	100	198
Area-Low-Up-Min	509/517	99	509/509	100	199
Median Filter					
3X3	517/517	100	517/525	99	199
5X5	517/517	100	517/533	97	197
7X7	517/517	100	517/553	94	194
5X5 Median Filter					
Min-Max Product	256/517	50	256/256	100	150
Chows	505/517	98	505/505	100	198

Table 7-4: Summary

OPERATOR	QUANTITATIVE	QUALITATIVE	VIRTUAL/REAL
Edge Identifiers			
Gradient Vector	241	Poor	11.11/12.7
Radial Diff	296	Average	11.02/11.75
Roberts	240	Poor	10.94/11.67
Prewitts	307	Average	11.39/12.12
Unsharp Mask			
3X3	24	Poor	
7X7	42	Poor	10.85/11.90
5X5 Median Filtered			
Gradient Vector	240	Poor	
Radial Diff	309	Average	
Roberts	243	Poor	
Prewitts	304	Average	
Interior Identifiers			
Min-Max Product	281	Average	11.02/11.74
Chows	385	Good	6.28/ 7.03
Histogram Threshold			
Object Area	384	Good	
Lower Peak	276	Average	
Upper Peak	276	Average	8.29/ 8.06
Average Filter			
Object Area	385	Good	7.77/ 7.53
Lower Peak	124	Poor	9.21/ 9.00
Upper Peak	124	Poor	7.76/ 7.53
Valley-Min	365	Average	7.77/ 7.54
Area-Valley	379	Good	7.77/ 7.53
Lower-Upper	384	Good	7.78/ 7.54
Area-Low-Up-Min	383	Good	7.77/ 7.54
Median Filter			
3X3	387	Best	12.23/12.60
5X5	386	Good	28.21/28.99
7X7	381	Good	69.28/70.18
5X5 Median Filter			
Min-Max Product	268	Poor	
Chows	387	Best	

Chapter 8
Conclusions

The qualitative summary table listing clearly shows that the interior identifiers exceeded the edge identifiers. The median filter preprocessed Chow and aprior area thresholding methods gave the highest figure of merit value. It is interesting to note that the Chow and aprior area threshold method performed to within a couple of merit points on all the test images. Of the tried edge identifying operators, the three-by-three neighborhood gradient operator performed the best. It performed fifty percentage points better than the two-by-two neighborhood gradient. The filtering provided by the median filter overall had no effect on the images. Noise reduction inherent in the smaller size cylinder image improved edge and interior merit figures by fifty and twenty points, respectively. If some object aprior knowledge is available and there is little DC noise, histogram global thresholding throughout edge enhancement process is all that is needed for single object tomography images.

There exist no edge enhancement technique that can be successfully applied to any given quality image generating device along with any object image. And even more certain, there is no single edge identifying operator which is universal. You can be assured that only the best resultant images become published. Acceptable results can be achieved for a specific imaging device type when mapped to a narrowly defined set of image objects. To do this requires integrating numerous information sources involving multiple processing steps or operators.

This paper has only discussed a fraction of the proposed object finding techniques. Experiments using other techniques should be tried and compared

with these results. The better methods should then be further developed and fine tuned for tomography applictions.

References

1. Robb, R., "The Dynamic Spatial Reconstructor", *IEEE Transactions on Medical Imaging* , July , 1982 .

2. Turnier, H., Houdek, P. V., and Trefler, M. , "Measurement of the Partial Volume Phenomenon ", *Computerized Tomography* , Vol. 3 , No. 3, 1979 .

3. Herman, G. T. , *Image Reconstruction from Projections: The Fundamentals of Computerized Tomography* , Academic Press , 1980 .

4. Hall, Ernest L. , *Computer Image Processing and Recognition* , Academic Press , 1979 .

5. Pavlidis, Theodosios , *Algorithms for Graphics and Image Processing* , Computer Science Press , 1982 .

6. Brooks, R. A. and DiChiro, G. , "Principles of Computer Assisted Tomography in Radiographic and Radioisotopic Imaging ", *International Journal of Radiation Oncology Biology, Physics* , Vol. 21 , No. 5 , 1976 .

7. Joseph, P. M., Spital, R. D., and Stockham, C. D. , "The Effects of Sampling on CT Images ", *Computerized Tomography* , July-September , 1980 .

8. Davis, L. S. , "A Survey of Edge Detection Techniques ", *Computer Graphics and Image Processing*, September , 1975 .

9. Pal, S. K. and King, R. A. , "On Edge Detection of X-Ray Images Using Fuzzy Sets ", *IEEE Transactions on Pattern Analysis and Machine Intelligence*, January , 1983 .

10. Zadeh, L. A. , "Making Computers Think Like People ", *IEEE Spectrum* , August , 1984 .

11. Lipkin, B. S. and Rosenfeld, A. , *Picture Processing and Psychopictorics* , Academic Press , 1970 .

12. Griffith, A. K. , "Edge Detection in Simple Scenes Using A Priori Information ", *IEEE Transactions on Computers*, April , 1973 .

13. Martelli, A. , "An Application of Heuristic Search Methods to Edge and Contour Detection ", *Communications of the Association for Computing Machinery* , February , 1976 .

14. Kelly, M. D. , "Edge Detection in Pictures by Computer Using Planning ", *Machine Intelligence* , Vol. 6, 1971 .

15. Abdou, I. E. and Pratt, W. K., "Quantitative Design and Evaluation of Enhancement/Thresholding Edge Detectors", *Proceedings of the IEEE*,

IEEE, May 1979.

16. Foley, J. D. and Dam, A. V. , *Fundamentals of Interactive Computer Graphics* , Addison - Wesley , 1982 .

17. Narendra, P. M. , "A Separable Median Filter for Image Noise Smoothing ", *IEEE Transactions on Pattern Analysis and Machine Intelligence*, January , 1981 .

18. Chin and Yeh , "Quantitative Evaluation of Some Edge Preserving Noise-Smoothing Techniques ", *Computer Vision, Graphics, and Image Processing*, May , .

19. Pratt, William K. , *Digital Image Processing* , John Wiley & Sons , 1978 .

20. Haynes, S. M. and Jain, R. , "Detection of Moving Edges ", *Computer Vision, Graphics, and Image Processing*, March , 1983 .

21. Kasvand, T. , "Iterative Edge Detection ", *Computer Graphics and Image Processing*, September , 1975 .

22. Eberlein, R. B. and Weszka, J. S. , "Mixtures of Derivative Operators as Edge Detectors ", *Computer Graphics and Image Processing*, June , 1975 .

23. Dondes, P. A. and Rosenfeld, A., "Pixel Classification Based on Grey Level and Local " Busyness"", *IEEE Transactions on Pattern Analysis and Machine Intelligence*, January , 1982 .

24. Fritchman, B. D., "Communications Course Text ", Pages 179 - 189

25. Rabiner, L. R. and Gold, B. , *Theory and Application of Digital Signal Processing* , Prentice-Hall , 1975 .

26. Oppenheim, A. V. and Schafer, R. W. , *Digital Signal Processing* , Prentice-Hall , 1975 .

27. Aggarwal, J. K., Duda, R. O., and Rosenfeld, A. , *Computer Methods in Image Analysis* , , .

28. Cheng, Ledley, Pollock, and Rosenfeld , *Pictorial Pattern Recognition* , , .

29. McCamy, C. S. , *Evaluation and Manipulation of Photographic Images* , , .

30. Andrews, , *Computer Techniques in Image Processing* , , .

31. Henrich, G. , "A Simple Computational Method for Reducing Streak Artifacts in CT Images ", *Computerized Tomography* , Vol. 4 , No. 1, 1980 .

32. Belanger, M. G., Yasnoff, W. A., Penn, R. D., and Bacus, J. W., "Automated Scene Analysis of CT Scans ", *Computerized Tomography* , Vol. 3 , No. 3, 1979 .

33. Machuca, R. and Gilbert, A. L. , "Finding Edges in Noisy Scenes ", *IEEE Transactions on Pattern Analysis and Machine Intelligence*, January , 1981 .

34. Rosenfeld, A. , "The Max Roberts Operator is a Hueckel-Type Edge Detector ", *IEEE Transactions on Pattern Analysis and Machine Intelligence*, January , 1981 .

35. Danker, A. J. and Rosenfeld, A. , "Blob Detection by Relaxation ", *IEEE Transactions on Pattern Analysis and Machine Intelligence*, January , 1981 .

36. Zucher, S. W. and Hummel, R. A. , "A Three-Dimensional Edge Operator ", *IEEE Transactions on Pattern Analysis and Machine Intelligence*, May , 1981 .

37. Ostrem, J. S. and Falconer, D. G. , "A Differential Operator Technique for Restoring Degraded Signals and Images", *IEEE Transactions on Pattern Analysis and Machine Intelligence*, May , 1981 .

38. Morgenthaler, D. G. and Rosenfeld, A. , "Multidimensional Edge Detector by Hypersurface Fitting ", *IEEE Transactions on Pattern Analysis and Machine Intelligence*, July , 1981 .

39. Jacobus, C. J. and Chien, R. T. , "Two New Edge Detectors ", *IEEE Transactions on Pattern Analysis and Machine Intelligence*, September , 1981 .

40. Rosenfeld, A. and Smith, R. C. , "Thresholding Using Relaxation ", *IEEE Transactions on Pattern Analysis and Machine Intelligence*, September , 1981 .

41. Eklundh, J. O. and Rosenfeld, A. , "Image Smoothing Based on Neighbor Linking ", *IEEE Transactions on Pattern Analysis and Machine Intelligence*, November , 1981 .

42. Sloan, K. R. , "Analysis of "Dot Product Space" Shape Descriptions", *IEEE Transactions on Pattern Analysis and Machine Intelligence*, January , 1982 .

43. Wu, A. Y., Hong, T. H., and Rosenfeld, A. , "Threshold Selection Using Quadtrees ", *IEEE Transactions on Pattern Analysis and Machine Intelligence*, January , 1982 .

44. Udupa, J. K., Srihari, S. N., and Herman, G. T. , "Boundary Detection in Multidimensions ", *IEEE Transactions on Pattern Analysis and Machine Intelligence*, January , 1982 .

45. Elliott, H., Cooper, D. B., Cohen, F. S., and Symosek, P. F. , "Implementation Interpretation and Analysis of a Suboptimal Boundary Finding Algorithm ", *IEEE Transactions on Pattern Analysis and Machine Intelligence*, March , 1982 .

46. Abramatic, J. F. and Silverman, L. M. , "Nonlinear Restoration of Noisy Images ", *IEEE Transactions on Pattern Analysis and Machine Intelligence*, March , 1982 .

47. Gritton, C. W. and Parrish, E. A. , "Boundary Location from an Initial Plan: The Bead Chain Algorithm ", *IEEE Transactions on Pattern Analysis and Machine Intelligence*, January , 1983 .

48. Kashyap, R. L. and Oommen, B. J. , "A Geometrical Approach to Polygonal Dissimilarity and Shape Matching ", *IEEE Transactions on Pattern Analysis and Machine Intelligence*, November , 1982 .

49. Bhanu, B. and Faugeras, O. D. , "Segmentation of Images Having Unimodal Distributions ", *IEEE Transactions on Pattern Analysis and Machine Intelligence*, July , 1982 .

50. Postaire, J. G. and Vasseur, C. , "A Fast Algorithm for Nonparametric Probability Density Estimation ", *IEEE Transactions on Pattern Analysis and Machine Intelligence*, November , 1982 .

51. Cooper, D. B. and Sung, F. P. , "Multiple-Window Parallel Adaptive Boundary Finding in Computer Vision ", *IEEE Transactions on Pattern Analysis and Machine Intelligence*, May , 1983 .

52. Machuca, R. and Phillips, K. , "Applications of Vector Fields to Image Processing ", *IEEE Transactions on Pattern Analysis and Machine Intelligence*, May , 1983 .

53. Yum, Y. H. and Park, S. B. , "Optimum Recursive Filtering of Noisy Two-Dimensional Data with Sequential Parameter Identification ", *IEEE Transactions on Pattern Analysis and Machine Intelligence*, May , 1983 .

54. Shneier, M. , "Using Pyramids to Define Local Thresholds for Blob Detection ", *IEEE Transactions on Pattern Analysis and Machine Intelligence*, May , 1983 .

55. Mohammed, J. L., Hummel, R. A., and Zucker, S. W. , "A Gradient Projection Algorithm for Relaxation Methods ", *IEEE Transactions on Pattern Analysis and Machine Intelligence*, May , 1983 .

56. Chen, T. C. and DeFigueiredo, R. J. , "An Image Transform Coding Scheme Based On Spatial Domain Considerations ", *IEEE Transactions on Pattern Analysis and Machine Intelligence*, May , 1983 .

57. Nagel, H. H. , "Displacement Vectors Derived from Second-Order Intensity Variations in Image Sequences ", *Computer Vision, Graphics,*

and Image Processing, January , 1983 .

58. , "Edge Detection Using Sliding Statistical Tests ", *Computer Vision, Graphics, and Image Processing*, July , 1983 .

59. Shannon, W. A., Rockholt, D. L., and Bates, S. B. , "Computer-assisted Measurement of the Thickness of Biological Structures ", *Computers in Biology and Medicine* , Vol. 12 , No. 2 , 1982 .

60. Weszka, J. S. , "A Survey of Threshold Selection Techniques ", *Computer Graphics and Image Processing*, April , 1978 .

61. Gray, S. B. , "Local Properties of Binary Images in Two Dimensions ", *IEEE Transactions on Computers*, May , 1971 .

62. Rosenfeld, A. and Thurston, M. , "Edge and Curve Detection for Visual Scene Analysis ", *IEEE Transactions on Computers*, May , 1971 .

63. Burt, P. J. , "Fast Algorithms for Estimating Local Image Properties ", *Computer Vision, Graphics, and Image Processing*, March , 1983 .

64. Nahi, N. E. and Jahanshahi, M. H. , "Image Boundary Estimation ", *IEEE Transactions on Computers*, August , 1977 .

65. Paton, K. , "Picture Description Using Legendre Polynomials ", *Computer Graphics and Image Processing*, March , 1975 .

66. Ramer, U. , "Extraction of Line Structures from Photographs of Curved Objects ", *Computer Graphics and Image Processing*, June , 1975 .

67. Fram, J. R. and Deutsch, E. S. , "On the Quantitative Evaluation of Edge Detection Schemes and Their Comparison with Human Performance ", *IEEE Transactions on Computers*, June , 1975 .

68. Nahi, N. E. and Lopez-Mora, S. , "Estimation-Detection of Boundaries in Noisy Images ", *IEEE Transactions on Automatic Control* , October , 1978 .

69. Thrift, P. R. and Dunn, S. M. , "Approximating Point-Set Images by Line Segments Using a Variation of the Hough Transform ", *Computer Vision, Graphics, and Image Processing*, March , 1983 .

70. Gil, B., Mitiche, A., and Aggarwal, J. K. , "Experiments in Combining Intensity and Range Edge Maps ", *Computer Vision, Graphics, and Image Processing*, March , 1983 .

71. Hildreth, E. C. , "Detection of Intensity Changes by Computer and Biological Vision Systems ", *Computer Vision, Graphics, and Image Processing*, April , 1983 .

72. Haralick, R. M. , "Ridges and Valleys on Digital Images ", *Computer Vision, Graphics, and Image Processing*, April , 1983 .

73. Grimson, W. E. , "An Implementation of a Computational Theory of Visual Surface Interpolation ", *Computer Vision, Graphics, and Image Processing*, April , 1983 .

74. Brady, M. and Horn, B. K. , "Rotationally Symmetric Operators for Surface Interpolation ", *Computer Vision, Graphics, and Image Processing*, April , 1983 .

75. Lawton, D. T. , "Processing Translational Motion Sequences ", *Computer Vision, Graphics, and Image Processing*, April , 1983 .

76. Kulpa, Z. , "More About Areas and Perimeters of Quantized Objects ", *Computer Vision, Graphics, and Image Processing*, May , 1983 .

77. Therrien, C. W. , "An Estimation-Theoretic Approach to Terrain Image Segmentation ", *Computer Vision, Graphics, and Image Processing*, June , 1983 .

78. Franklin, W. R. , "Rays-New Representation for Polygons and Polyhedra ", *Computer Vision, Graphics, and Image Processing*, June , 1983 .

79. Mitiche, A. and Aggarwal, J. K. , "Contour Registration by Shape-Specific Points for Shape Matching ", *Computer Vision, Graphics, and Image Processing*, June , 1983 .

80. Smith, M. W. and Davis, W. A. , "A New Algorithm for Edge Detection ", *Computer Graphics and Image Processing*, March , 1975 .

81. Hueckel, M. H. , "An Operator Which Locates Edges in Digitized Pictures ", *Journal of the Association for Computing Machinery* , January , 1971 .

82. Duda, R. O. and Hart, P. E. , "Use of the Hough Transformation to Detect Lines and Curves in Pictures ", *Communications of the Association for Computing Machinery* , January , 1972 .

83. Freeman, H. , "On the Encoding of Arbitrary Geometric Configurations ", *IRE Transactions on Electronic Computers* , June , 1961 .

84. Granlund, G. H. , "Fourier Preprocessing for Hand Print Character Recognition ", *IEEE Transactions on Computers* , February , 1972 .

85. Robert, L. G. , "Machine Perception of Three-Dimensional Solids ", *Optical and Electro - Optical Information Processing* , 1965 , pp. 159-197.

86. Brice, C. R. and Fennema, C. L. , "Scene Analysis Using Regions ", *Artificial Intelligence* , Vol. 1 , 1970.

Appendix A
Graphs of Image i

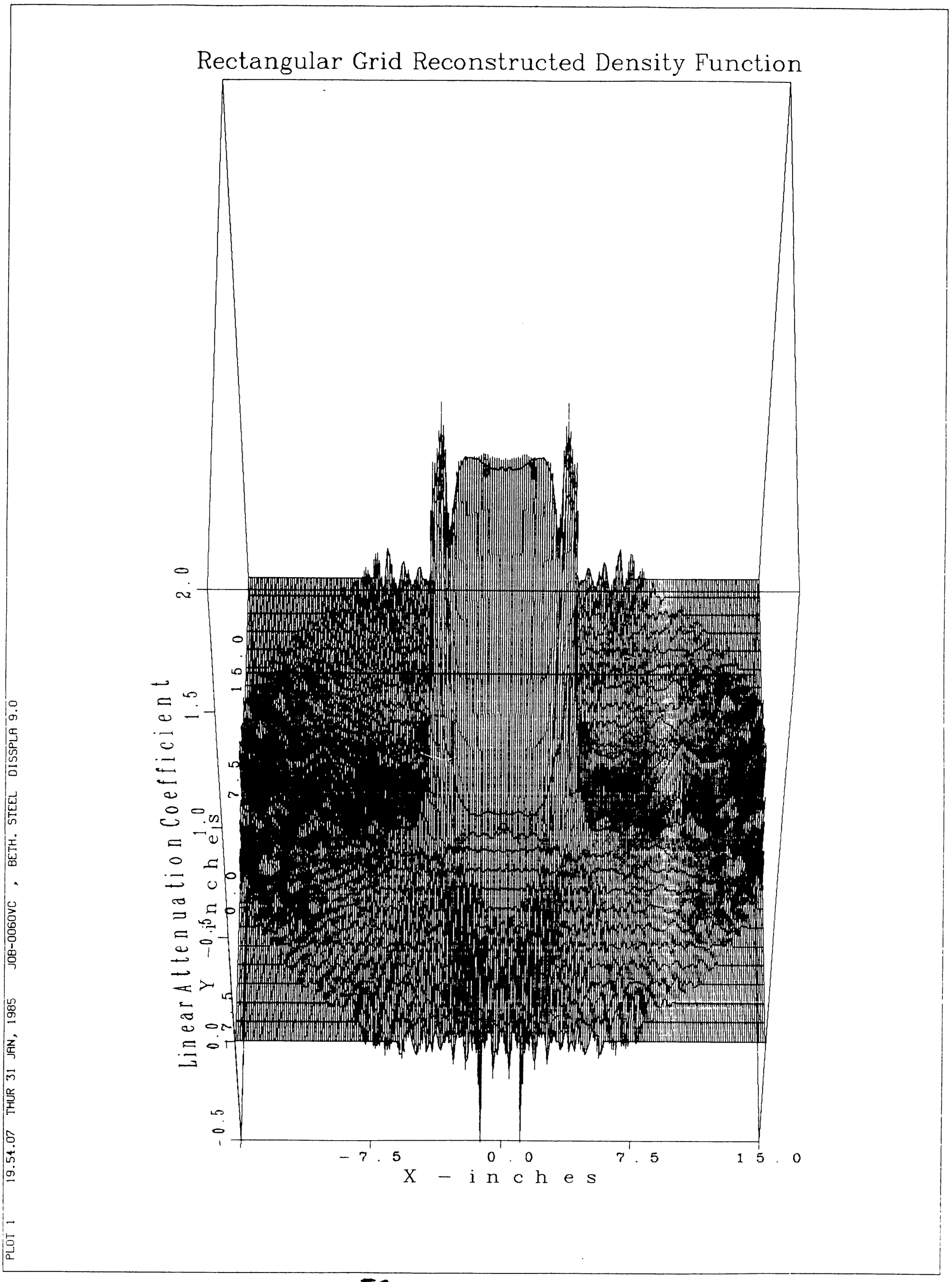
Rectangular Grid Reconstructed Density Function
Linear Attenuation Coefficient
0.0 Y -0.5 inches 1.0
1.5
2.0
0
-0.5
-7.5
0.0
7.5
15.0
X - inches
PLOT 1 19.54.07 THUR 31 JAN, 1985 JOB-0060VC , BETH. STEEL DISSPLA 9.0

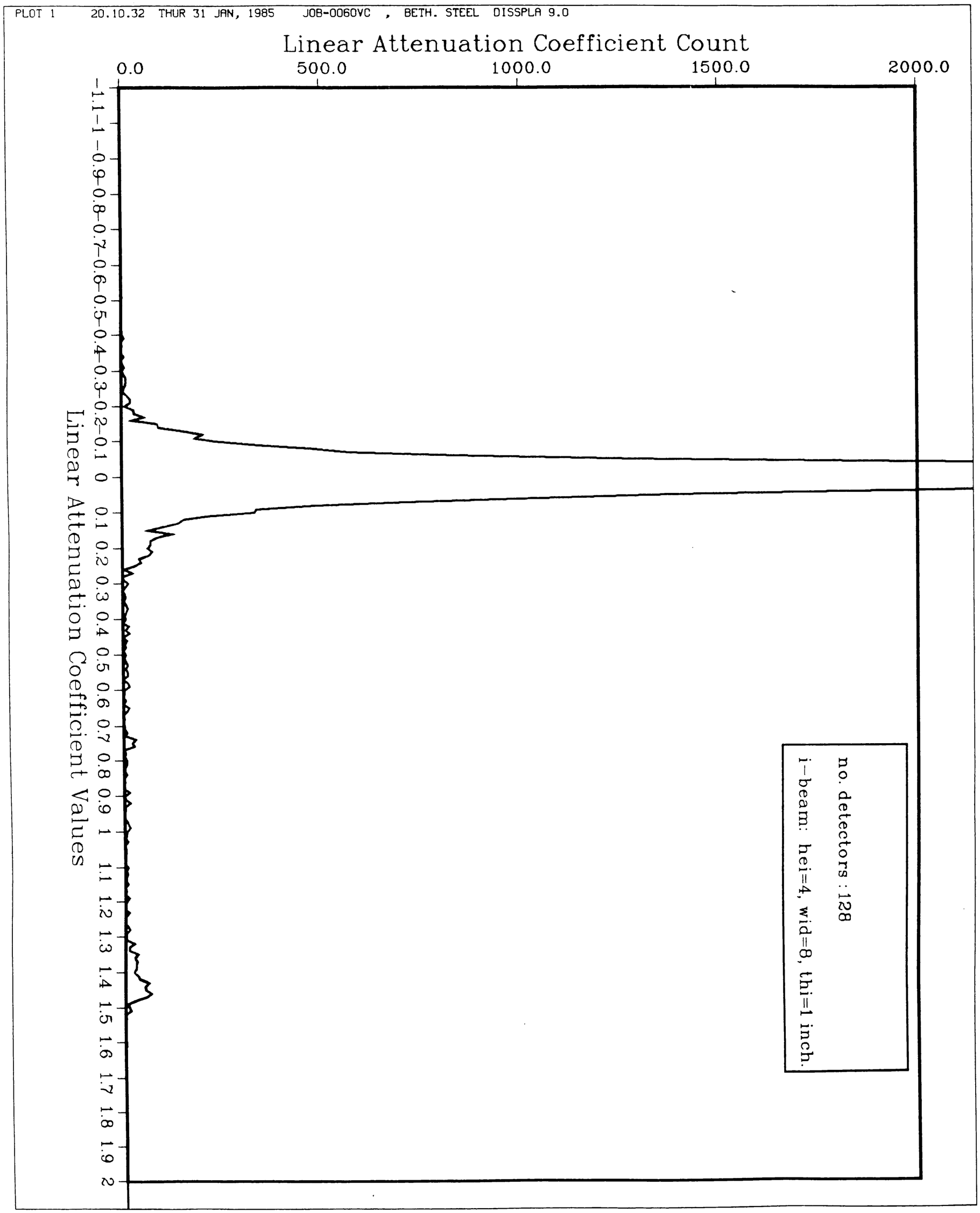
PLOT 1 20.10.32 THUR 31 JAN, 1985 JOB-0060VC , BETH. STEEL DISSPLA 9.0
Linear Attenuation Coefficient Count
0.0
500.0
1000.0
1500.0
2000.0
-1.1 -1 -0.9 -0.8 -0.7 -0.6 -0.5 -0.4 -0.3 -0.2 -0.1 0 0.1 0.2 0.3 0.4 0.5 0.6 0.7 0.8 0.9 1 1.1 1.2 1.3 1.4 1.5 1.6 1.7 1.8 1.9 2
Linear Attenuation Coefficient Values
no. detectors :128
i-beam: hei=4, wid=8, thi=1 inch.

PLOT 1 20.46.45 THUR 31 JAN, 1985 JOB-0060VC , BETH. STEEL DISSPLA 9.0

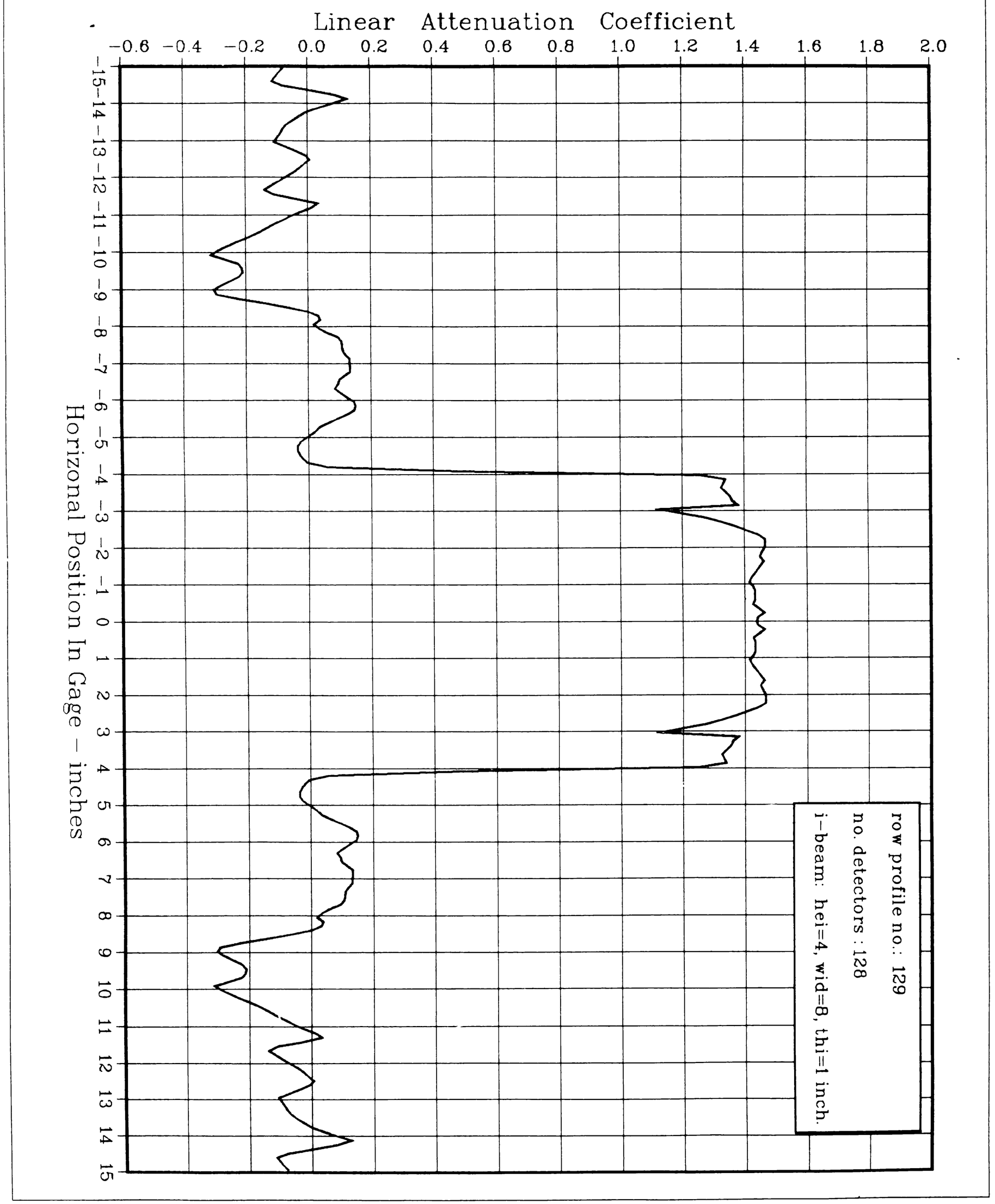

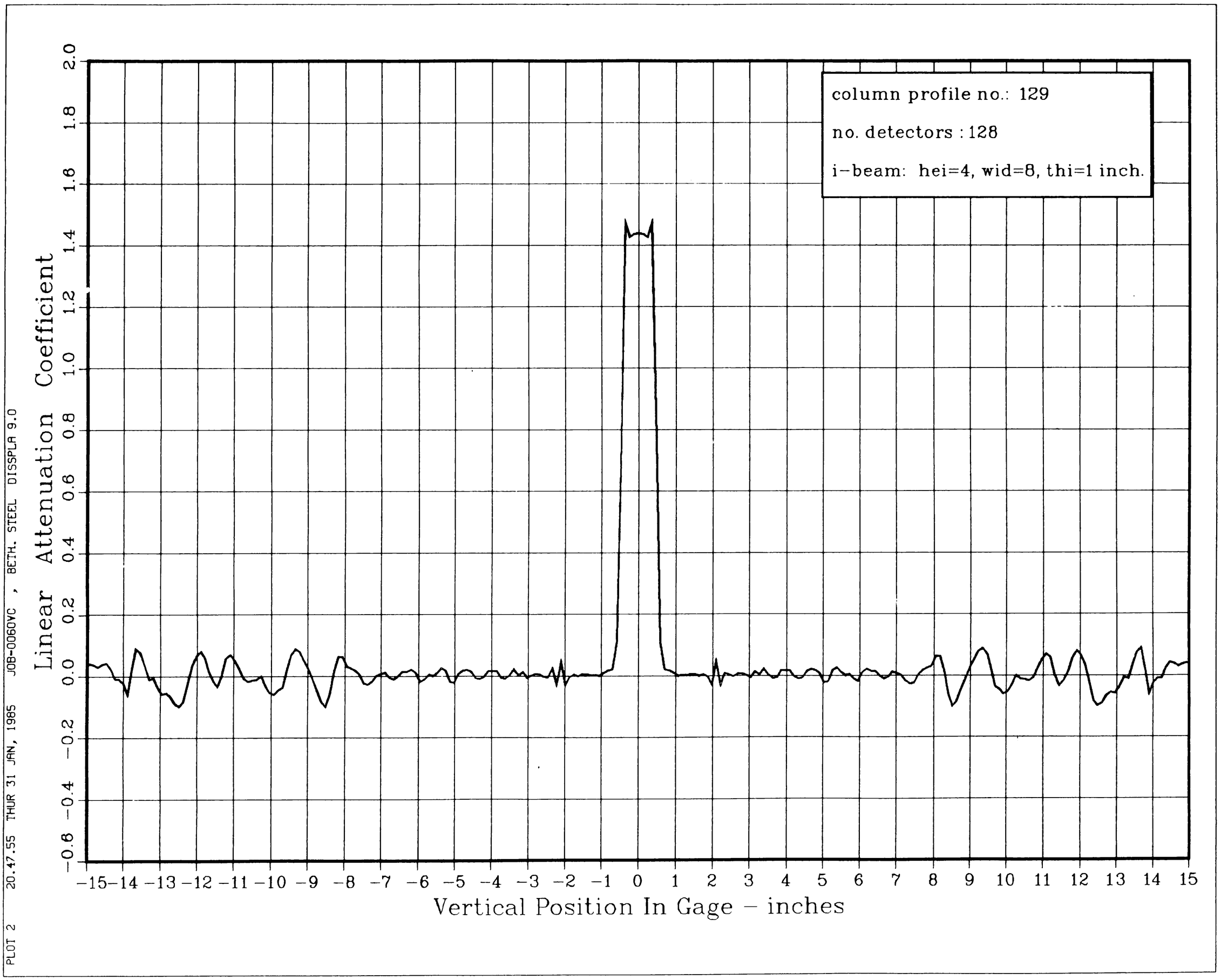
column profile no.: 129
no. detectors : 128
i-beam: hei=4, wid=8, thi=1 inch.
Linear Attenuation Coefficient
2.0
1.8
1.6
1.4
1.2
1.0
0.8
0.6
0.4
0.2
0.0
-0.2
-0.4
-0.6
-15 -14 -13 -12 -11 -10 -9 -8 -7 -6 -5 -4 -3 -2 -1 0 1 2 3 4 5 6 7 8 9 10 11 12 13 14 15
Vertical Position In Gage - inches
PLOT 2 20.47.55 THUR 31 JAN, 1985 JOB-0060VC , BETH. STEEL DISSPLA 9.0

PLOT 1 18.10.18 WED 20 FEB, 1985 JOB-0060VC , BETH. STEEL DISSPLA 9.0

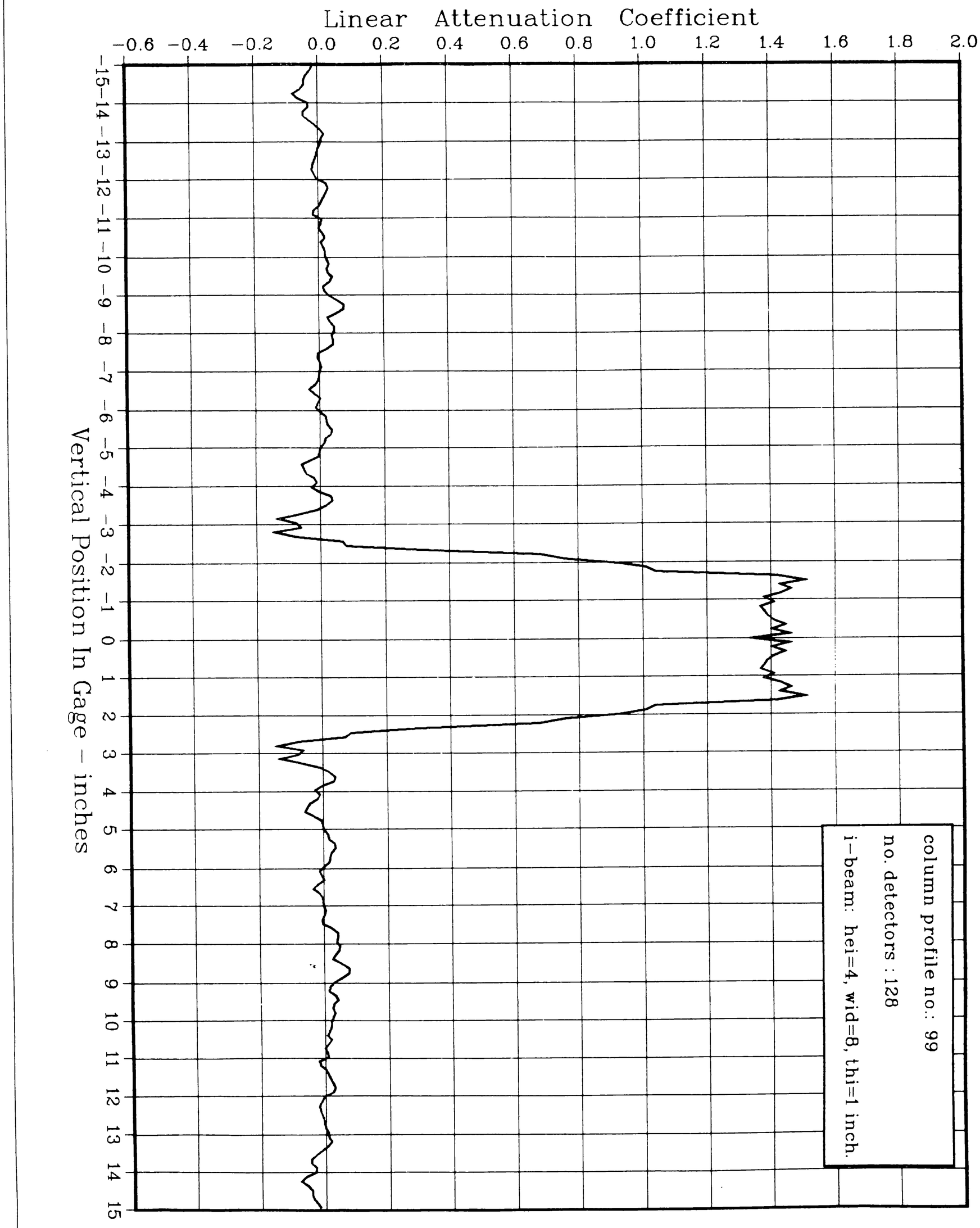

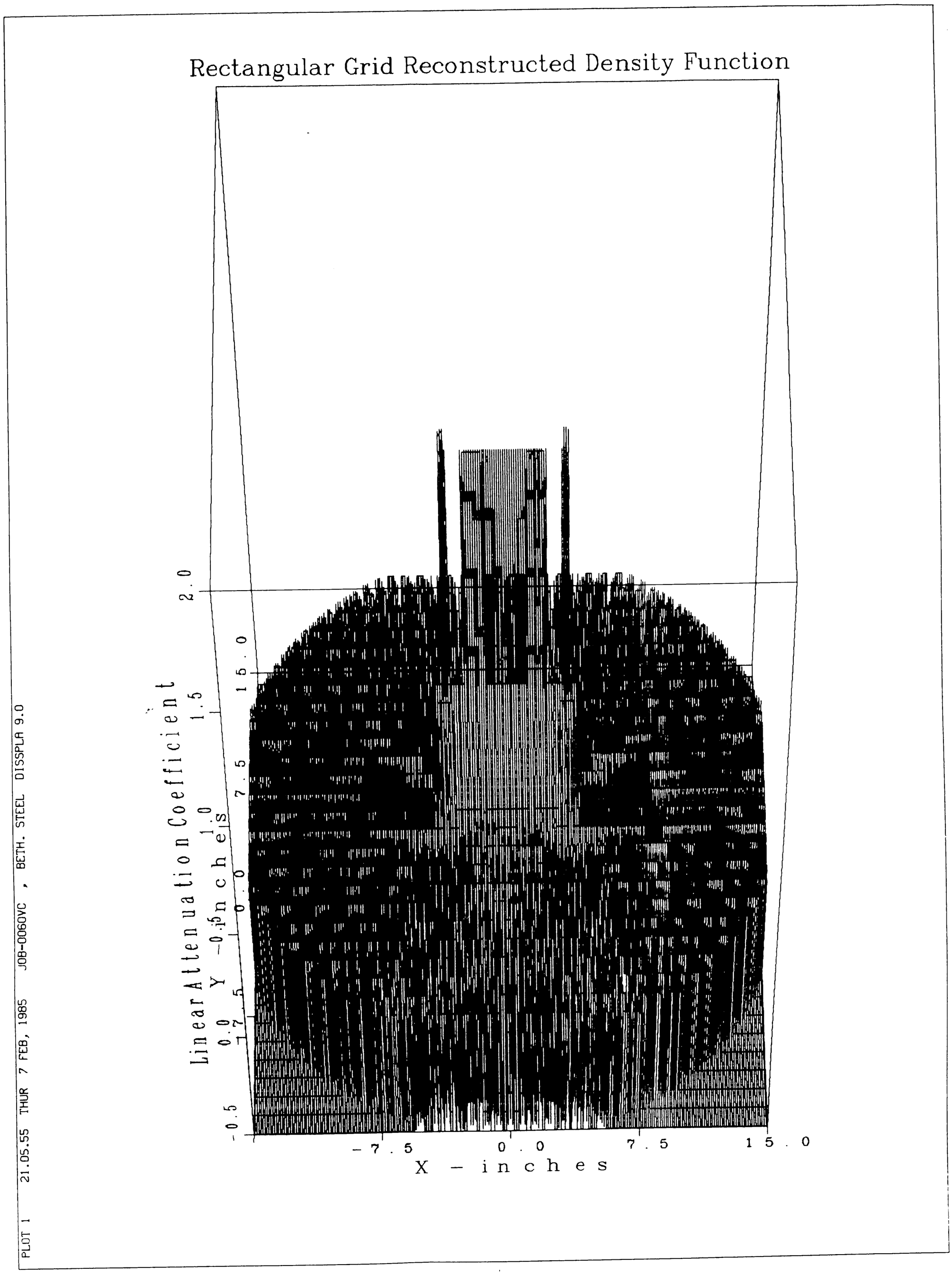
Rectangular Grid Reconstructed Density Function
Linear Attenuation Coefficient
2.0
1.5
1.0
0.5
0.0
-0.5
Y - inches
-7.5
0.0
7.5
15.0
X - inches
PLOT 1 21.05.55 THUR 7 FEB, 1985 JOB-0060VC , BETH. STEEL DISSPLA 9.0

PLOT 1 21.08.21 THUR 7 FEB, 1985 JOB-0060VC , BETH. STEEL DISSPLA 9.0

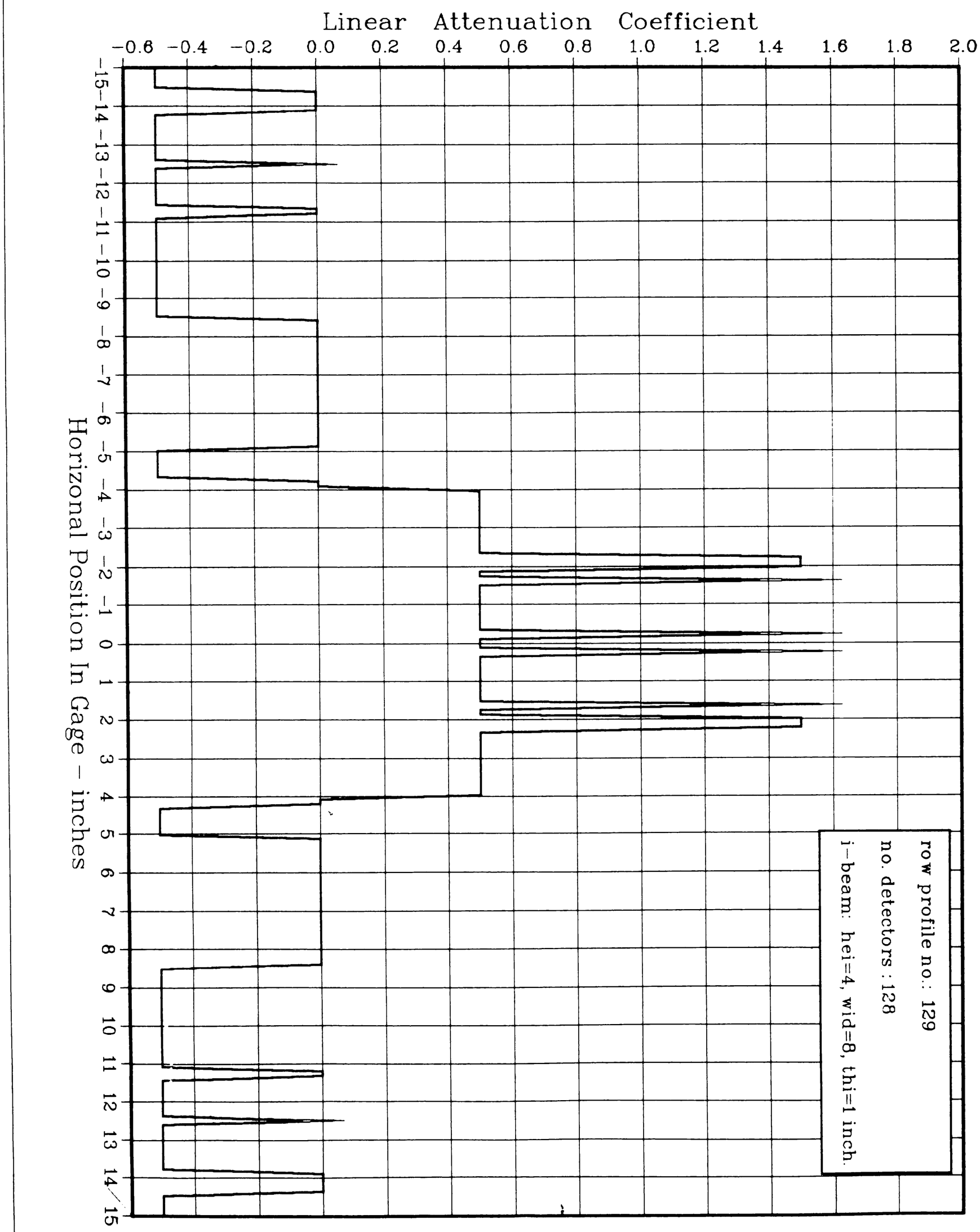

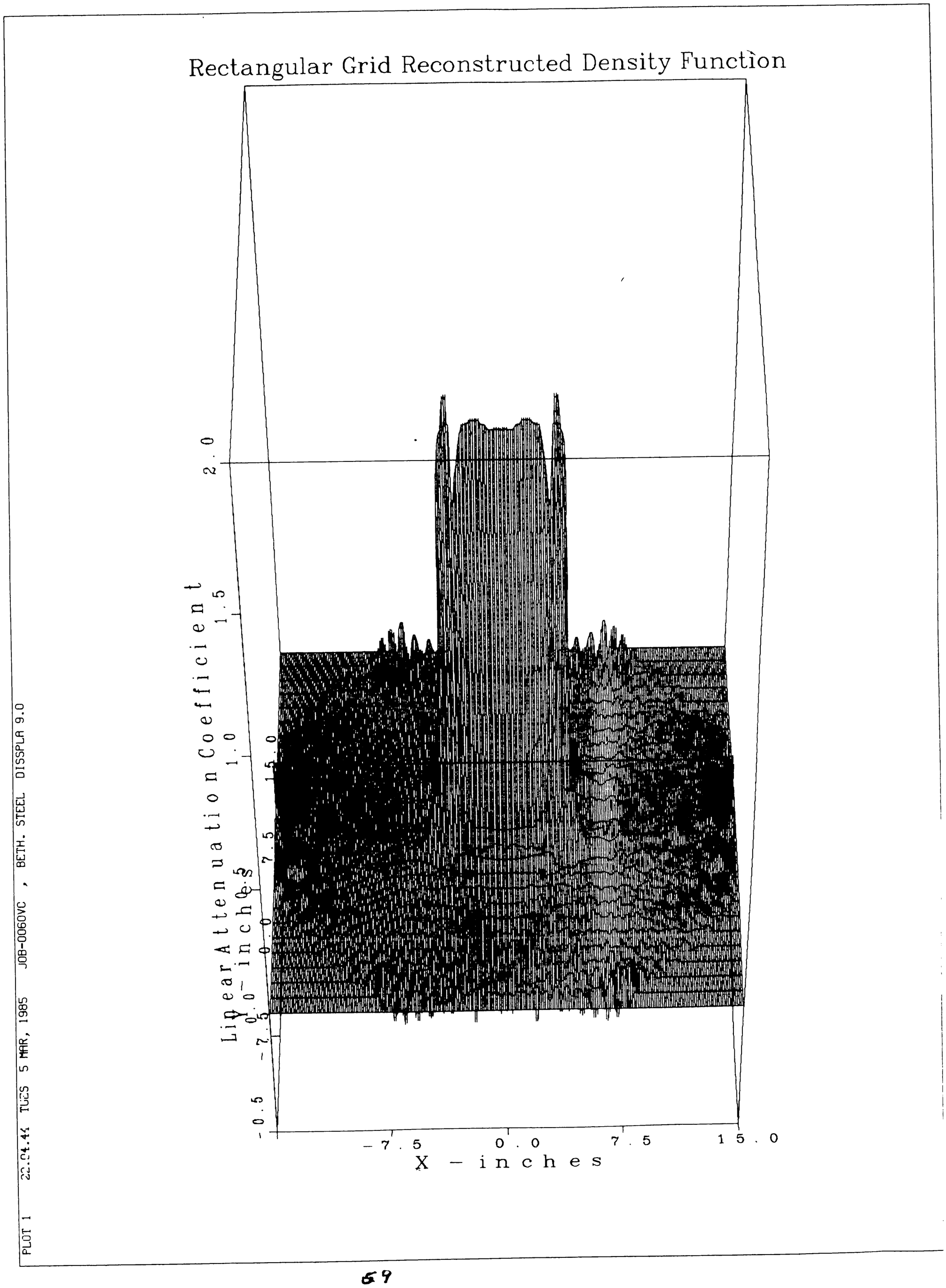
Rectangular Grid Reconstructed Density Function
Linear Attenuation Coefficient
0.0 - inches
2.0
1.5
1.0
0.5
0.0
-0.5
-7.5
0.0
7.5
15.0
X - inches
PLOT 1 22:04:44 TUES 5 MAR, 1985 JOB-0060VC , BETH. STEEL DISSPLA 9.0

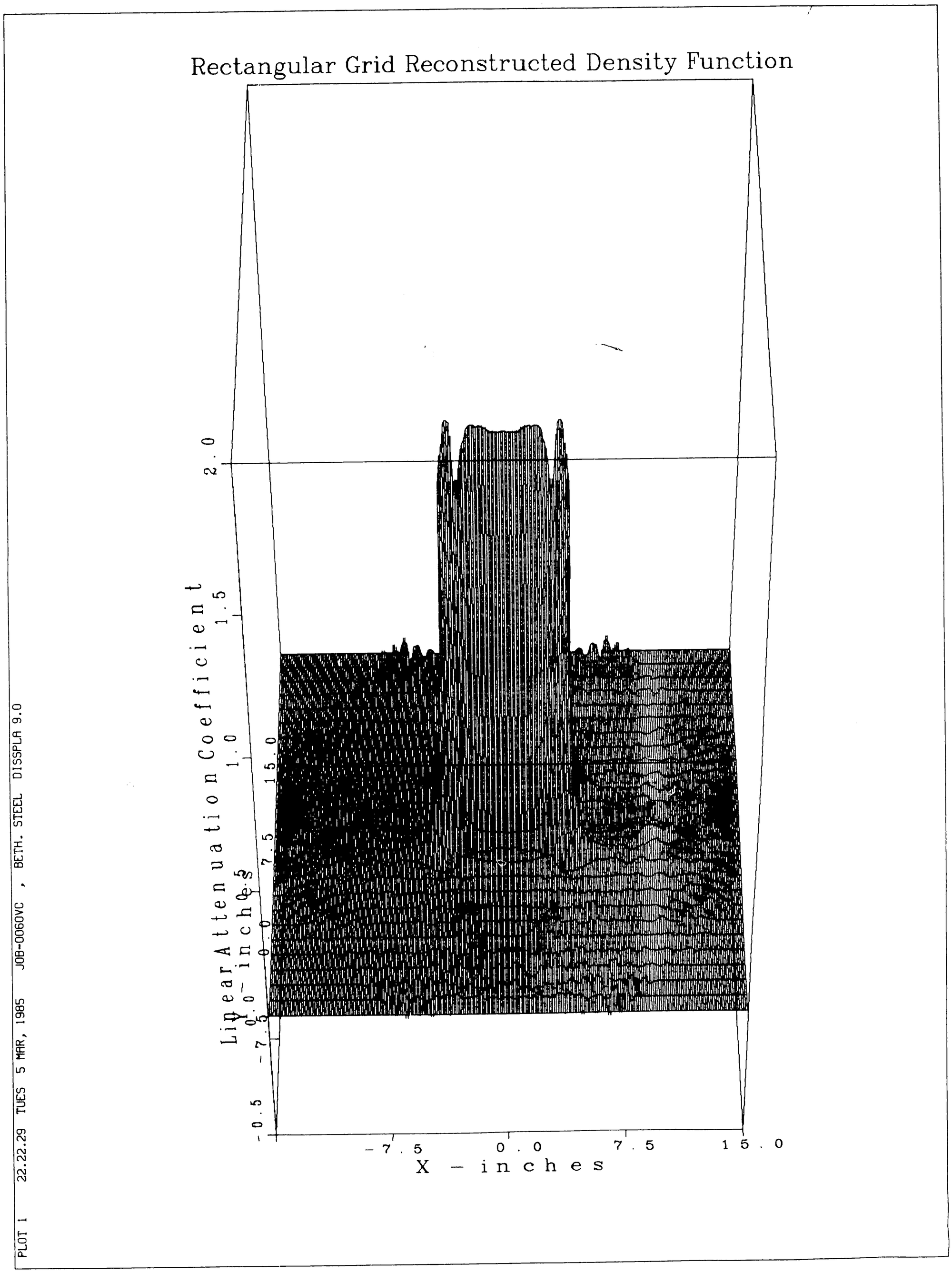
Rectangular Grid Reconstructed Density Function
Linear Attenuation Coefficient
2.0
1.5
1.0
0.5
0.0
-0.5
-7.5
0.0
7.5
15.0
Y - inches
-7.5
0.0
7.5
15.0
X - inches
PLOT 1
22.22.29 TUES 5 MAR, 1985 JOB-0060VC , BETH. STEEL DISSPLA 9.0

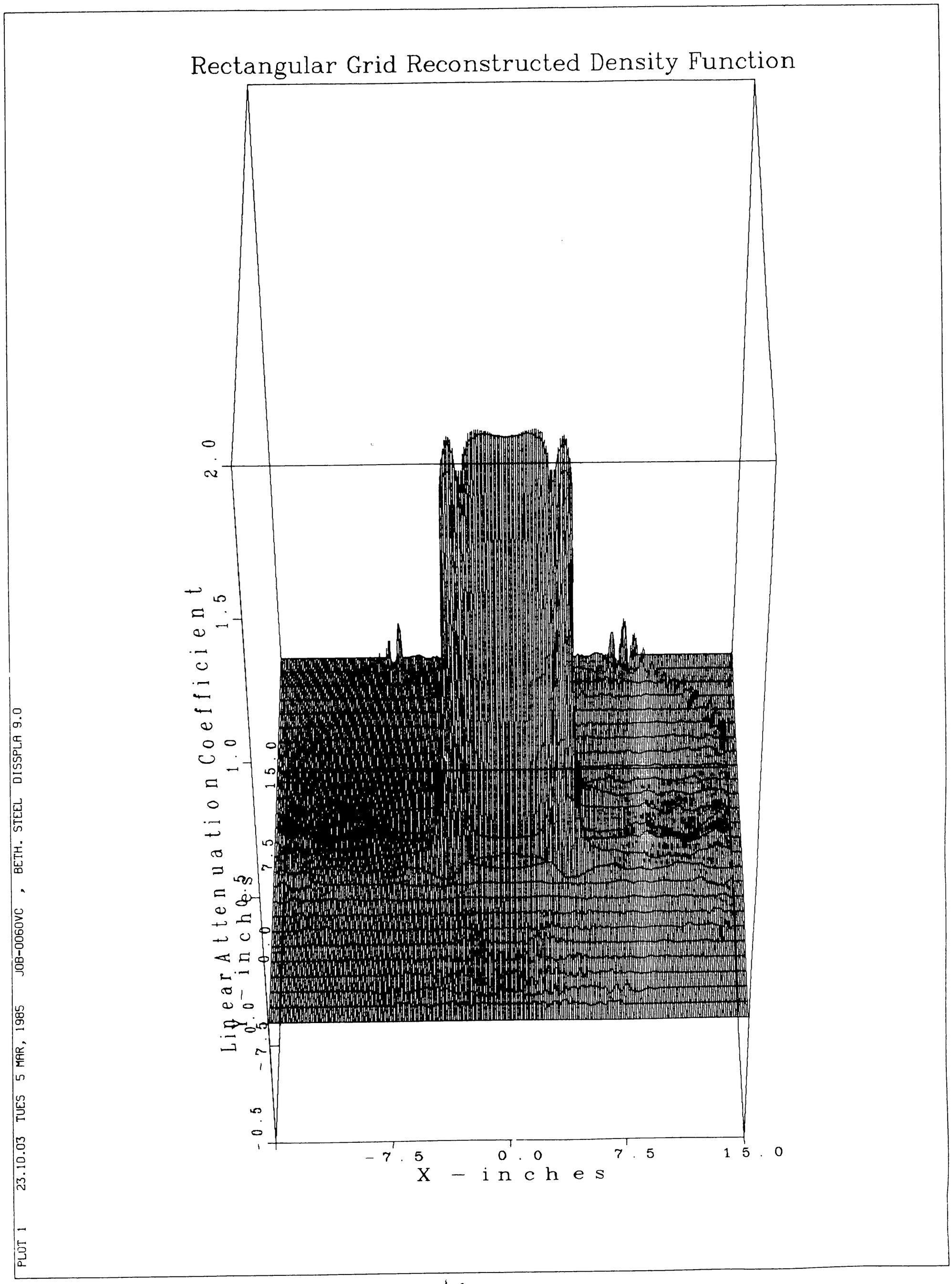
Rectangular Grid Reconstructed Density Function
Linear Attenuation Coefficient
2.0
1.5
1.0
0.5
0.0
-0.5
-7.5
0.0
7.5
15.0
Y - inches
-7.5
0.0
7.5
15.0
X - inches
PLOT 1 23.10.03 TUES 5 MAR, 1985 JOB-0060VC , BETH. STEEL DISSPLA 9.0

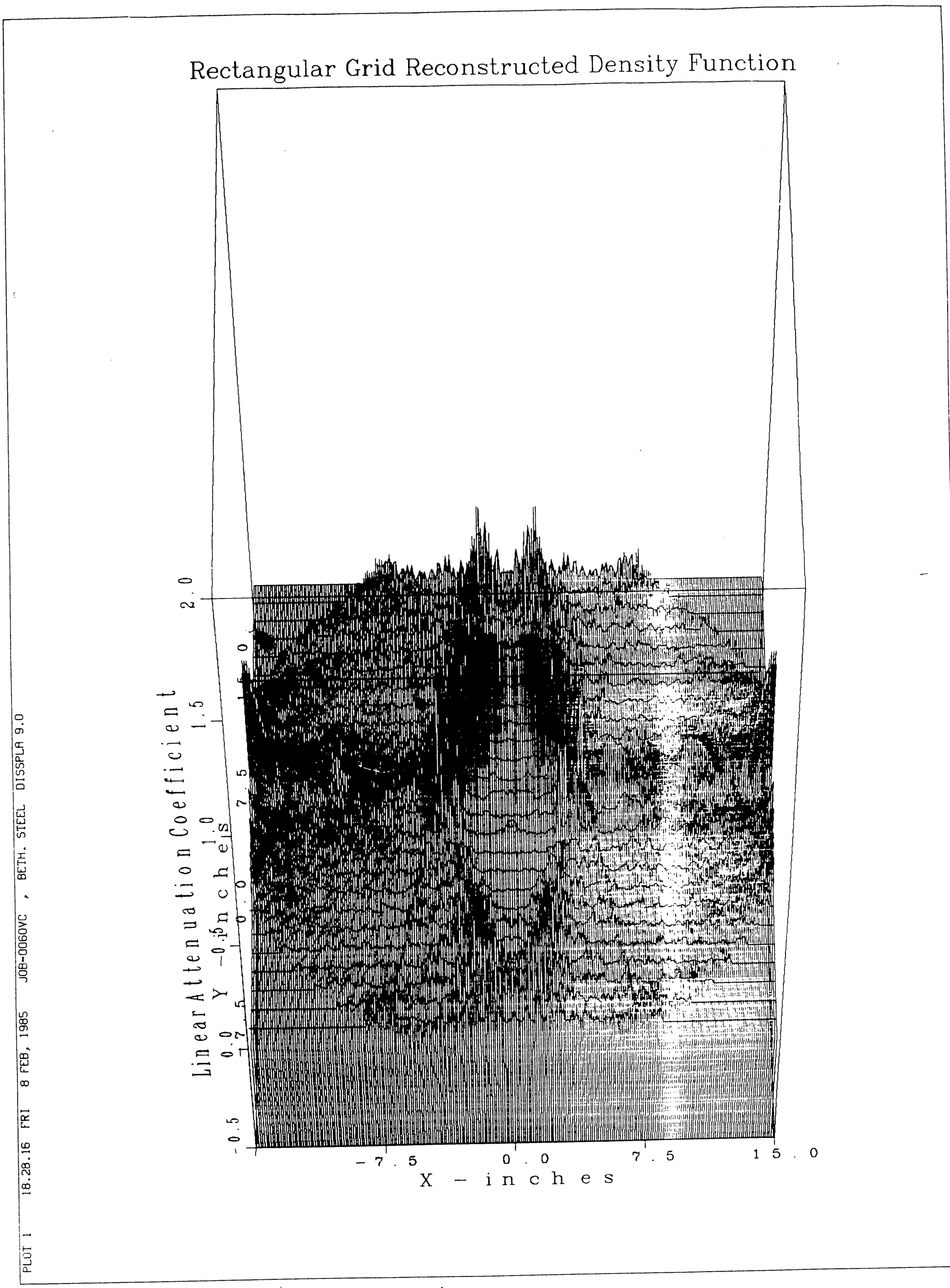
Rectangular Grid Reconstructed Density Function
Linear Attenuation Coefficient
Y - inches
X - inches
2.0
1.5
1.0
0.5
0.0
-0.5
-7.5
0.0
7.5
15.0
PLOT 1 18.28.16 FRI 8 FEB, 1985 JOB-0060VC , BETH. STEEL DISSPLA 9.0

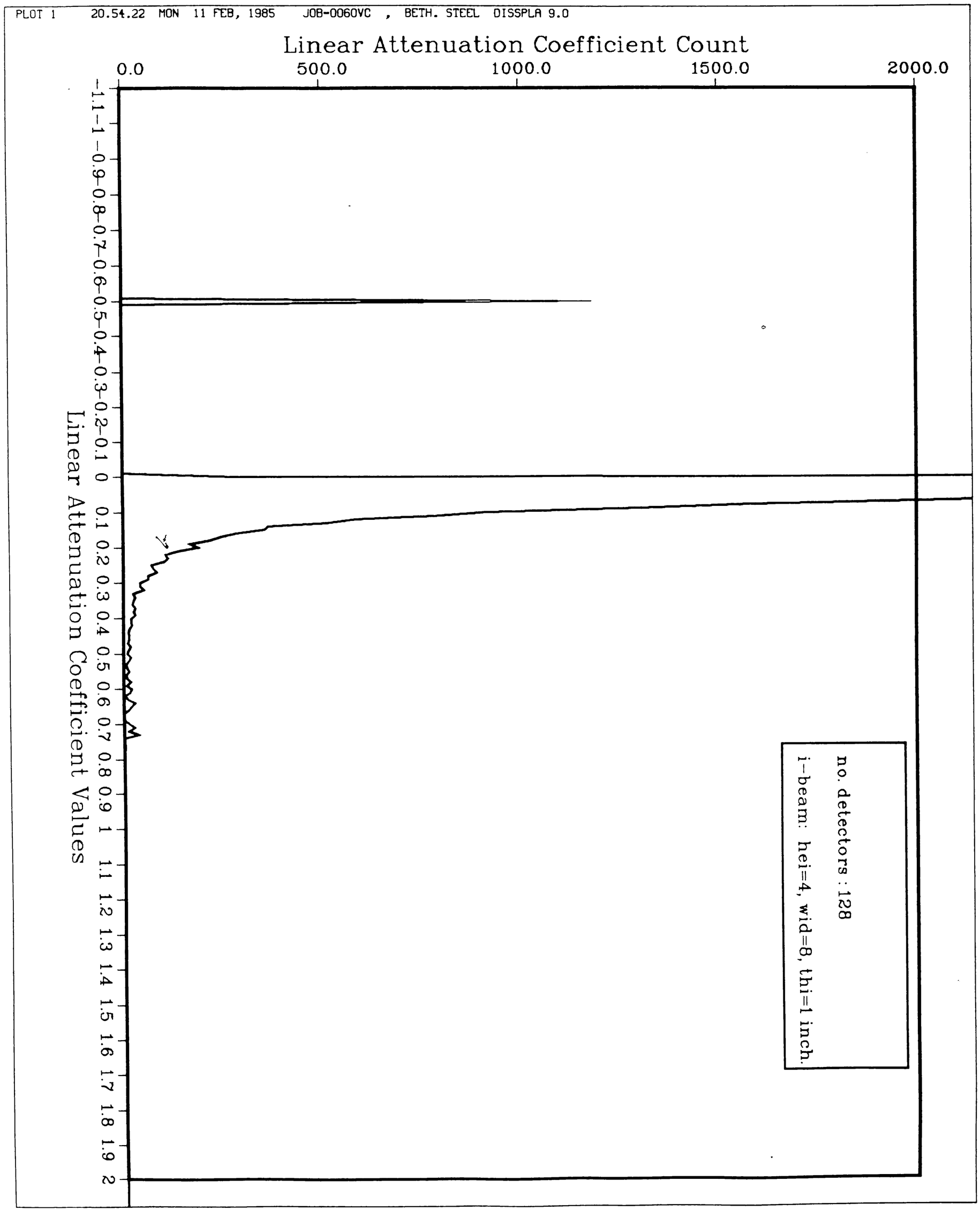
PLOT 1 20.54.22 MON 11 FEB, 1985 JOB-0060VC , BETH. STEEL DISSPLA 9.0
Linear Attenuation Coefficient Count
0.0
500.0
1000.0
1500.0
2000.0
-1.1 -1 -0.9 -0.8 -0.7 -0.6 -0.5 -0.4 -0.3 -0.2 -0.1 0 0.1 0.2 0.3 0.4 0.5 0.6 0.7 0.8 0.9 1 1.1 1.2 1.3 1.4 1.5 1.6 1.7 1.8 1.9 2
Linear Attenuation Coefficient Values
no. detectors : 128
i-beam: hei=4, wid=8, thi=1 inch.

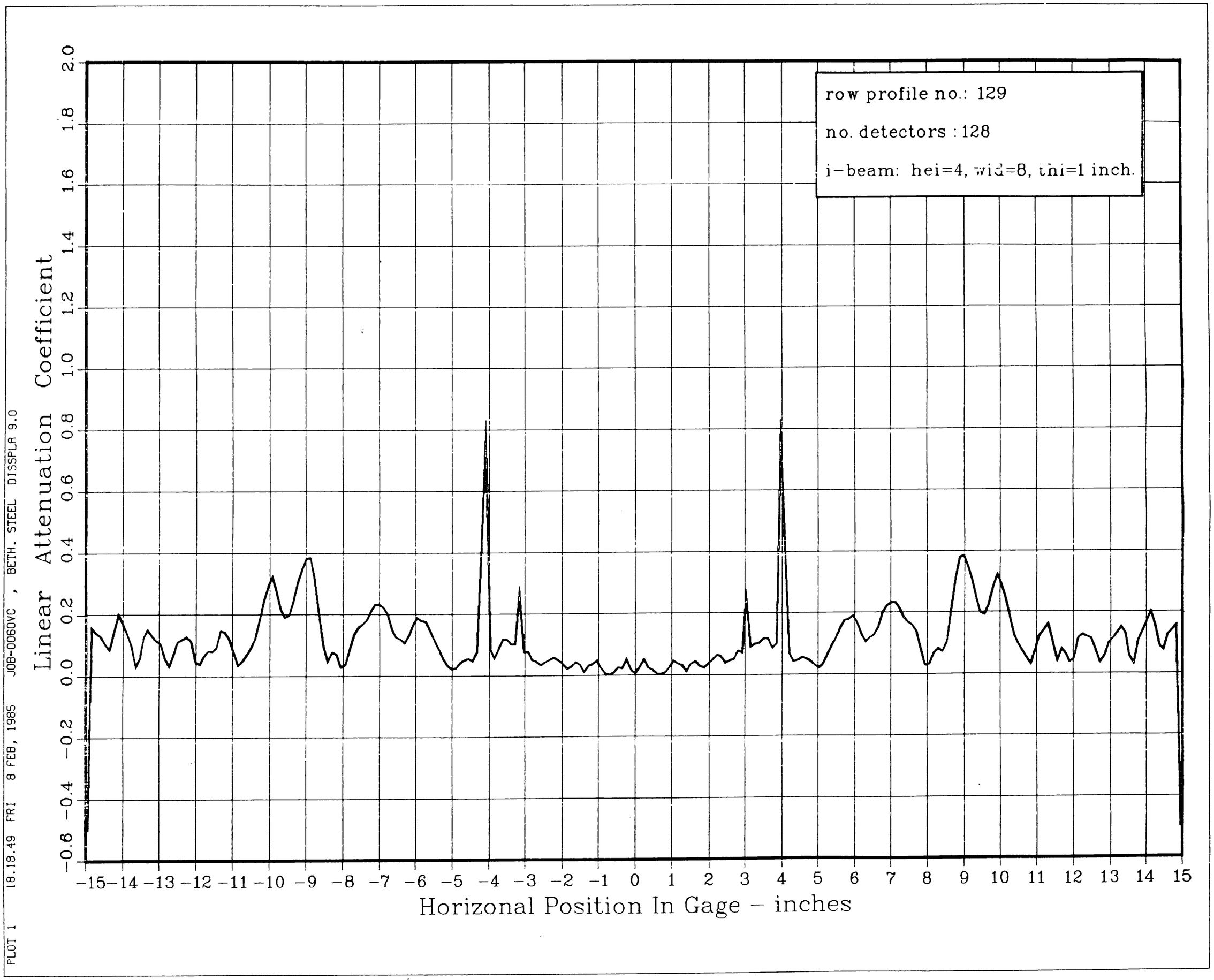

row profile no.: 129
no. detectors : 128
i-beam: hei=4, wid=8, thi=1 inch.
Linear Attenuation Coefficient
Horizonal Position In Gage - inches
PLOT 1 18.18.49 FRI 8 FEB, 1985 JOB-0060VC , BETH. STEEL DISSPLA 9.0

69

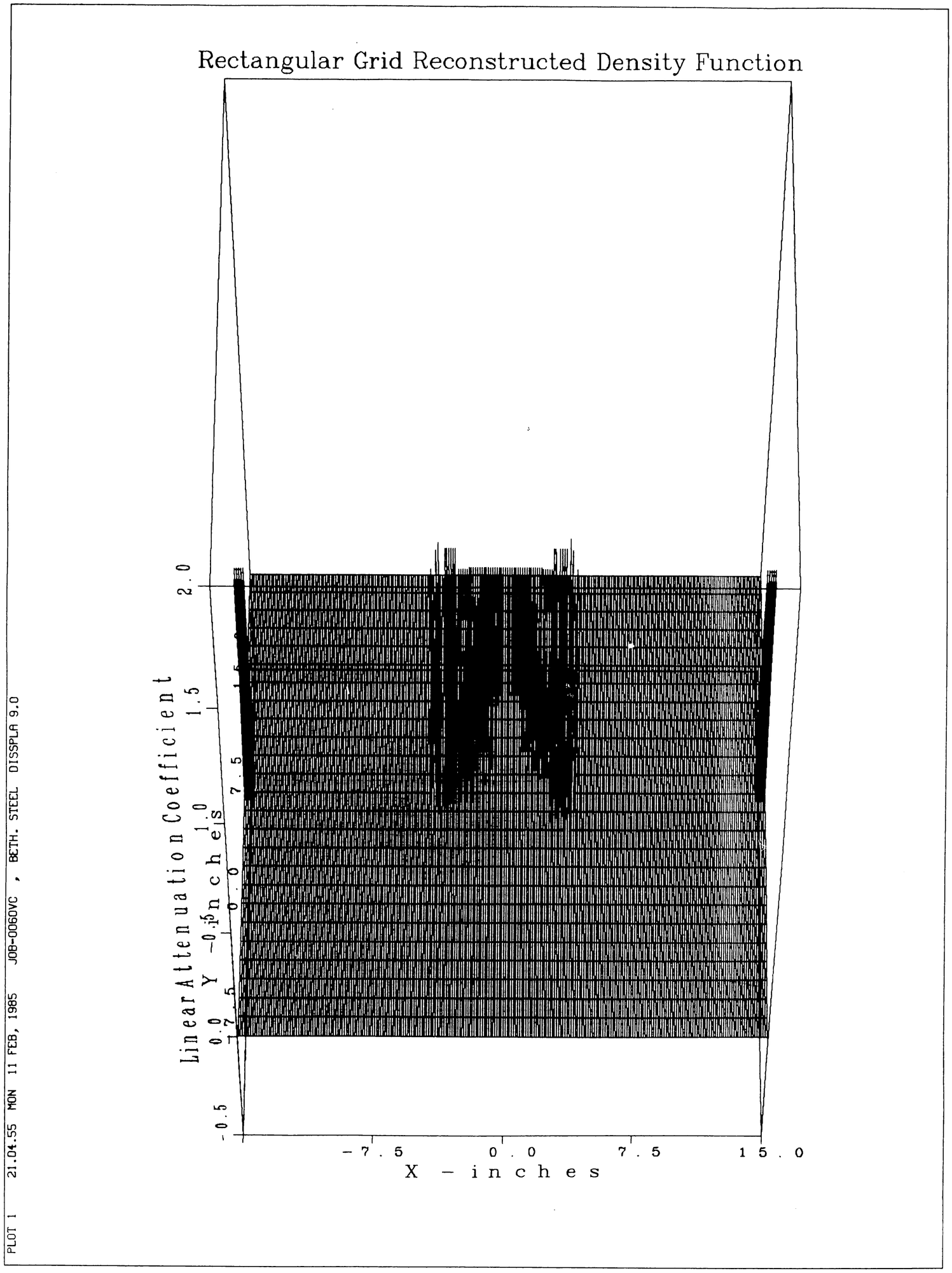
Rectangular Grid Reconstructed Density Function
Linear Attenuation Coefficient
Y - inches
X - inches
2.0
1.5
1.0
0.5
0.0
-0.5
7.5
0.0
-7.5
15.0
PLOT 1 21.04.55 MON 11 FEB, 1985 JOB-0060VC , BETH. STEEL DISSPLA 9.0

PLOT 1 21.08.30 MON 11 FEB, 1985 JOB-0060VC , BETH. STEEL DISSPLA 9.0

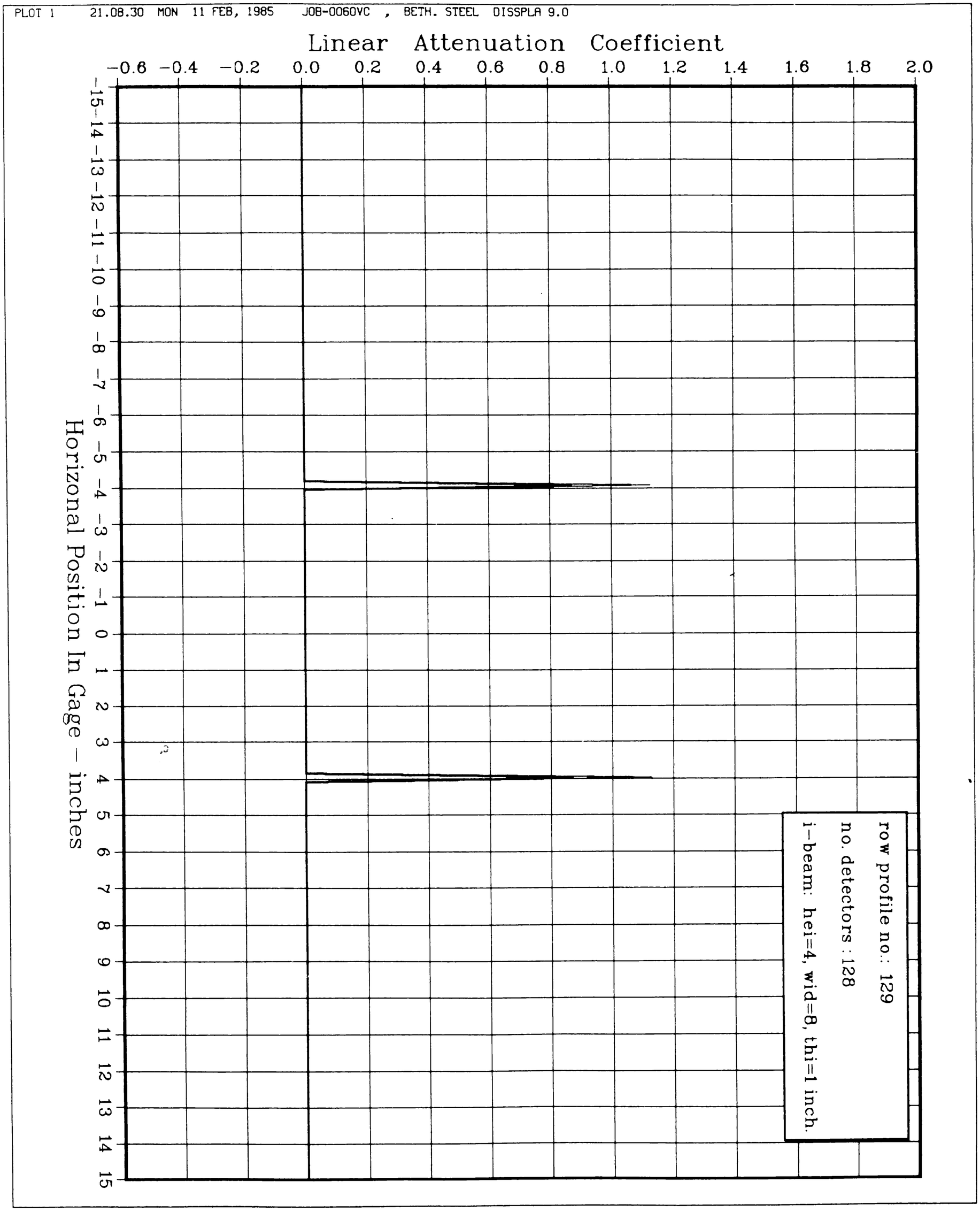

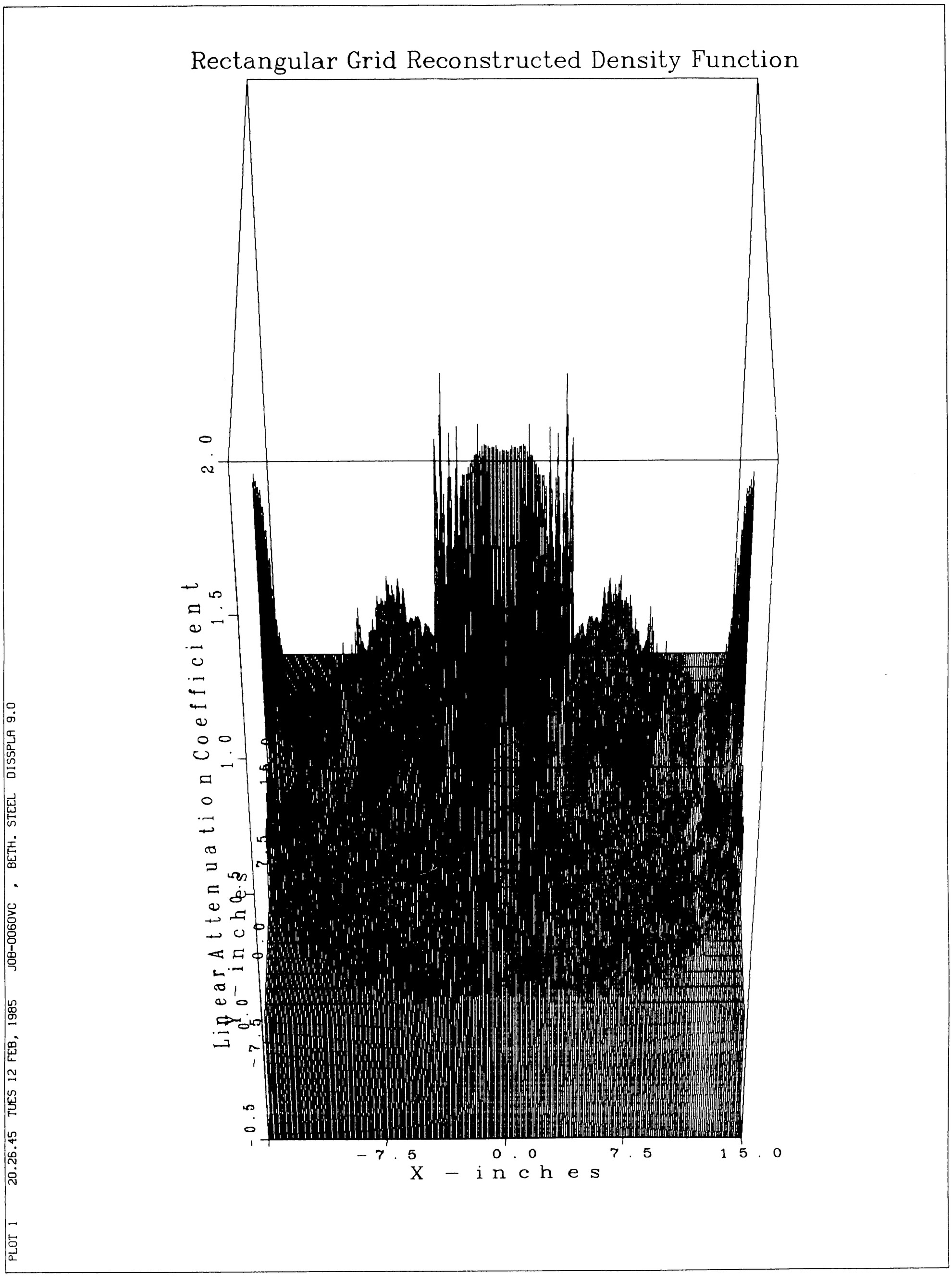
Rectangular Grid Reconstructed Density Function
Linear Attenuation Coefficient
0.0 - inches
0.5
1.0
1.5
2.0
-0.5
0.0
7.5
15.0
-7.5
0.0
7.5
15.0
X - inches
PLOT 1 20.26.45 TUES 12 FEB, 1985 JOB-0060VC , BETH. STEEL DISSPLA 9.0

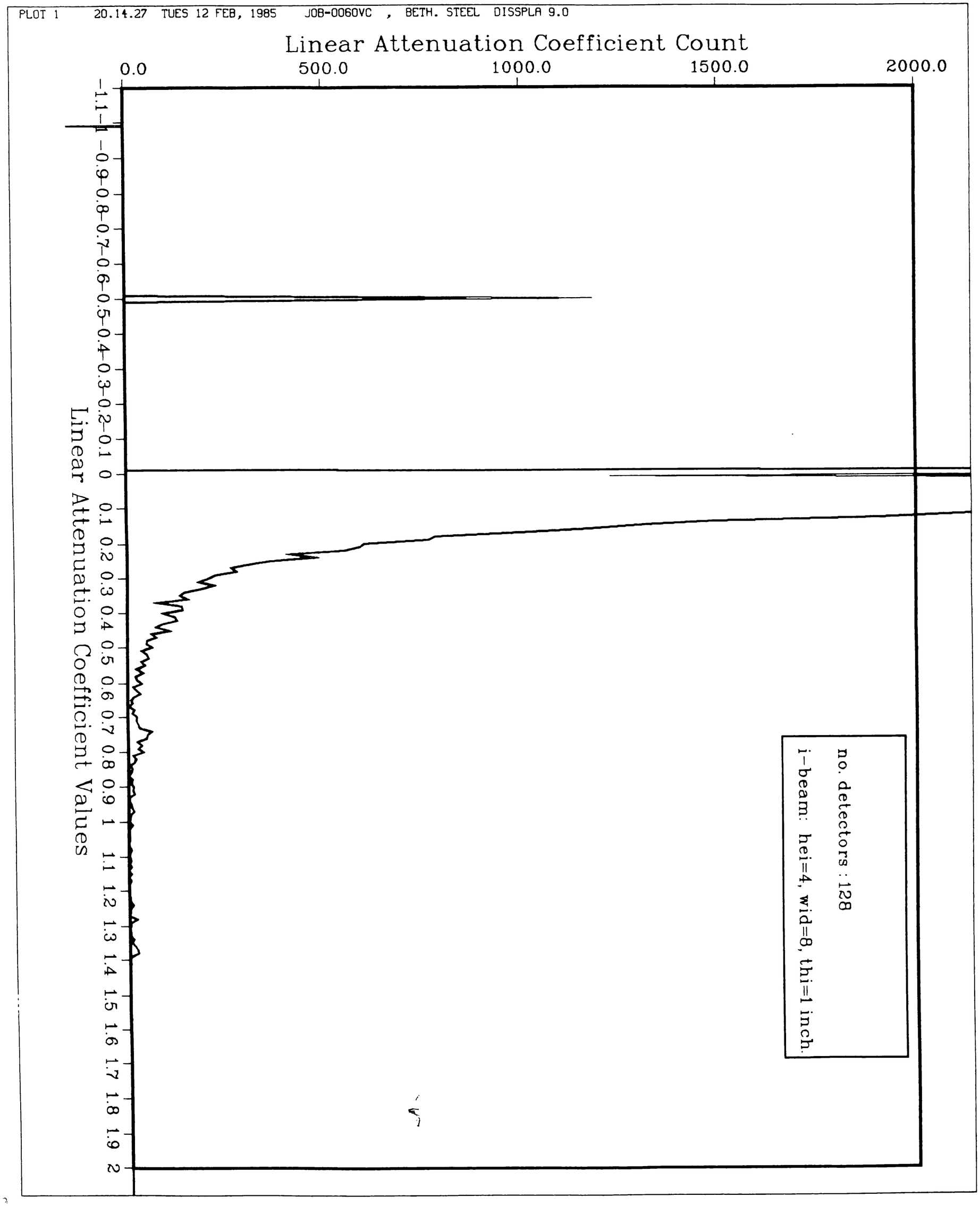
PLOT 1 20.14.27 TUES 12 FEB, 1985 JOB-0060VC , BETH. STEEL DISSPLA 9.0
Linear Attenuation Coefficient Count
0.0
500.0
1000.0
1500.0
2000.0
Linear Attenuation Coefficient Values
-1.1 -1 -0.9 -0.8 -0.7 -0.6 -0.5 -0.4 -0.3 -0.2 -0.1 0 0.1 0.2 0.3 0.4 0.5 0.6 0.7 0.8 0.9 1 1.1 1.2 1.3 1.4 1.5 1.6 1.7 1.8 1.9 2
no. detectors : 128
i-beam: hei=4, wid=8, thi=1 inch.

PLOT 1 20.30.34 TUES 12 FEB, 1985 JOB-0060VC , BETH. STEEL DISSPLA 9.0

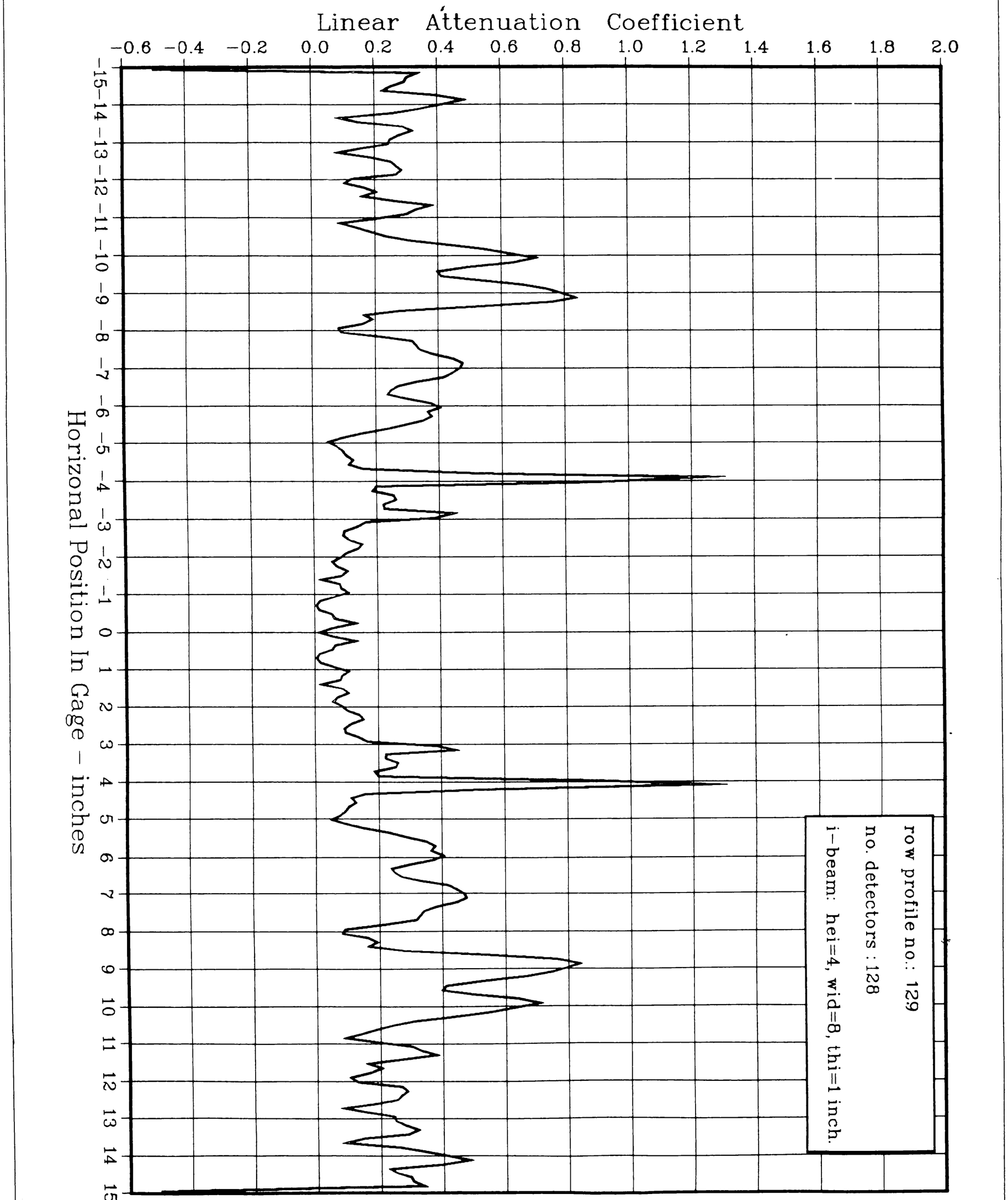

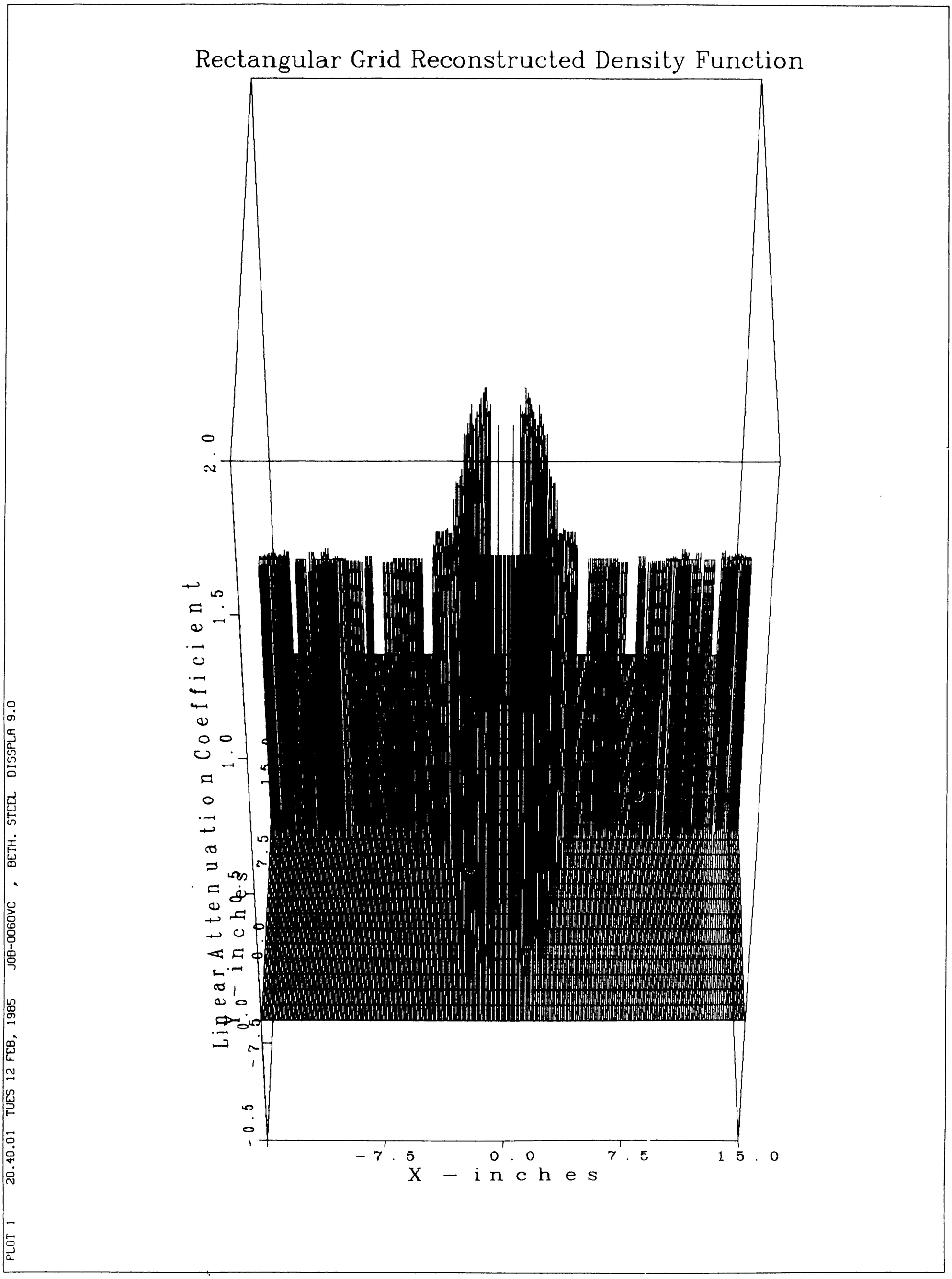
Rectangular Grid Reconstructed Density Function
Linear Attenuation Coefficient
1/0 - inches
2.0
1.5
1.0
0.5
0.0
-0.5
-7.5
0.0
7.5
15.0
X - inches
PLOT 1 20.40.01 TUES 12 FEB, 1985 JOB-0060VC , BETH. STEEL DISSPLA 9.0

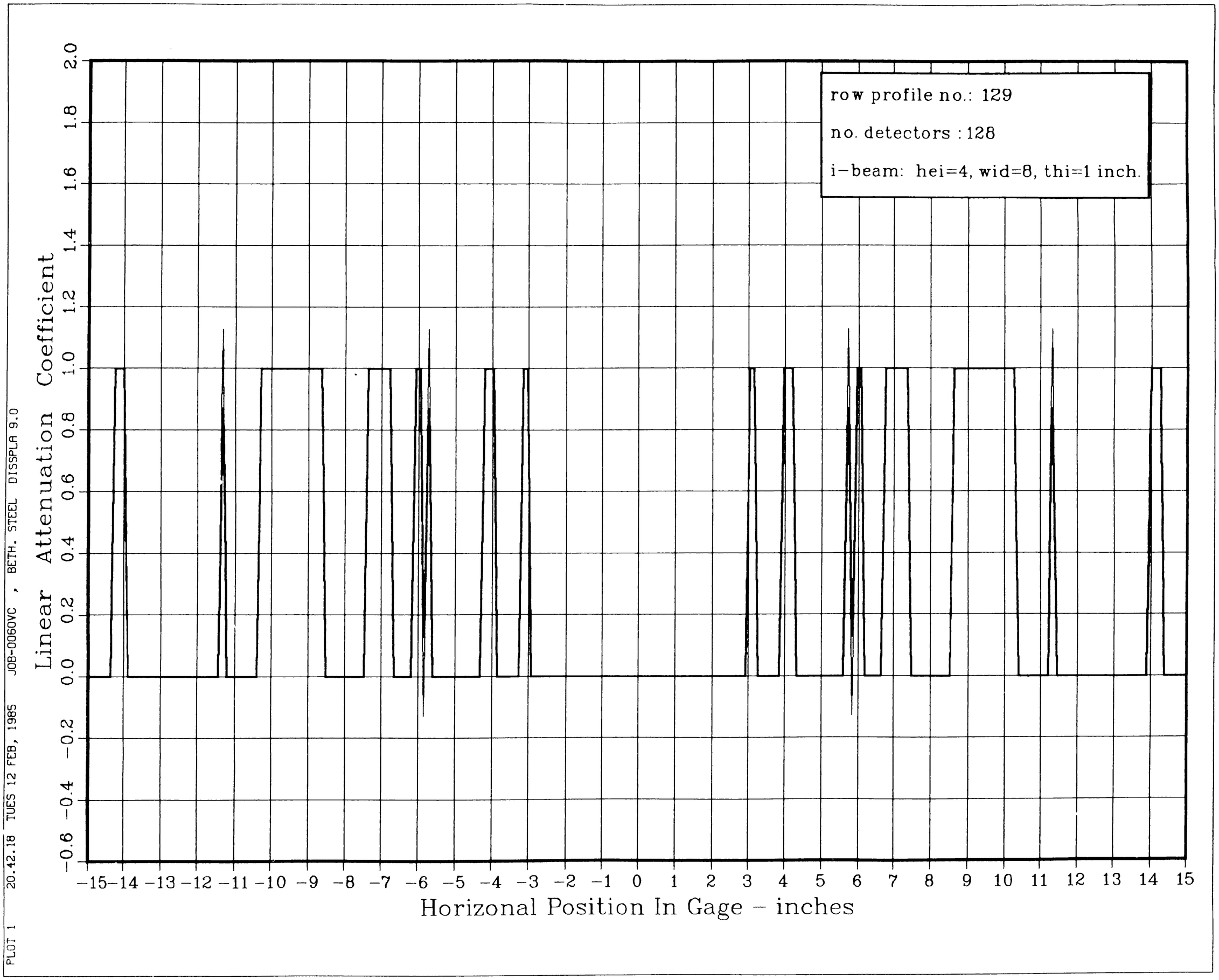
row profile no.: 129
no. detectors : 128
i-beam: hei=4, wid=8, thi=1 inch.
Linear Attenuation Coefficient
2.0
1.8
1.6
1.4
1.2
1.0
0.8
0.6
0.4
0.2
0.0
-0.2
-0.4
-0.6
-15 -14 -13 -12 -11 -10 -9 -8 -7 -6 -5 -4 -3 -2 -1 0 1 2 3 4 5 6 7 8 9 10 11 12 13 14 15
Horizonal Position In Gage - inches
PLOT 1 20.42.18 TUES 12 FEB, 1985 JOB-0060VC , BETH. STEEL DISSPLA 9.0

77

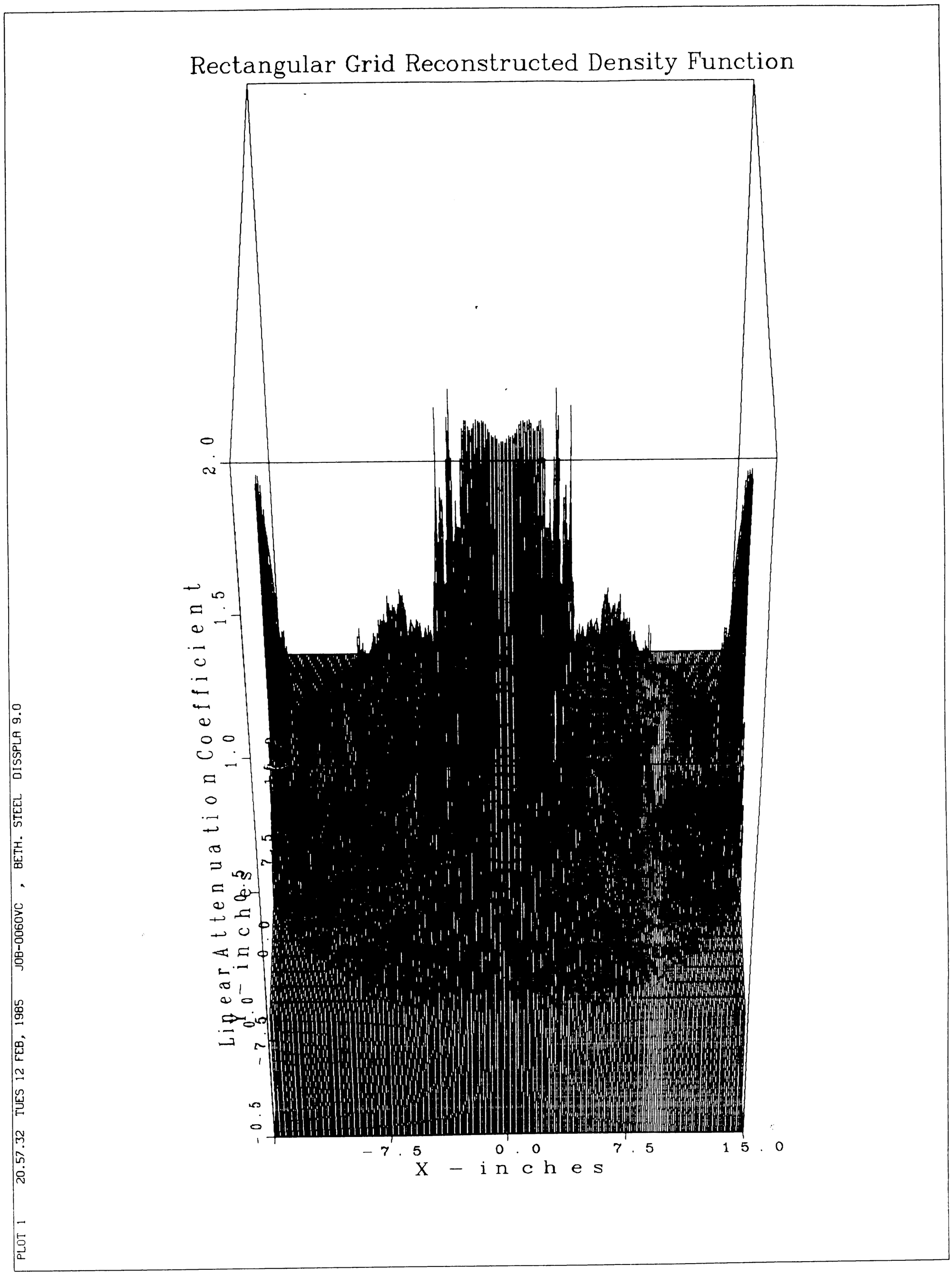
Rectangular Grid Reconstructed Density Function
Linear Attenuation Coefficient
2.0
1.5
1.0
0.5
0.0
-0.5
Y - inches
-7.5
0.0
7.5
X - inches
-7.5
0.0
7.5
15.0
PLOT 1 20.57.32 TUES 12 FEB, 1985 JOB-0060VC , BETH. STEEL DISSPLA 9.0

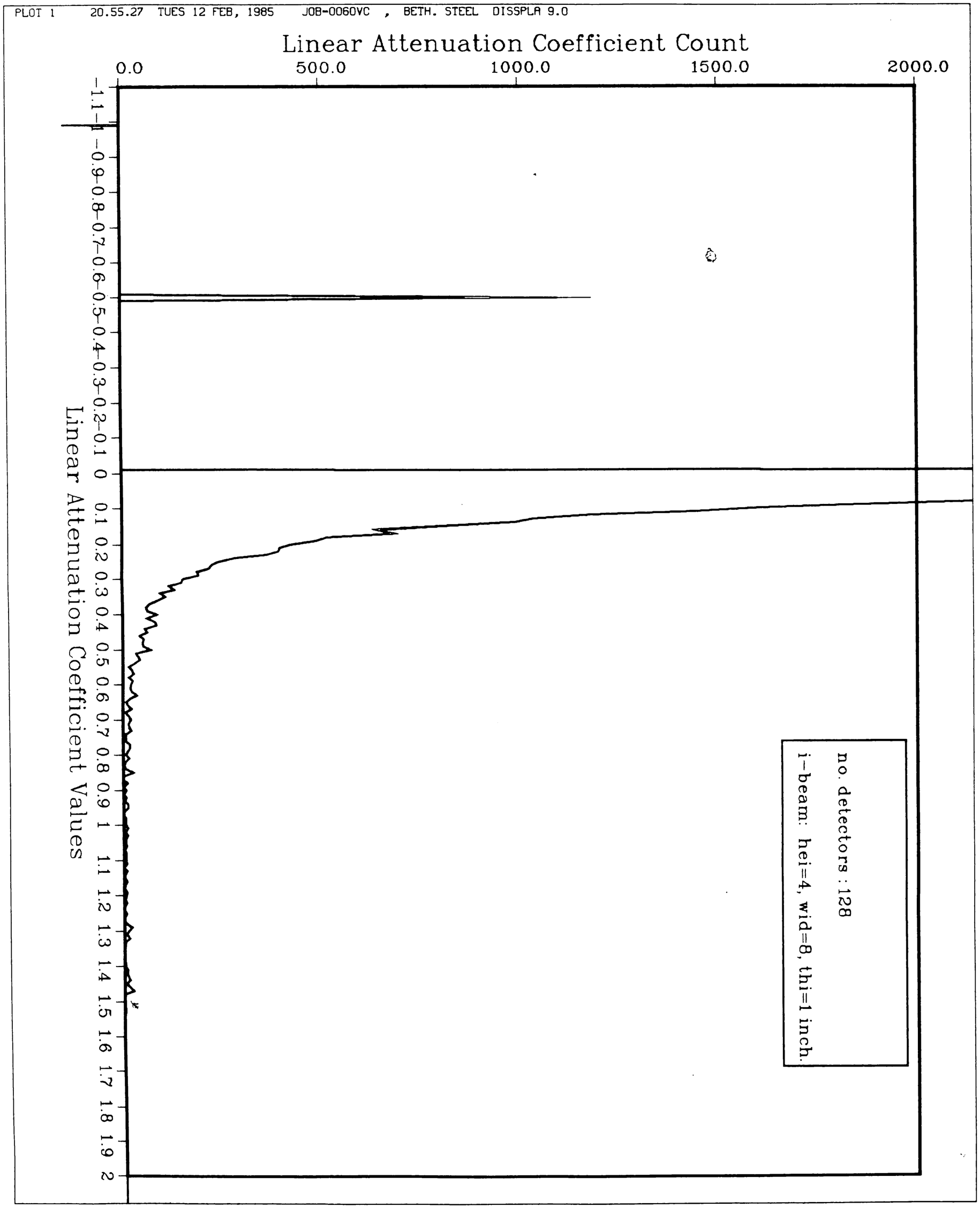
PLOT 1 20.55.27 TUES 12 FEB, 1985 JOB-0060VC , BETH. STEEL DISSPLA 9.0
Linear Attenuation Coefficient Count
0.0
500.0
1000.0
1500.0
2000.0
-1.1 -1 -0.9 -0.8 -0.7 -0.6 -0.5 -0.4 -0.3 -0.2 -0.1 0 0.1 0.2 0.3 0.4 0.5 0.6 0.7 0.8 0.9 1 1.1 1.2 1.3 1.4 1.5 1.6 1.7 1.8 1.9 2
Linear Attenuation Coefficient Values
no. detectors : 128
i-beam: hei=4, wid=8, thi=1 inch.

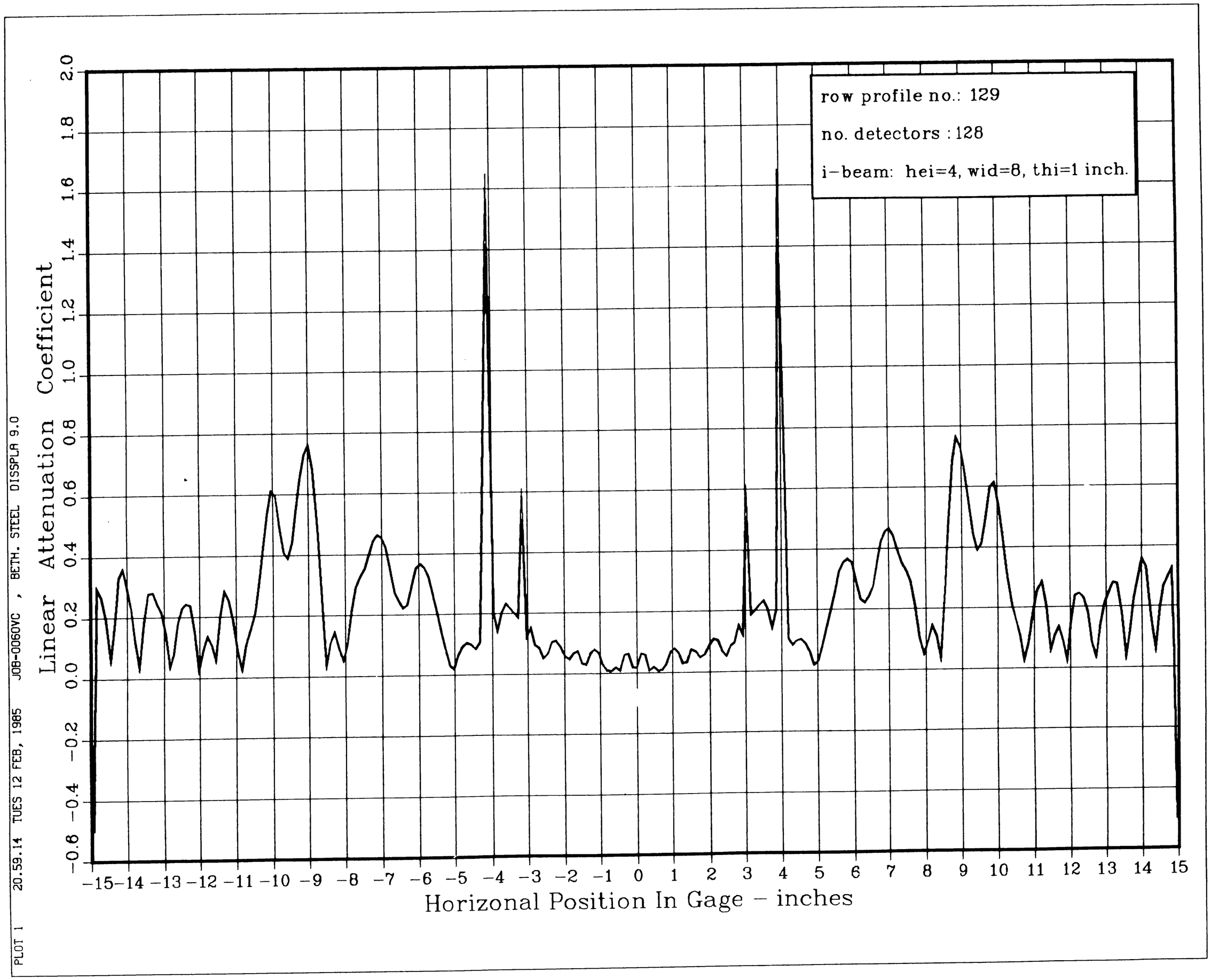
row profile no.: 129
no. detectors : 128
i-beam: hei=4, wid=8, thi=1 inch.
Linear Attenuation Coefficient
2.0
1.8
1.6
1.4
1.2
1.0
0.8
0.6
0.4
0.2
0.0
-0.2
-0.4
-0.6
-15 -14 -13 -12 -11 -10 -9 -8 -7 -6 -5 -4 -3 -2 -1 0 1 2 3 4 5 6 7 8 9 10 11 12 13 14 15
Horizonal Position In Gage - inches
PLOT 1 20.59.14 TUES 12 FEB, 1985 JOB-0060VC , BETH. STEEL DISSPLA 9.0

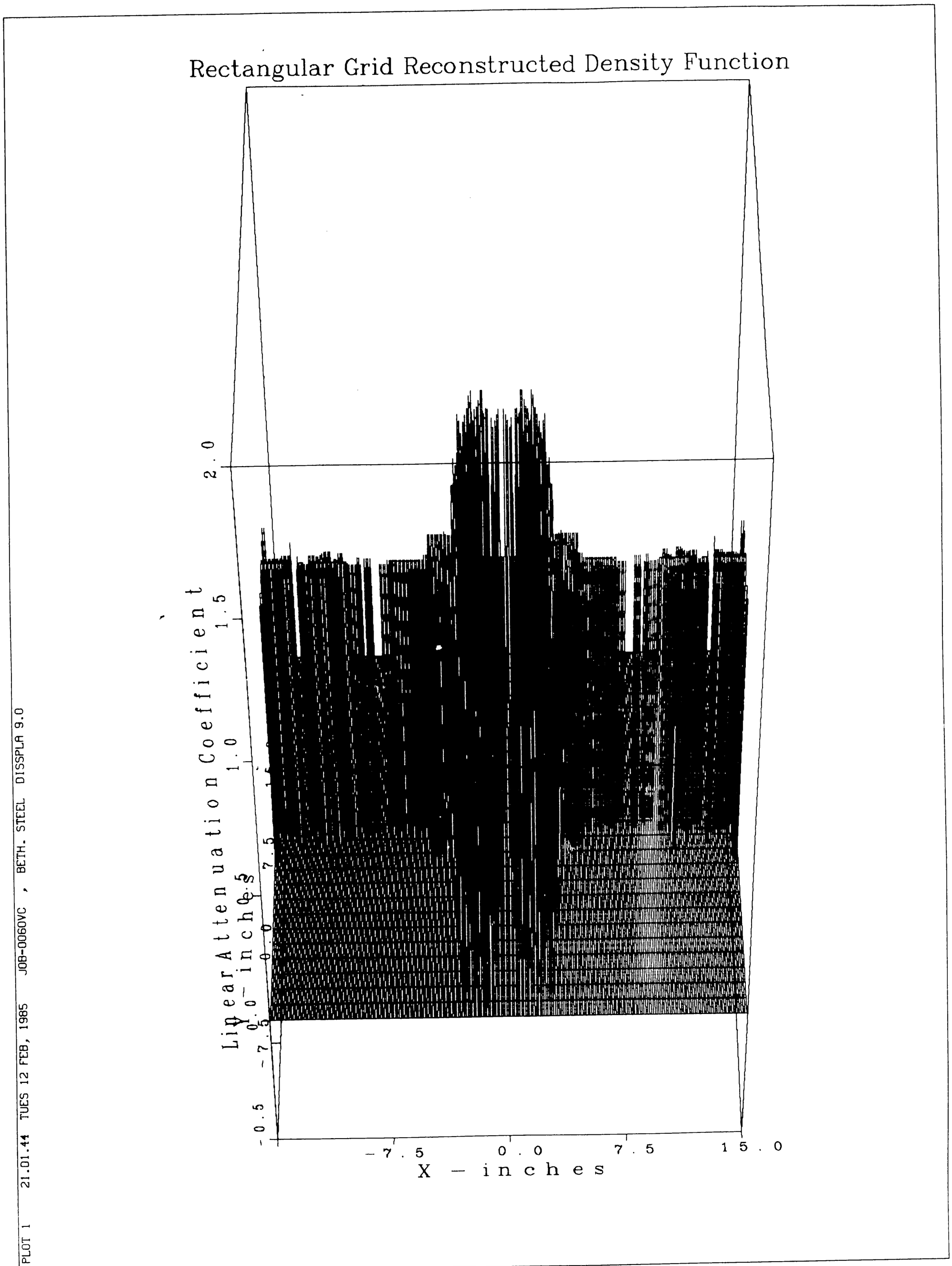
Rectangular Grid Reconstructed Density Function
Linear Attenuation Coefficient
2.0
1.5
1.0
0.5
0.0
-0.5
Y - inches
-7.5
0.0
7.5
15.0
X - inches
PLOT 1 21.01.44 TUES 12 FEB, 1985 JOB-0060VC , BETH. STEEL DISSPLA 9.0

PLOT 1 21.04.34 TUES 12 FEB, 1985 JOB-0060VC , BETH. STEEL DISSPLA 9.0

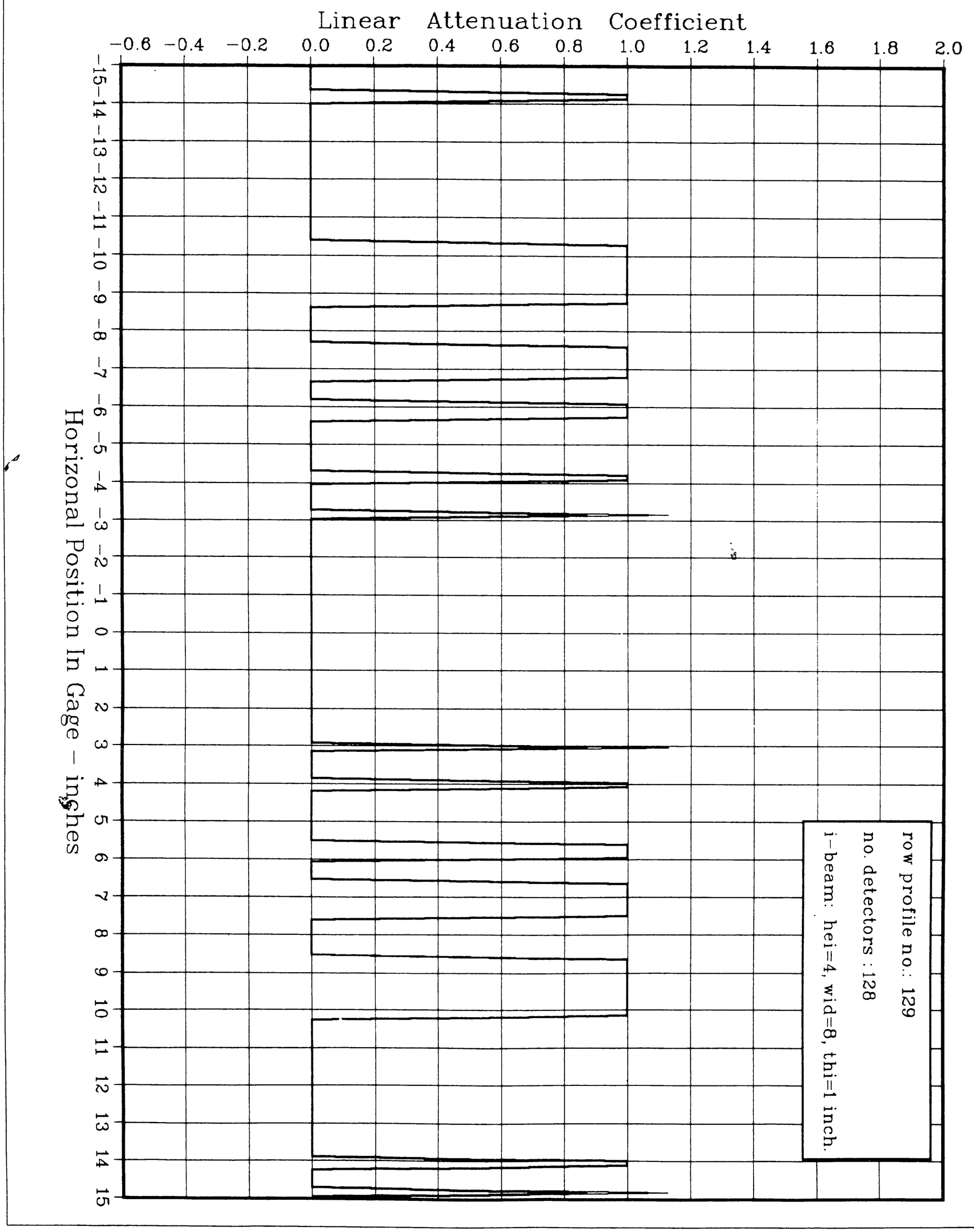

Appendix B
Graphs of Image ii

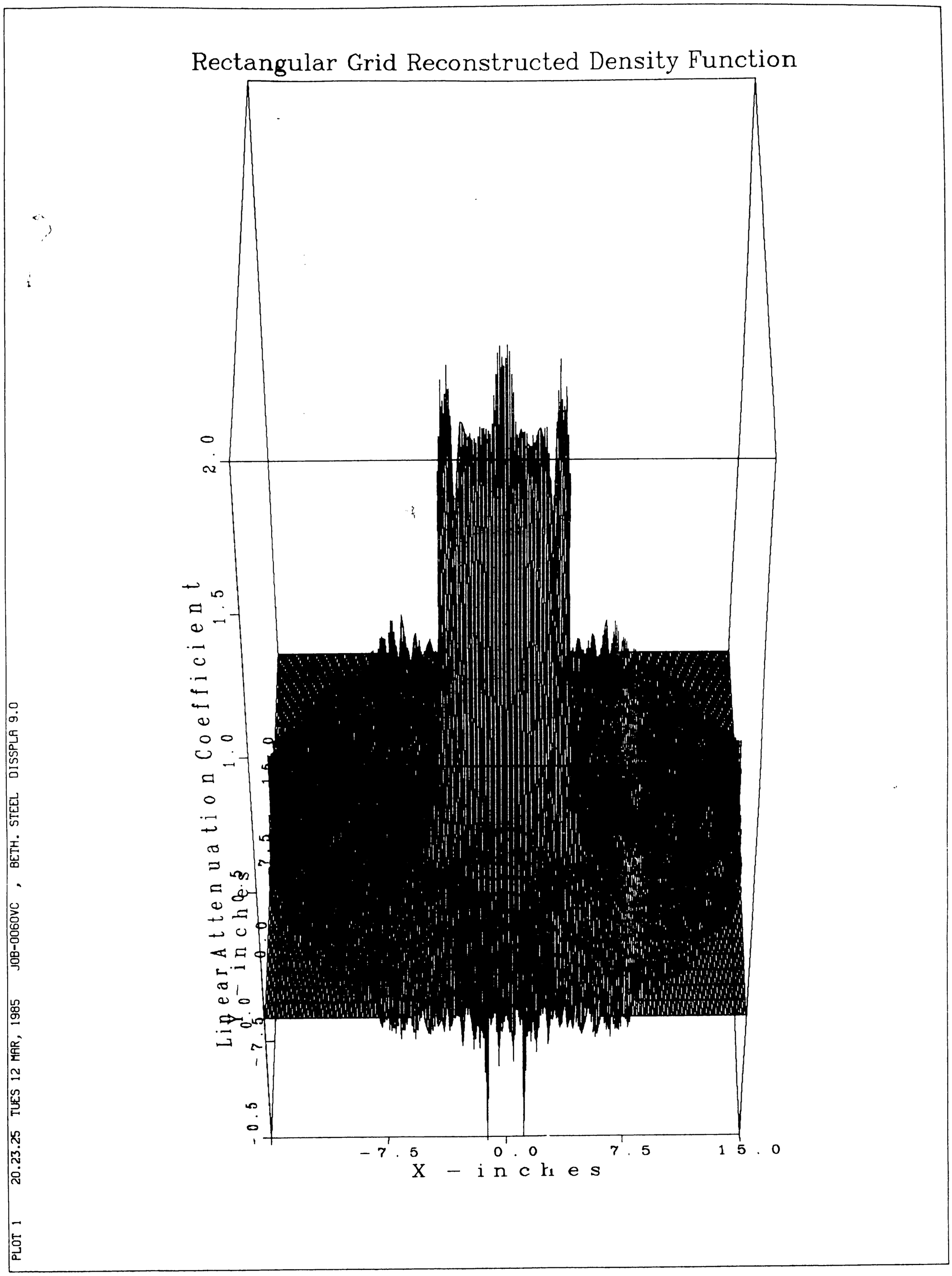
Rectangular Grid Reconstructed Density Function
Linear Attenuation Coefficient
2.0
1.5
1.0
0.5
0.0
-0.5
-7.5
0.0
7.5
15.0
Y - inches
-7.5
0.0
7.5
15.0
X - inches
PLOT 1 20.23.25 TUES 12 MAR, 1985 JOB-0060VC , BETH. STEEL DISSPLA 9.0

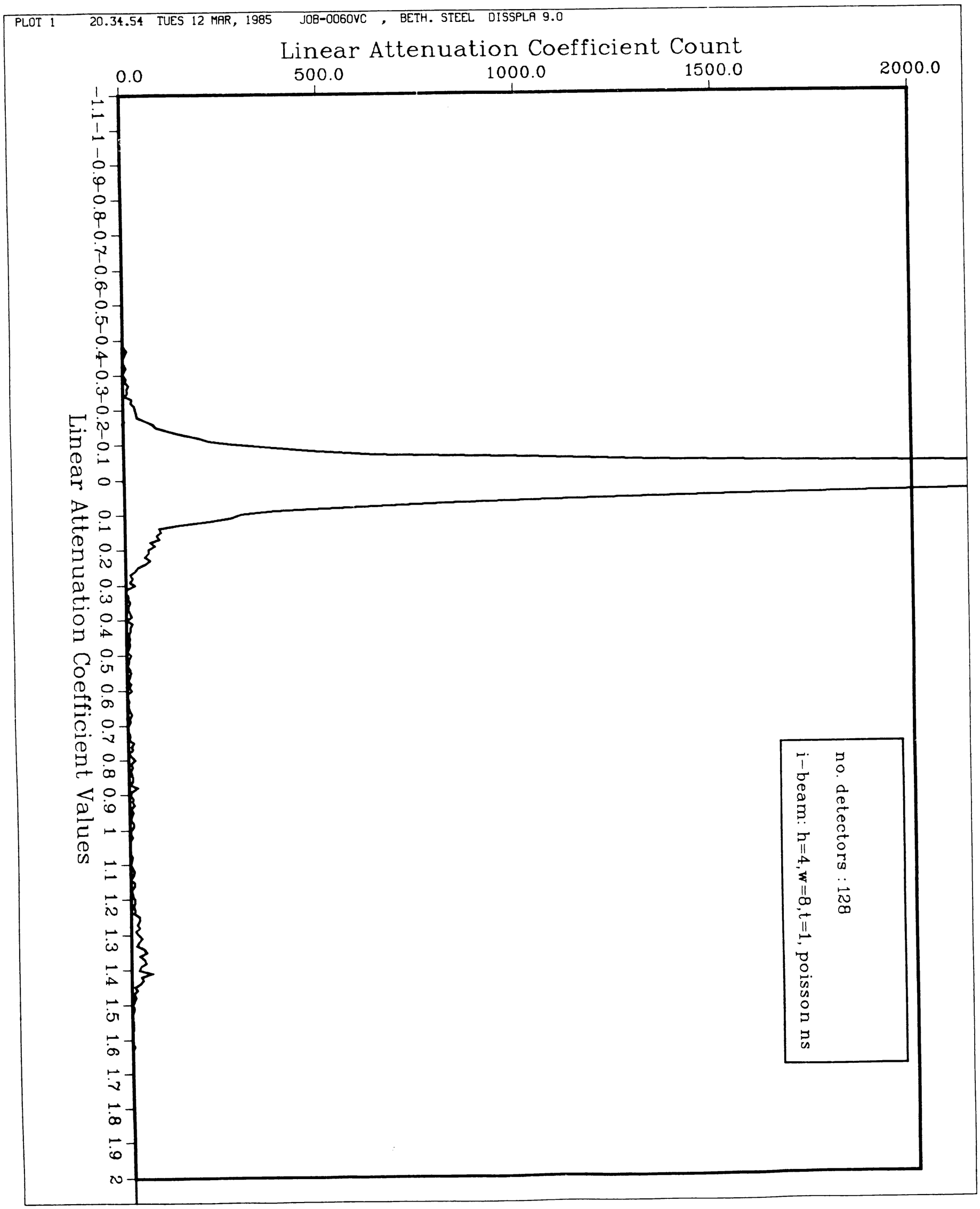
PLOT 1 20.34.54 TUES 12 MAR, 1985 JOB-0060VC , BETH. STEEL DISSPLA 9.0
Linear Attenuation Coefficient Count
0.0
500.0
1000.0
1500.0
2000.0
Linear Attenuation Coefficient Values
-1.1 -1 -0.9 -0.8 -0.7 -0.6 -0.5 -0.4 -0.3 -0.2 -0.1 0 0.1 0.2 0.3 0.4 0.5 0.6 0.7 0.8 0.9 1 1.1 1.2 1.3 1.4 1.5 1.6 1.7 1.8 1.9 2
no. detectors : 128
i-beam: h=4,w=8,t=1, poisson ns

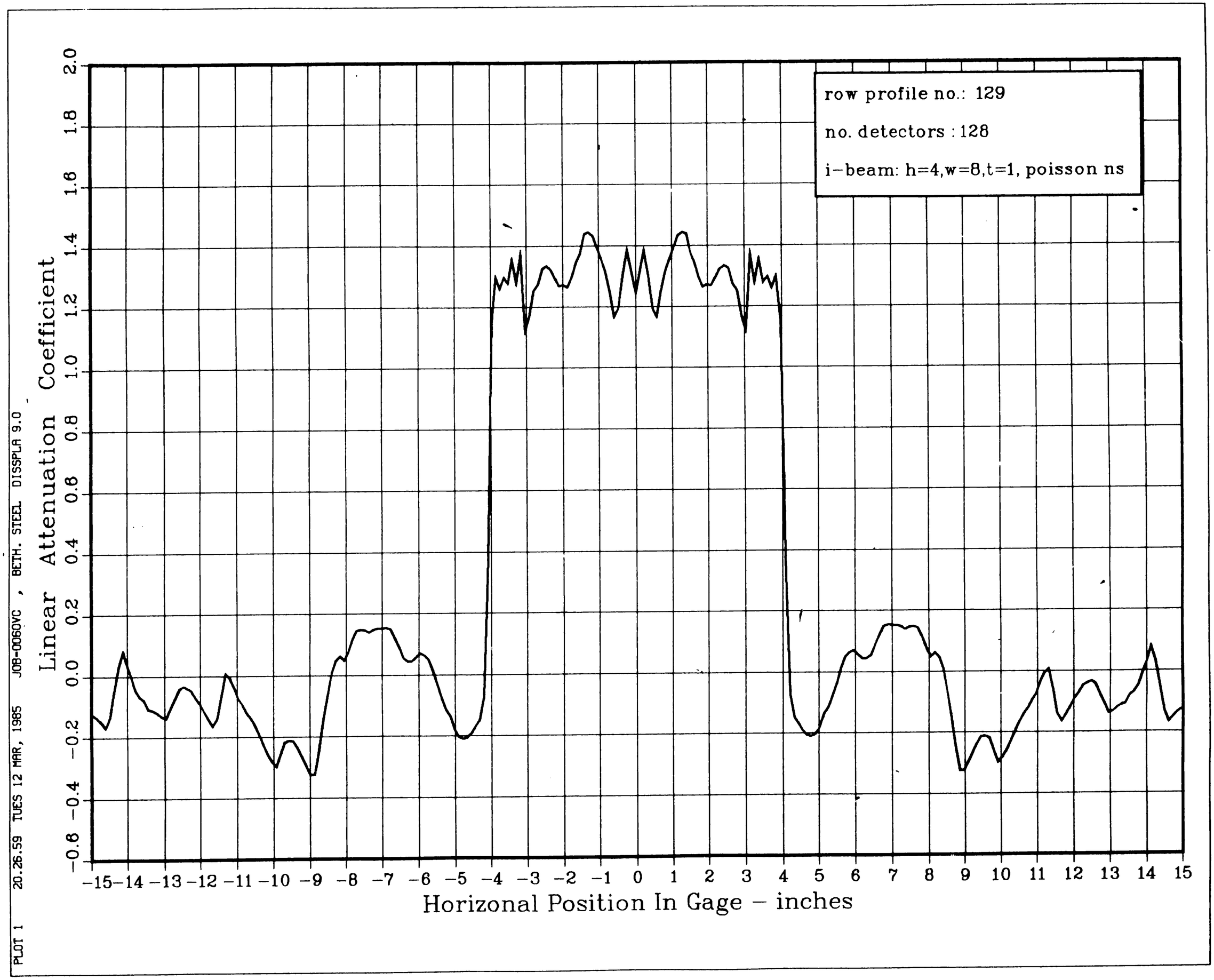
row profile no.: 129
no. detectors : 128
i-beam: h=4,w=8,t=1, poisson ns
Linear Attenuation Coefficient
Horizonal Position In Gage – inches
PLOT 1 20.26.59 TUES 12 MAR, 1985 JOB-0060VC , BETH. STEEL DISSPLA 9.0

PLOT 2 20.29.42 TUES 12 MAR, 1985 JOB-0060VC , BETH. STEEL CISSPLA 9.0

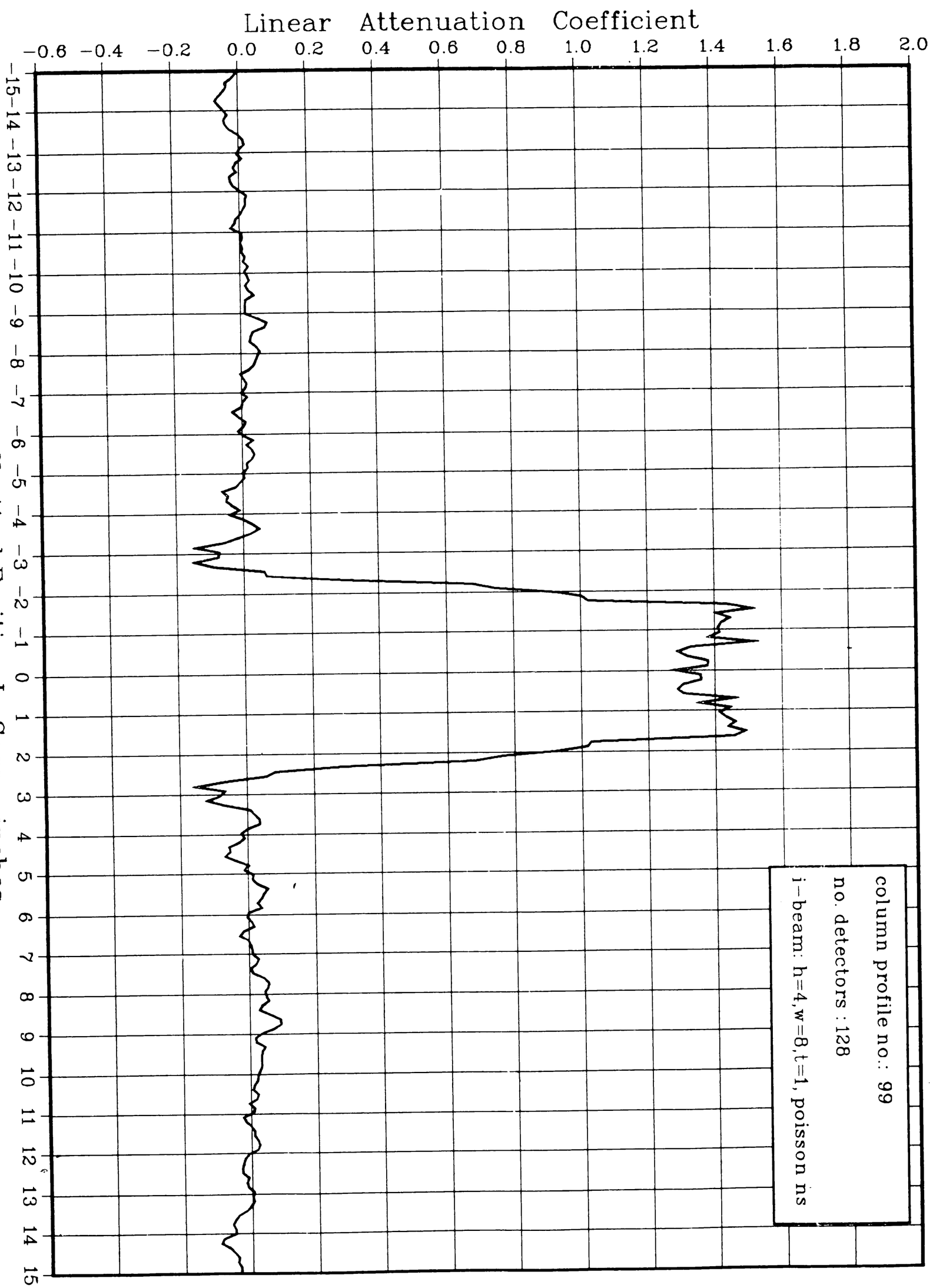

PLOT 1 20.39.20 TUES 12 MAR, 1985 JOB-0060VC , BETH. STEEL DISSPLA 9.0

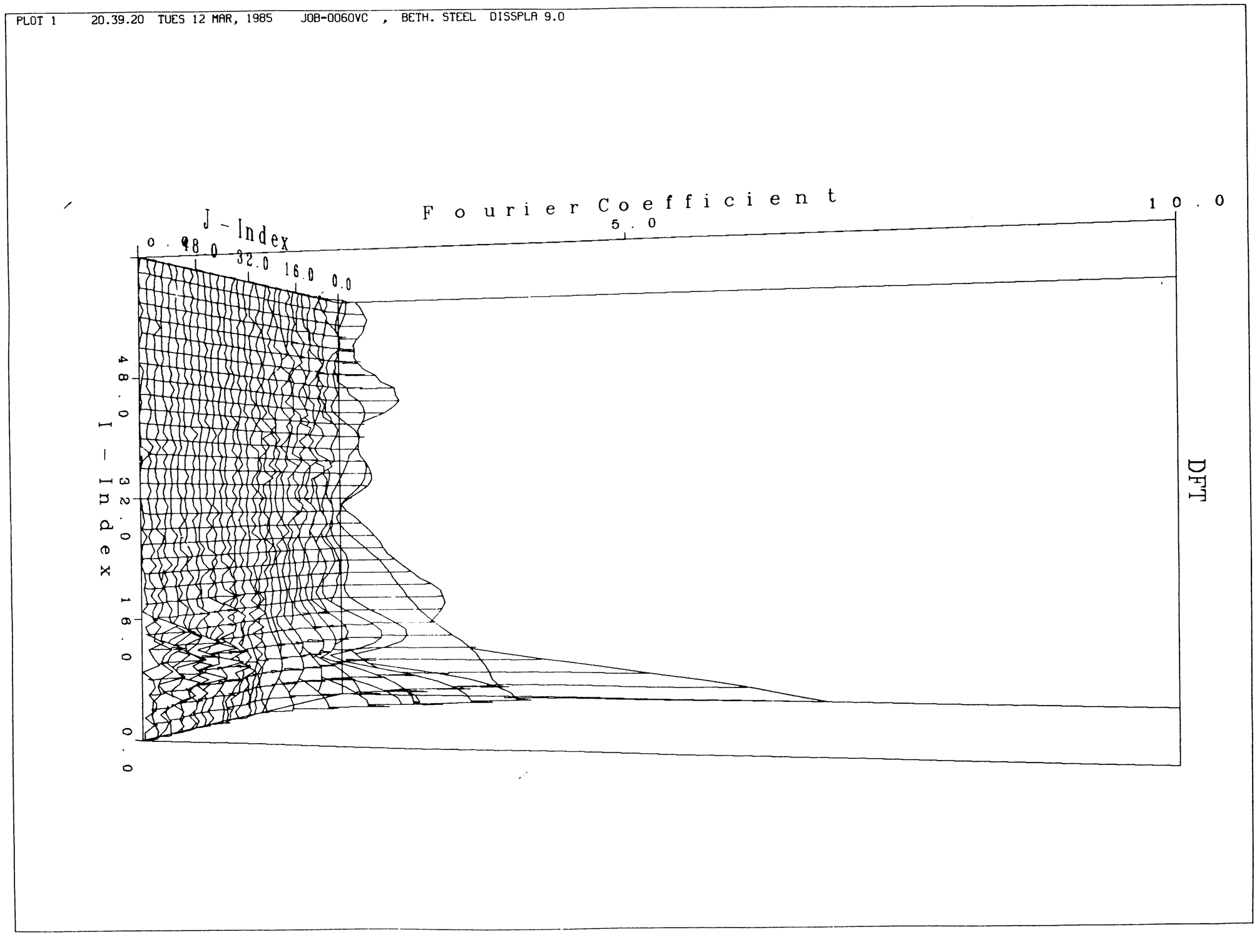

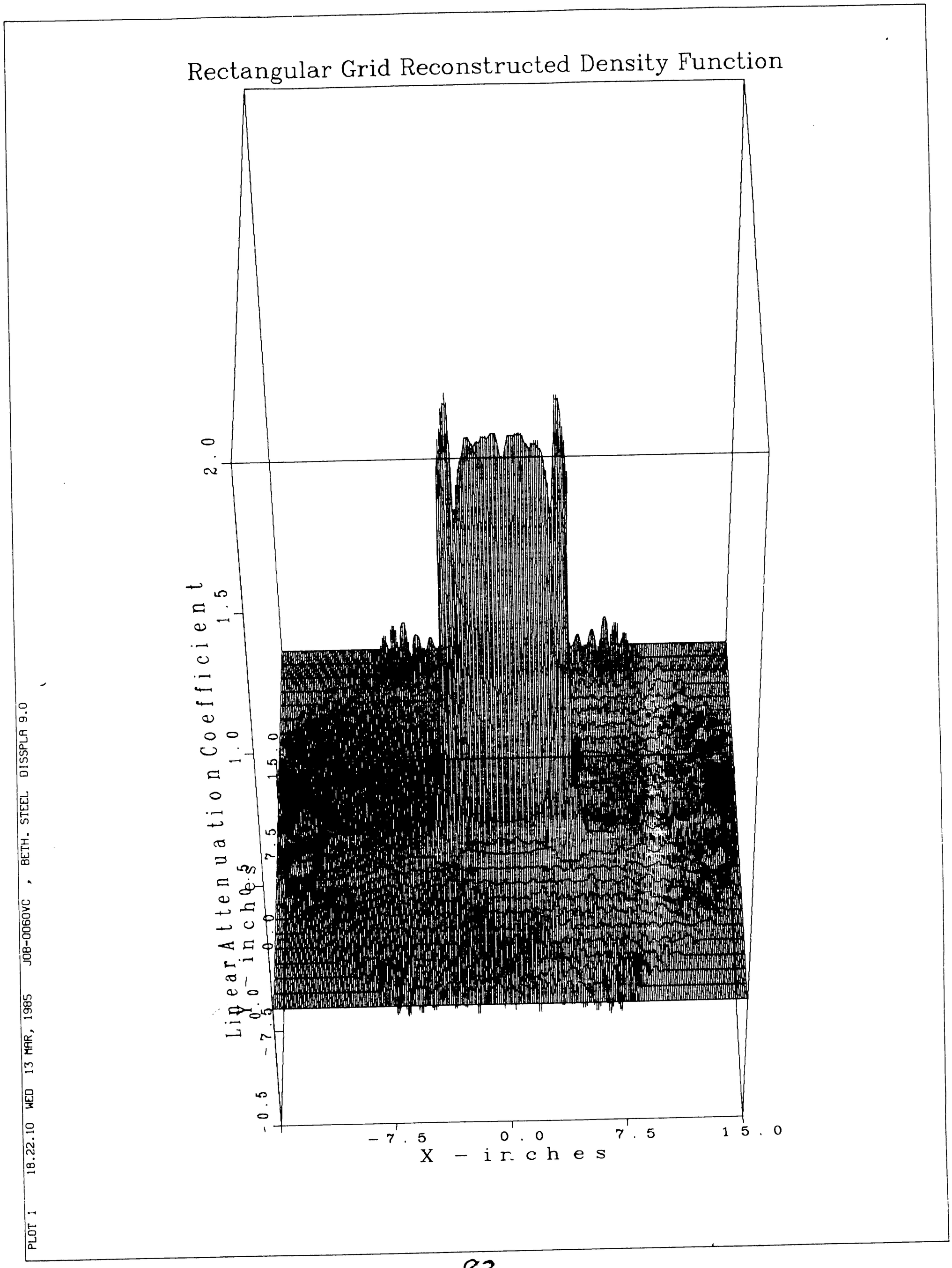
Rectangular Grid Reconstructed Density Function
Linear Attenuation Coefficient
0.0 - inches
2.0
1.5
1.0
0.5
-0.5
-7.5
0.0
7.5
15.0
X - inches
PLOT 1 18.22.10 WED 13 MAR, 1985 JOB-0060VC , BETH. STEEL DISSPLA 9.0

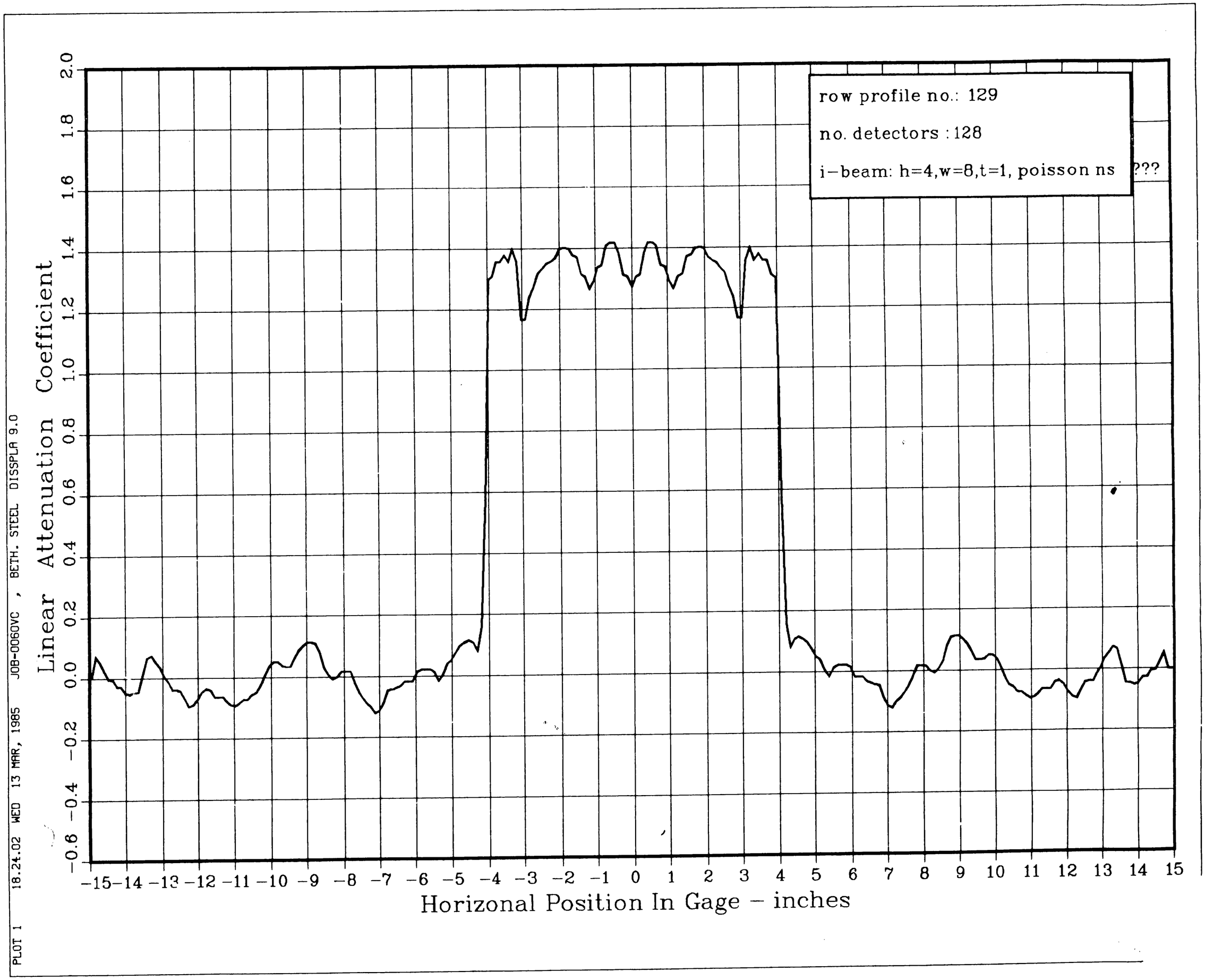

row profile no.: 129
no. detectors : 128
i-beam: h=4,w=8,t=1, poisson ns ???
Linear Attenuation Coefficient
Horizonal Position In Gage - inches
PLOT 1 18.24.02 WED 13 MAR, 1985 JOB-0060VC , BETH. STEEL DISSPLA 9.0

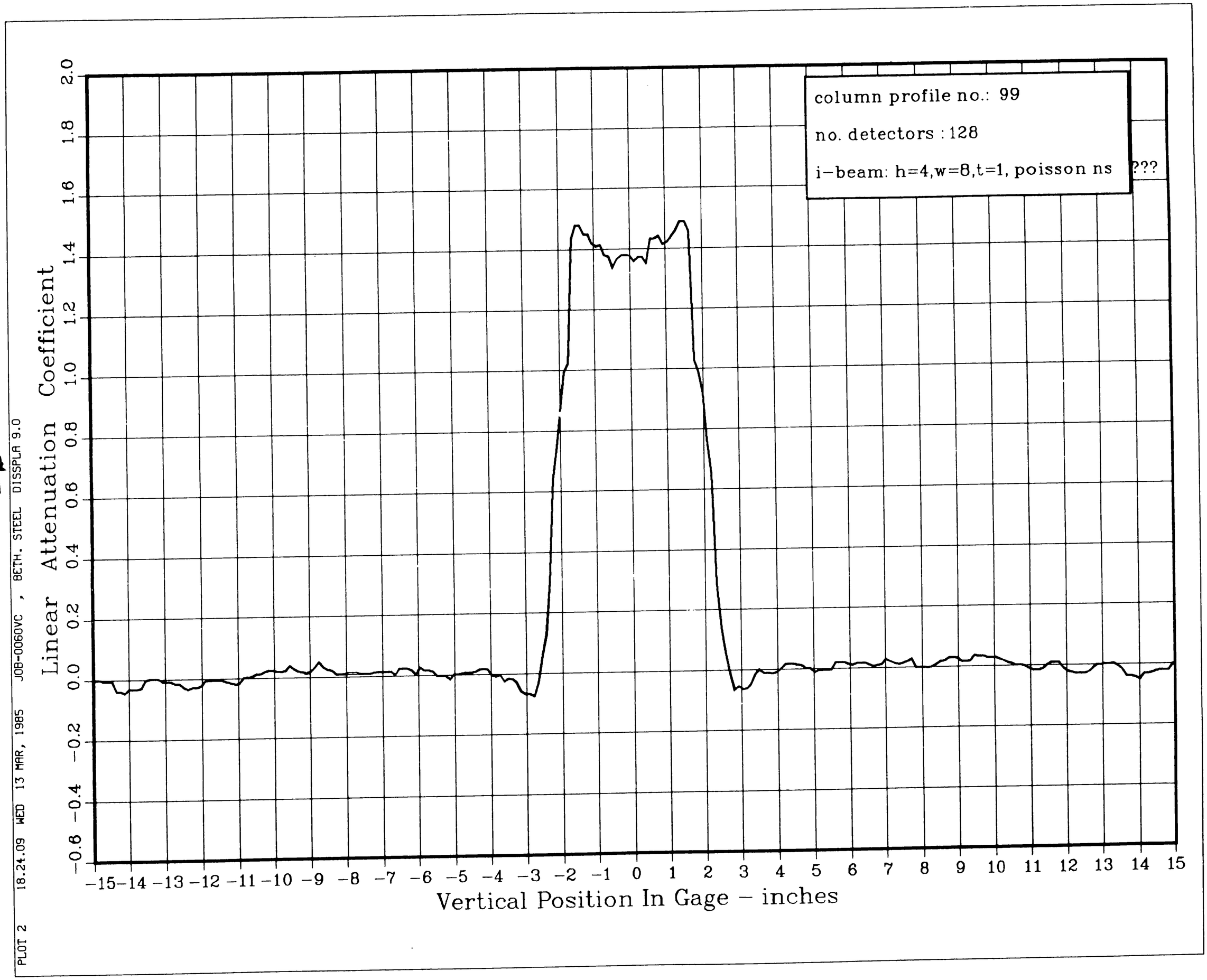
column profile no.: 99
no. detectors : 128
i-beam: h=4,w=8,t=1, poisson ns
???
Linear Attenuation Coefficient
2.0
1.8
1.6
1.4
1.2
1.0
0.8
0.6
0.4
0.2
0.0
-0.2
-0.4
-0.6
-15 -14 -13 -12 -11 -10 -9 -8 -7 -6 -5 -4 -3 -2 -1 0 1 2 3 4 5 6 7 8 9 10 11 12 13 14 15
Vertical Position In Gage - inches
PLOT 2 18.24.09 WED 13 MAR, 1985 JOB-0060VC , BETH. STEEL DISSPLA 9.0

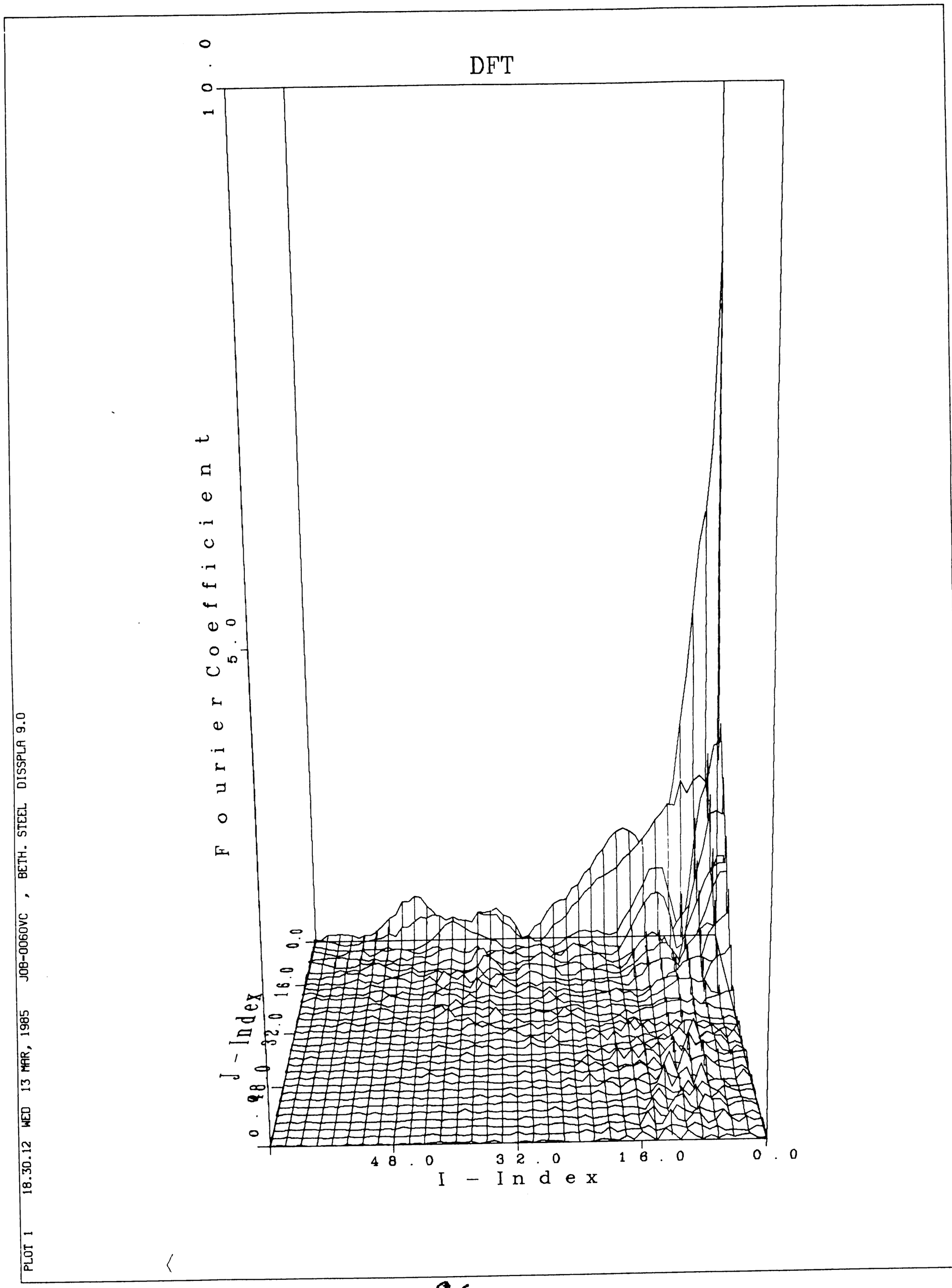
DFT
1 0 . 0
5 . 0
F o u r i e r C o e f f i c i e n t
J - Index
0 . 0
1 6 . 0
3 2 . 0
4 8 . 0
I - Index
PLOT 1 18.30.12 WED 13 MAR, 1985 JOB-0060VC , BETH. STEEL DISSPLA 9.0

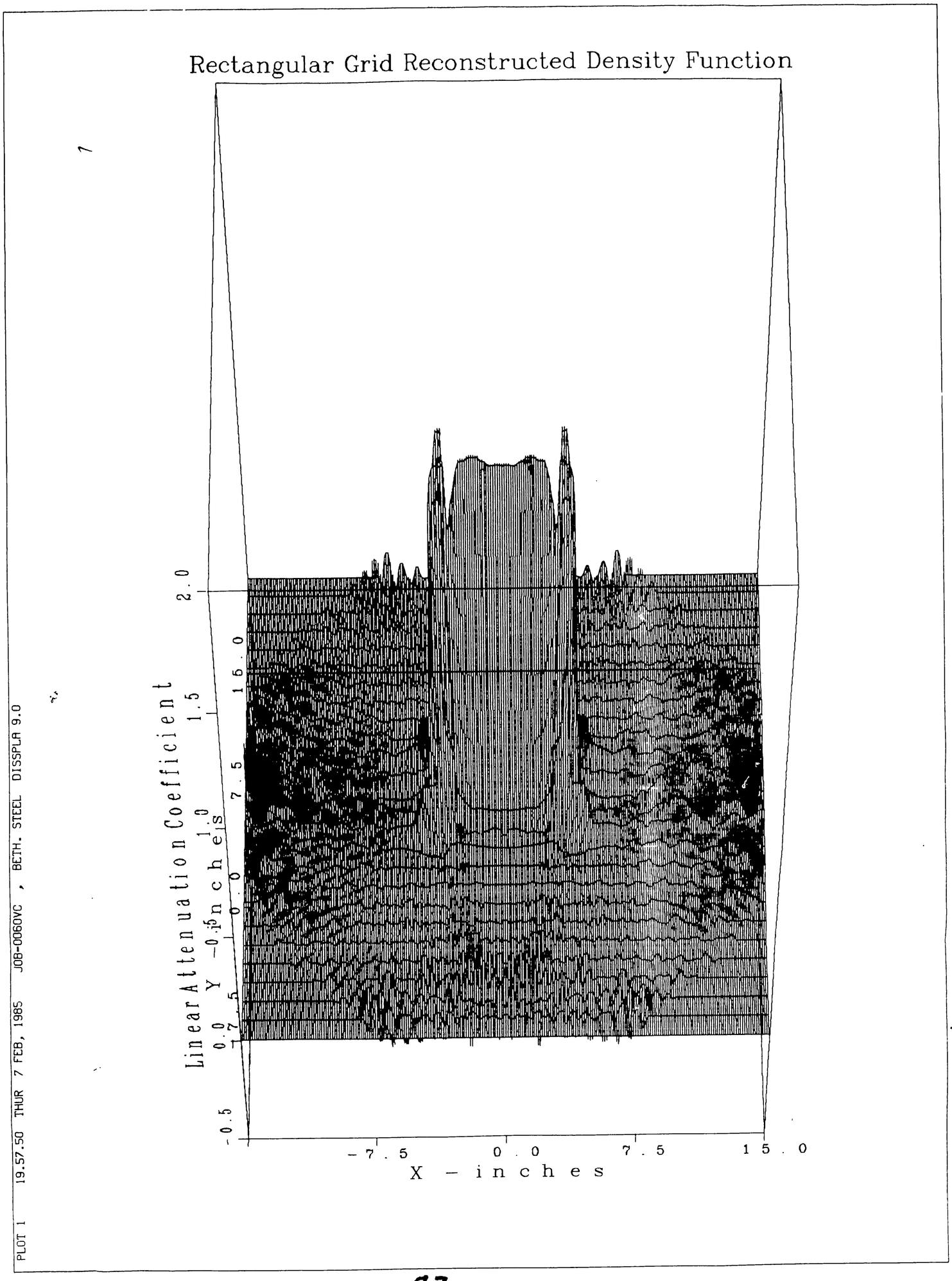
Rectangular Grid Reconstructed Density Function
Linear Attenuation Coefficient
Y - inches
X - inches
2.0
1.5
1.0
0.5
0.0
-0.5
-7.5
0.0
7.5
15.0
PLOT 1 19.57.50 THUR 7 FEB, 1985 JOB-0060VC , BETH. STEEL DISSPLA 9.0

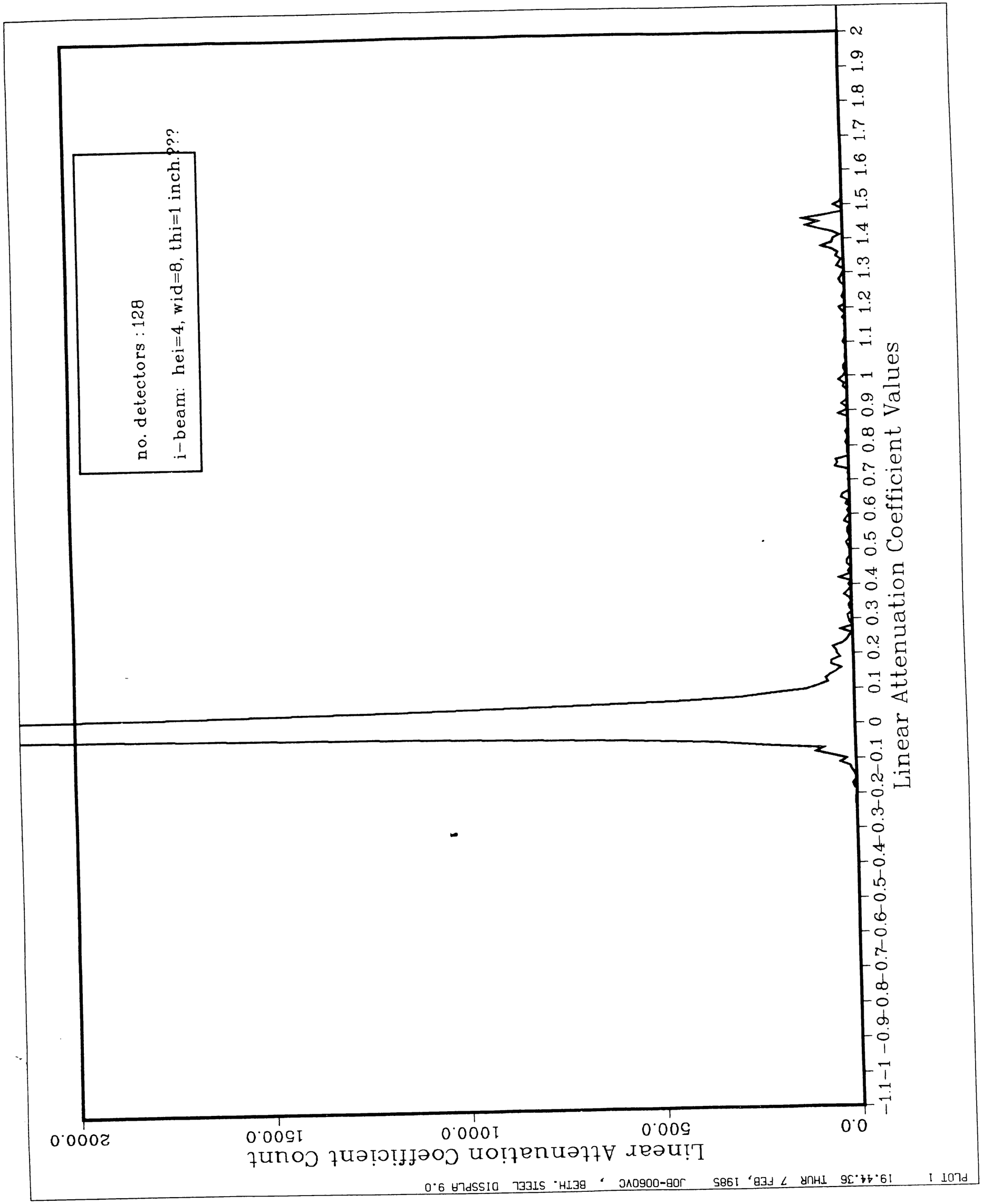
no. detectors : 128
i-beam: hei=4, wid=8, thi=1 inch. ???
Linear Attenuation Coefficient Values
−1.1 −1 −0.9 −0.8 −0.7 −0.6 −0.5 −0.4 −0.3 −0.2 −0.1 0 0.1 0.2 0.3 0.4 0.5 0.6 0.7 0.8 0.9 1 1.1 1.2 1.3 1.4 1.5 1.6 1.7 1.8 1.9 2
Linear Attenuation Coefficient Count
0.0
500.0
1000.0
1500.0
2000.0
PLOT 1 19.44.36 THUR 7 FEB, 1985 JOB-00606VC , BETH. STEEL DISSPLA 9.0

68

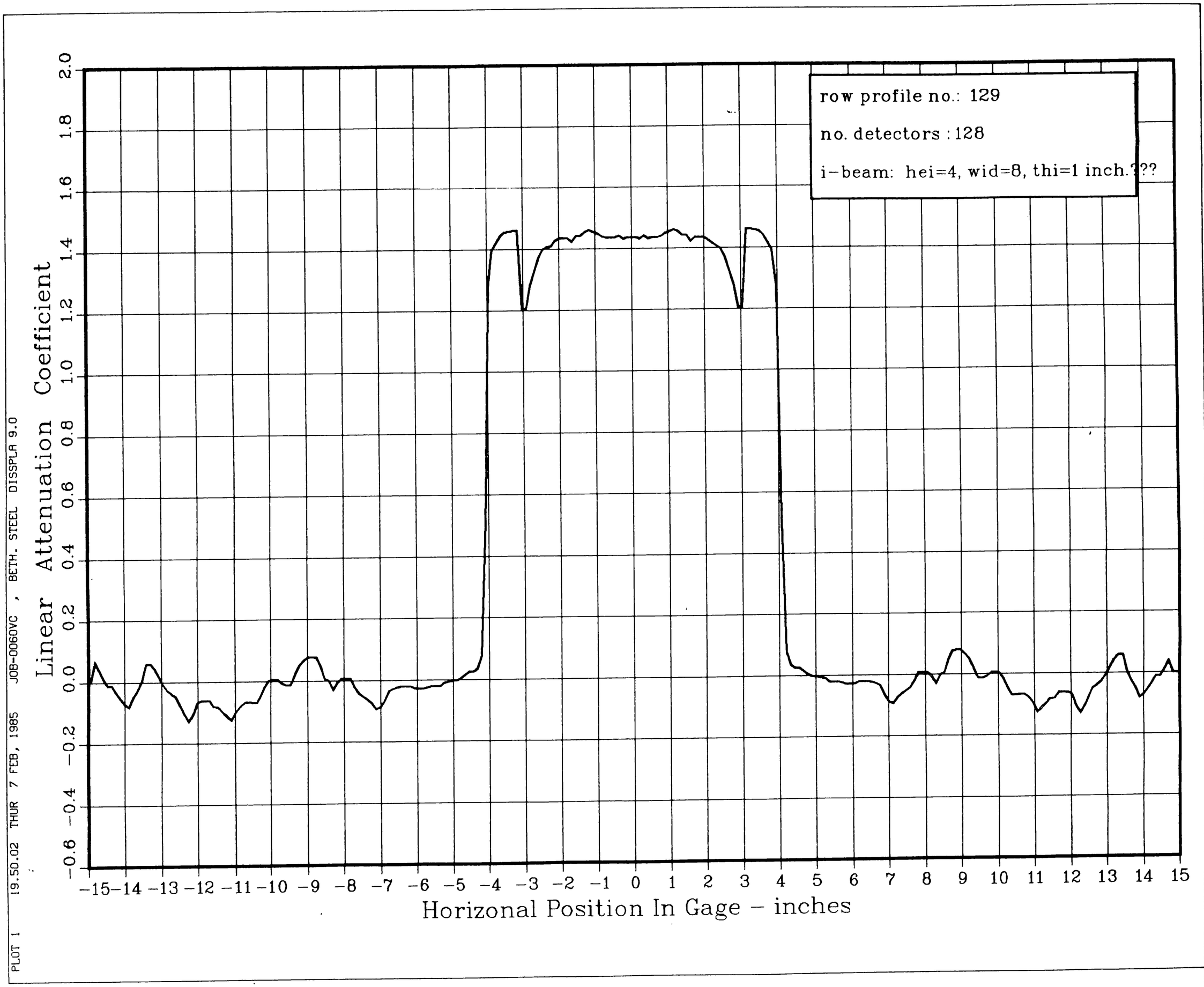
row profile no.: 129
no. detectors : 128
i-beam: hei=4, wid=8, thi=1 inch.???
Linear Attenuation Coefficient
2.0
1.8
1.6
1.4
1.2
1.0
0.8
0.6
0.4
0.2
0.0
−0.2
−0.4
−0.6
−15 −14 −13 −12 −11 −10 −9 −8 −7 −6 −5 −4 −3 −2 −1 0 1 2 3 4 5 6 7 8 9 10 11 12 13 14 15
Horizonal Position In Gage − inches
PLOT 1 19.50.02 THUR 7 FEB, 1985 JOB-0060VC , BETH. STEEL DISSPLA 9.0

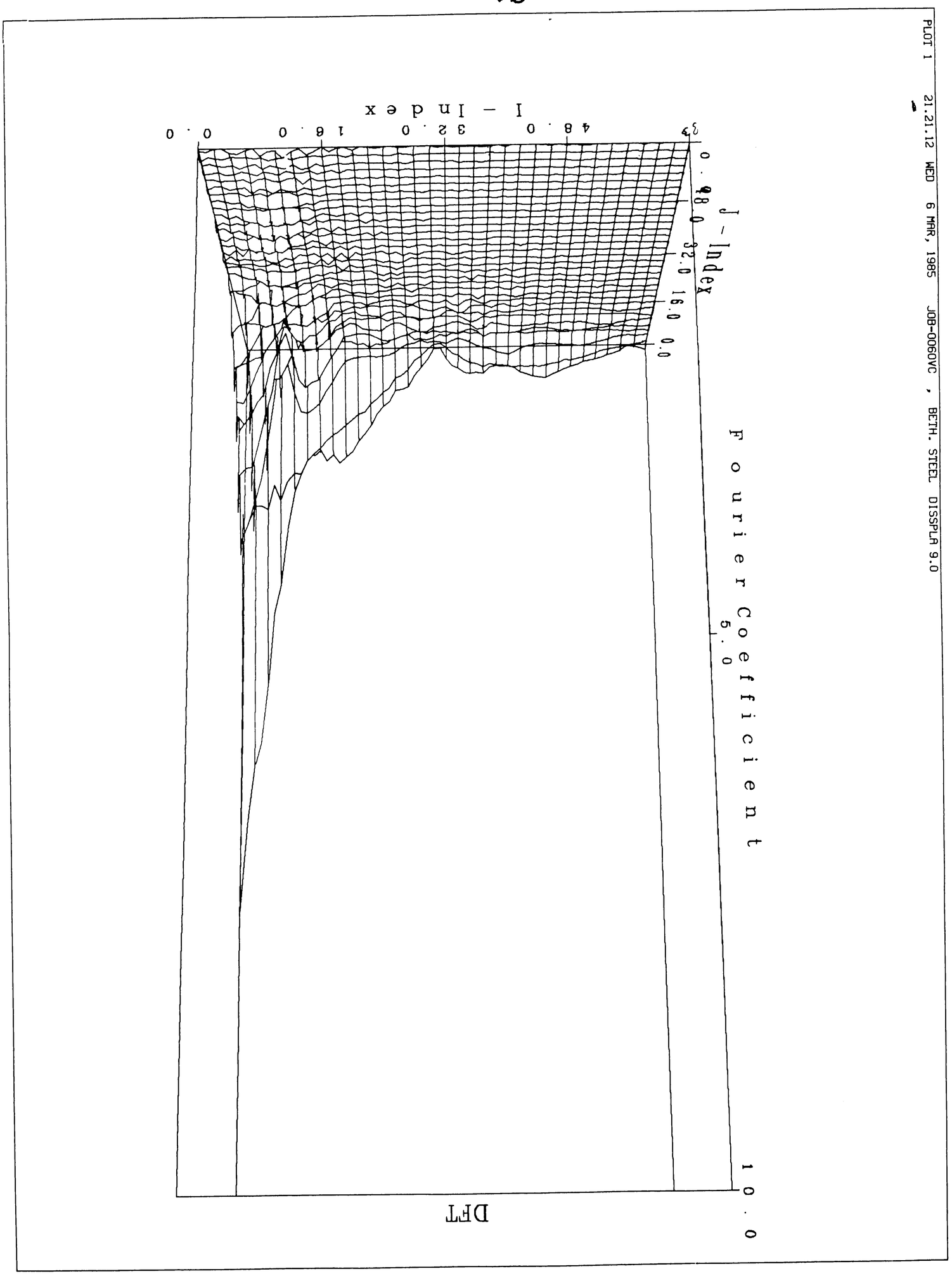
PLOT 1 21.21.12 WED 6 MAR, 1985 JOB-0060VC , BETH. STEEL DISSPLA 9.0
I - Index
0.0
16.0
32.0
48.0
J - Index
0.0
5.0
10.0
Fourier Coefficient
DFT

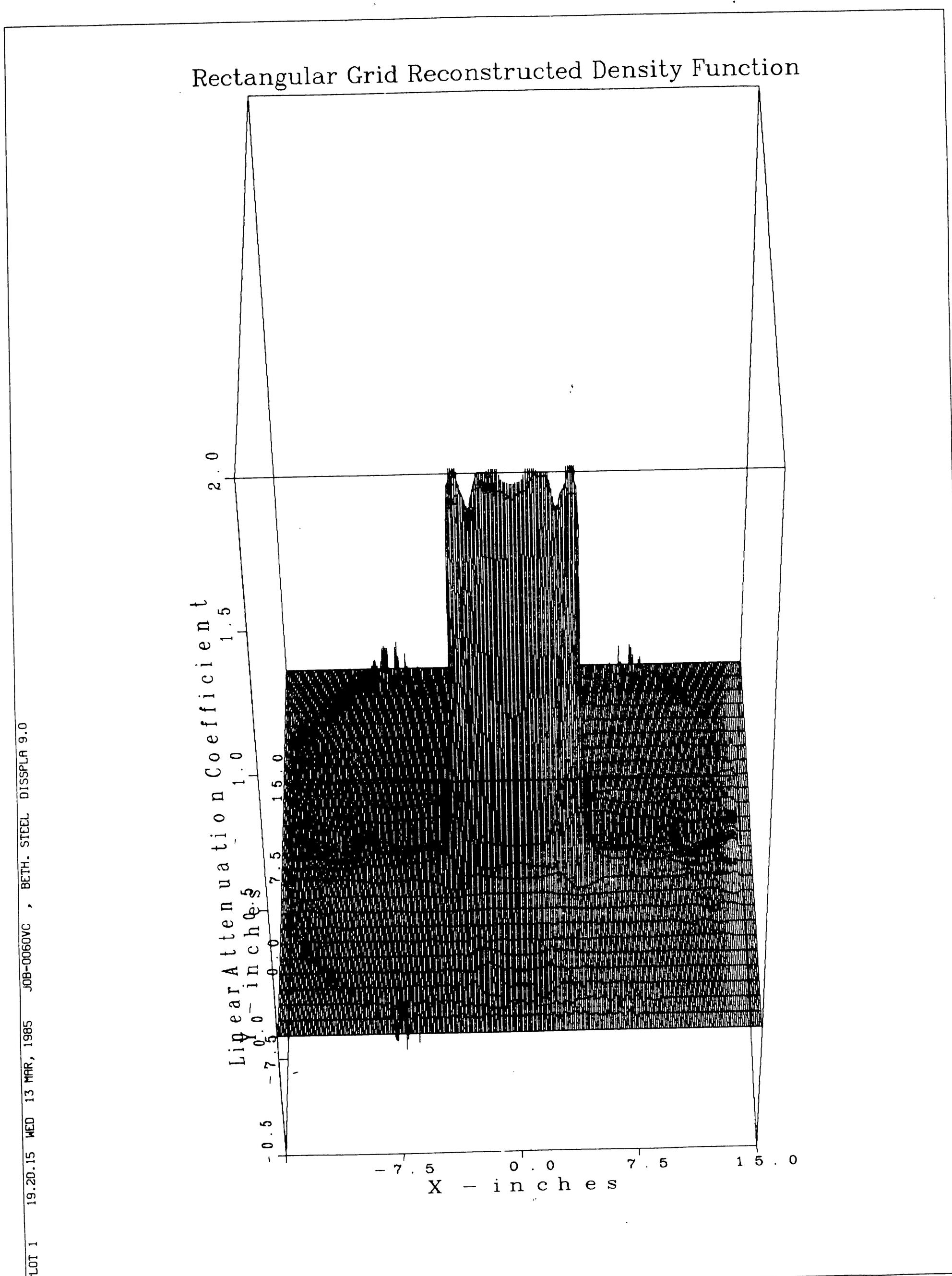
Rectangular Grid Reconstructed Density Function
Linear Attenuation Coefficient
2.0
1.5
1.0
0.5
0.0
-0.5
Y - inches
-7.5
0.0
7.5
15.0
X - inches
PLOT 1 19.20.15 WED 13 MAR, 1985 JOB-0060VC , BETH. STEEL DISSPLA 9.0

PLOT 1 19.24.34 WED 13 MAR, 1985 JOB-0060VC , BETH. STEEL DISSPLA 9.0

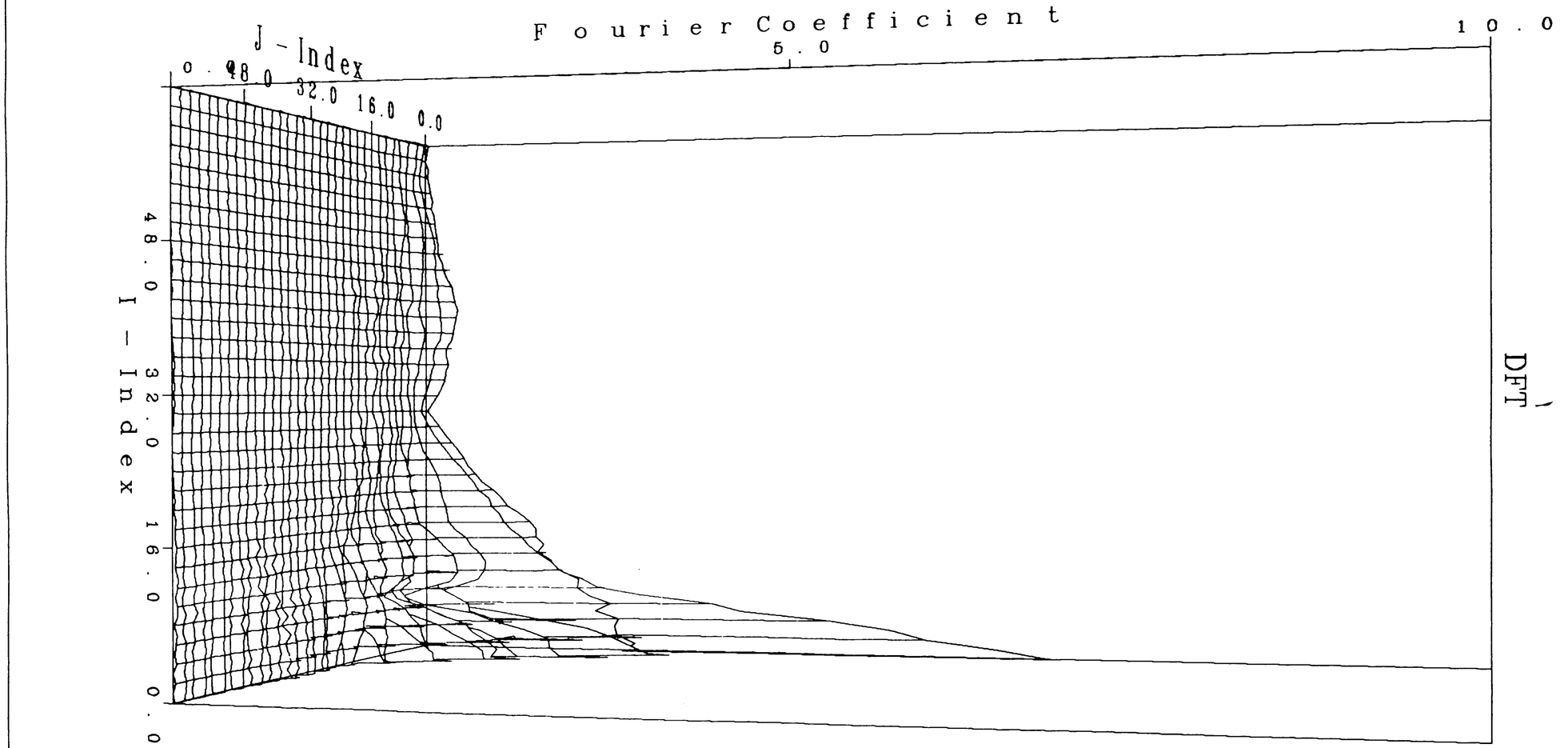

42

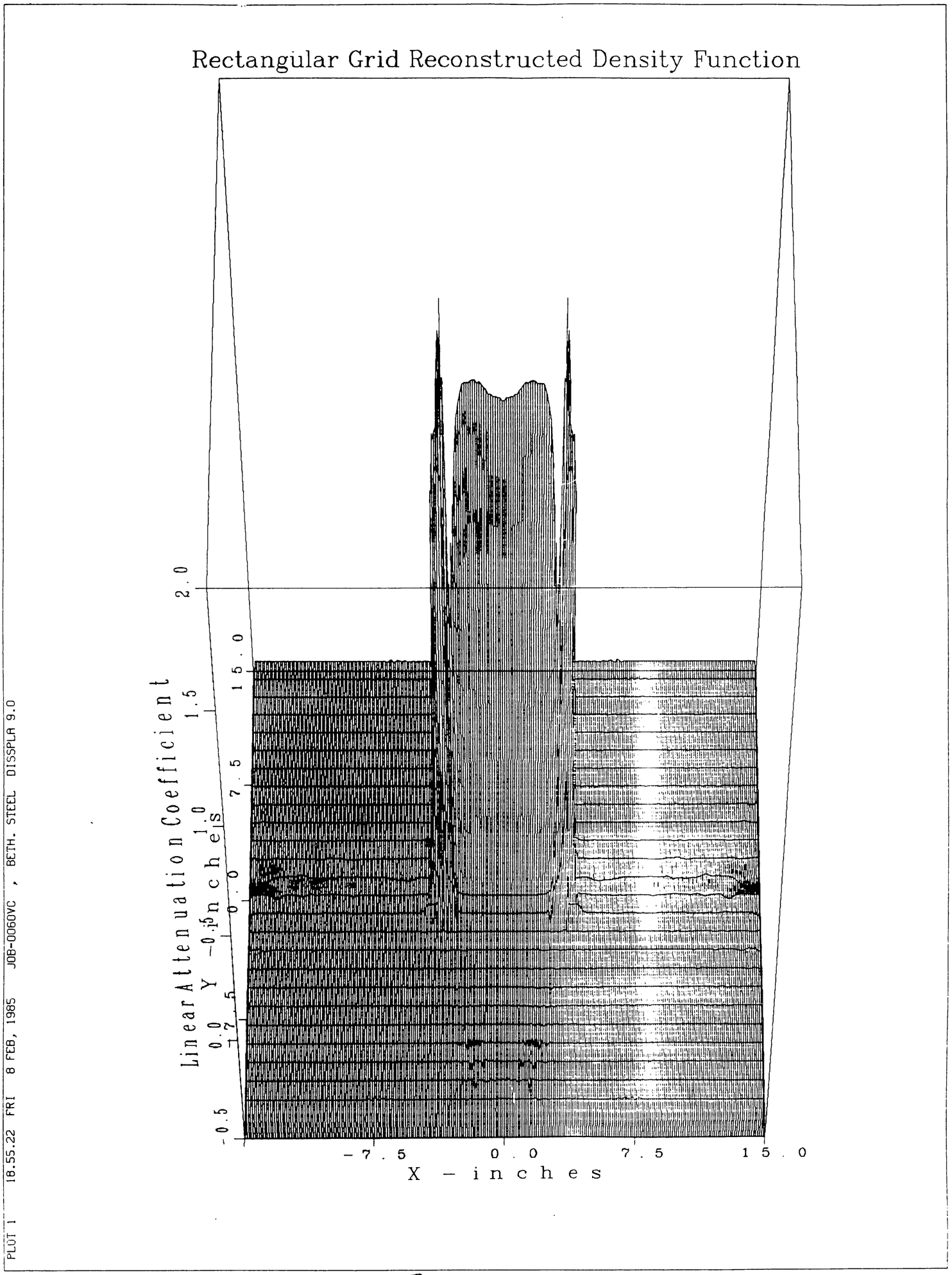
Rectangular Grid Reconstructed Density Function
Linear Attenuation Coefficient
2.0
1.5
1.0
0.5
0.0
-0.5
Y - inches
15.0
7.5
0.0
-7.5
X - inches
PLOT 1 18.55.22 FRI 8 FEB, 1985 JOB-0060VC , BETH. STEEL DISSPLA 9.0

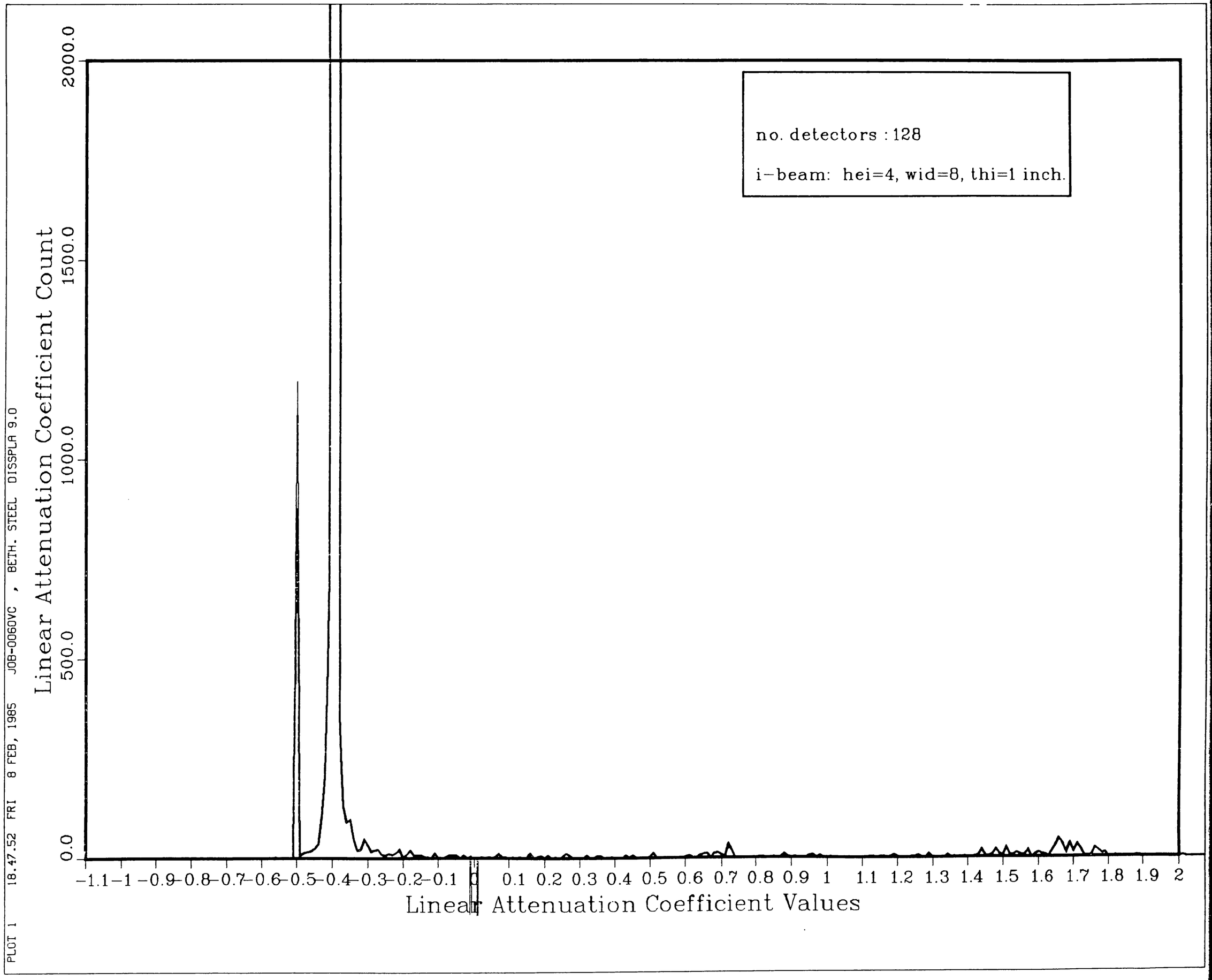
no. detectors : 128
i-beam: hei=4, wid=8, thi=1 inch.
Linear Attenuation Coefficient Count
0.0
500.0
1000.0
1500.0
2000.0
-1.1 -1 -0.9 -0.8 -0.7 -0.6 -0.5 -0.4 -0.3 -0.2 -0.1 0 0.1 0.2 0.3 0.4 0.5 0.6 0.7 0.8 0.9 1 1.1 1.2 1.3 1.4 1.5 1.6 1.7 1.8 1.9 2
Linear Attenuation Coefficient Values
PLOT 1 18.47.52 FRI 8 FEB, 1985 JOB-0060VC , BETH. STEEL DISSPLA 9.0

5b

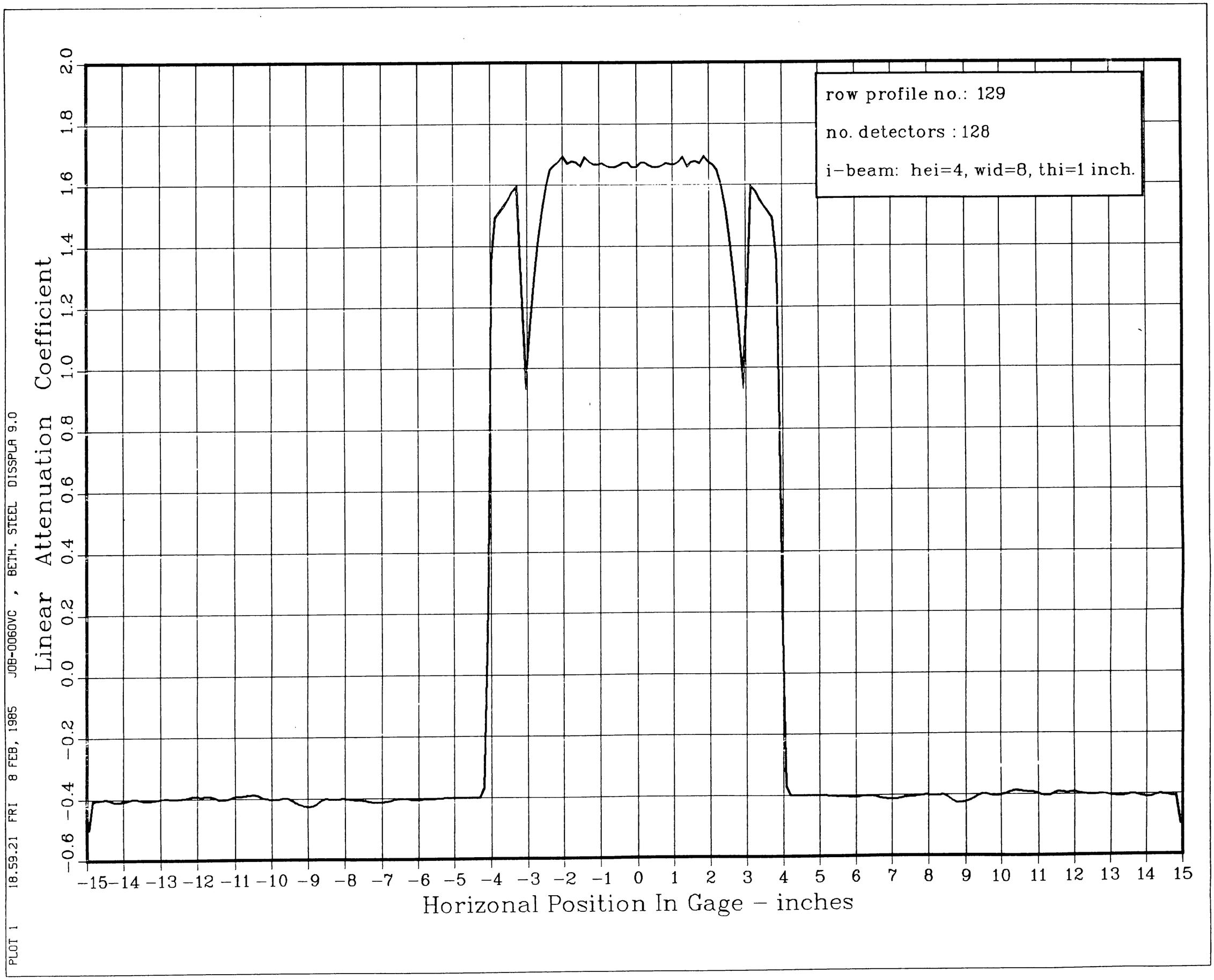
row profile no.: 129
no. detectors : 128
i-beam: hei=4, wid=8, thi=1 inch.
Linear Attenuation Coefficient
2.0
1.8
1.6
1.4
1.2
1.0
0.8
0.6
0.4
0.2
0.0
−0.2
−0.4
−0.6
−15 −14 −13 −12 −11 −10 −9 −8 −7 −6 −5 −4 −3 −2 −1 0 1 2 3 4 5 6 7 8 9 10 11 12 13 14 15
Horizonal Position In Gage − inches
PLOT 1 18.59.21 FRI 8 FEB, 1985 JOB-0060VC , BETH. STEEL DISSPLA 9.0

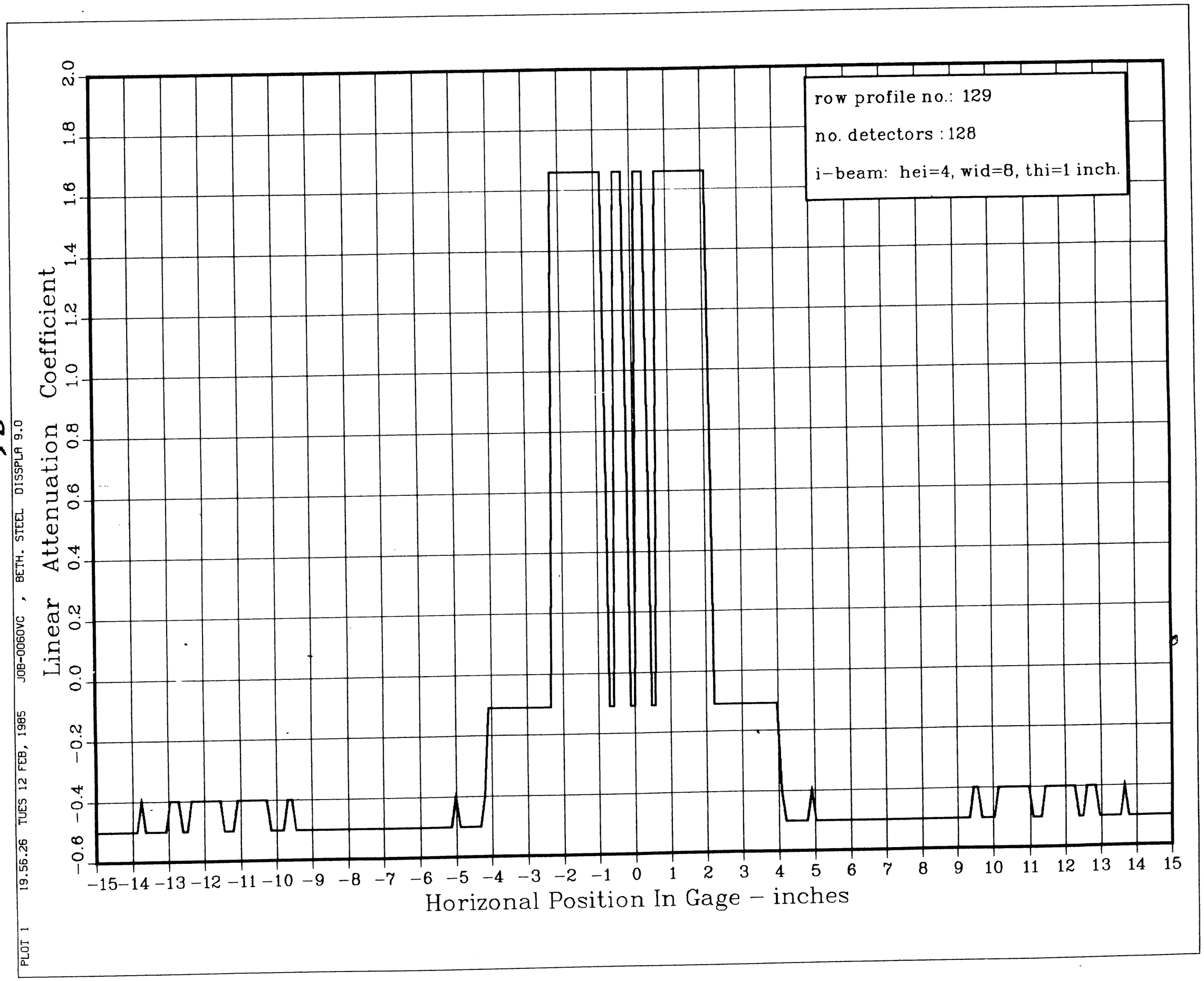

row profile no.: 129
no. detectors : 128
i-beam: hei=4, wid=8, thi=1 inch.
Linear Attenuation Coefficient
Horizonal Position In Gage - inches
PLOT 1 19.56.26 TUES 12 FEB, 1985 JOB-0060VC , BETH. STEEL DISSPLA 9.0

96

Appendix C
Graphs of Image iii

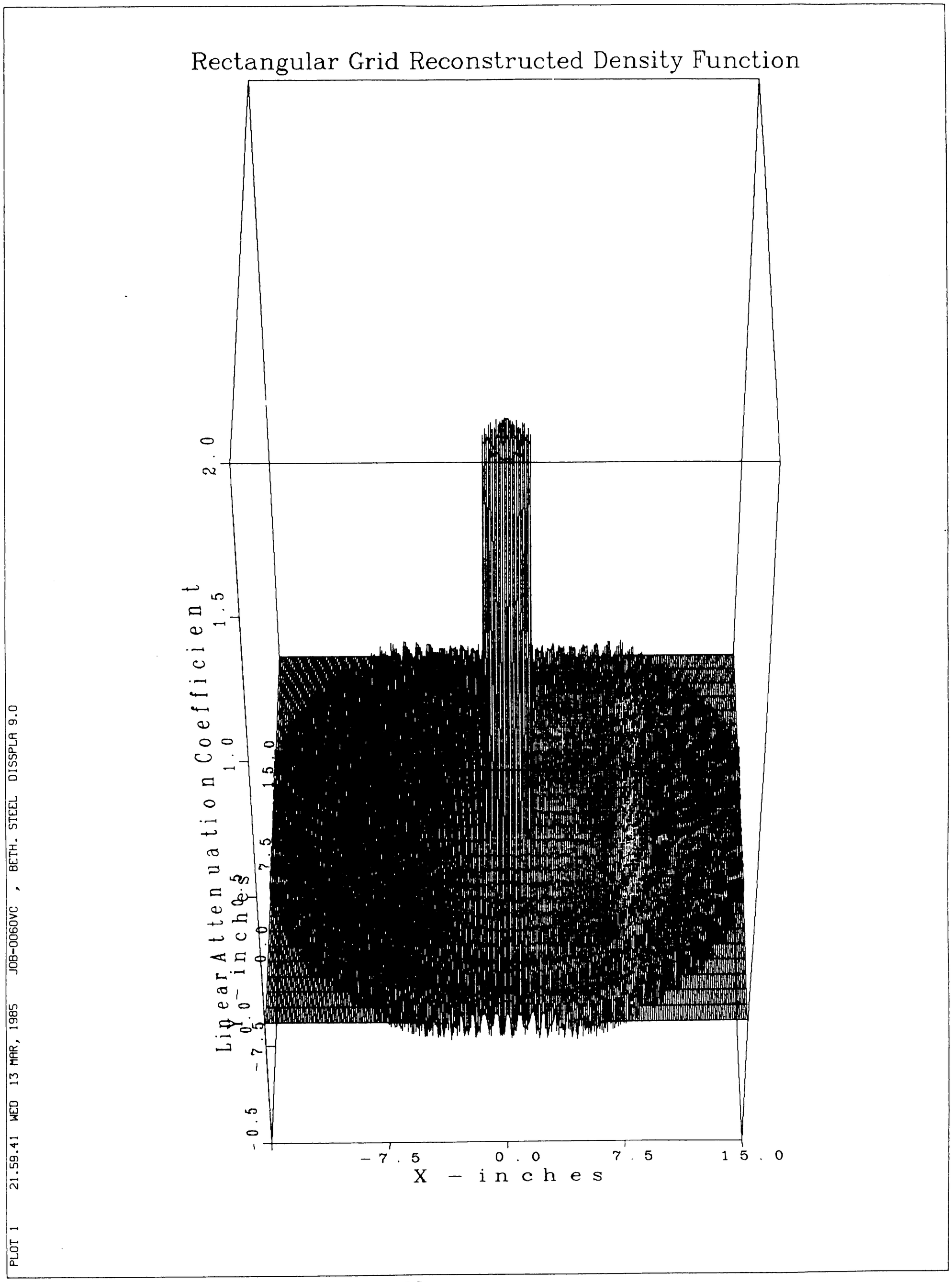
Rectangular Grid Reconstructed Density Function
Linear Attenuation Coefficient
2.0
1.5
1.0
0.5
0.0
-0.5
-7.5
0.0
7.5
15.0
Y - inches
-7.5
0.0
7.5
15.0
X - inches
PLOT 1 21.59.41 WED 13 MAR, 1985 JOB-0060VC , BETH. STEEL DISSPLA 9.0

bb

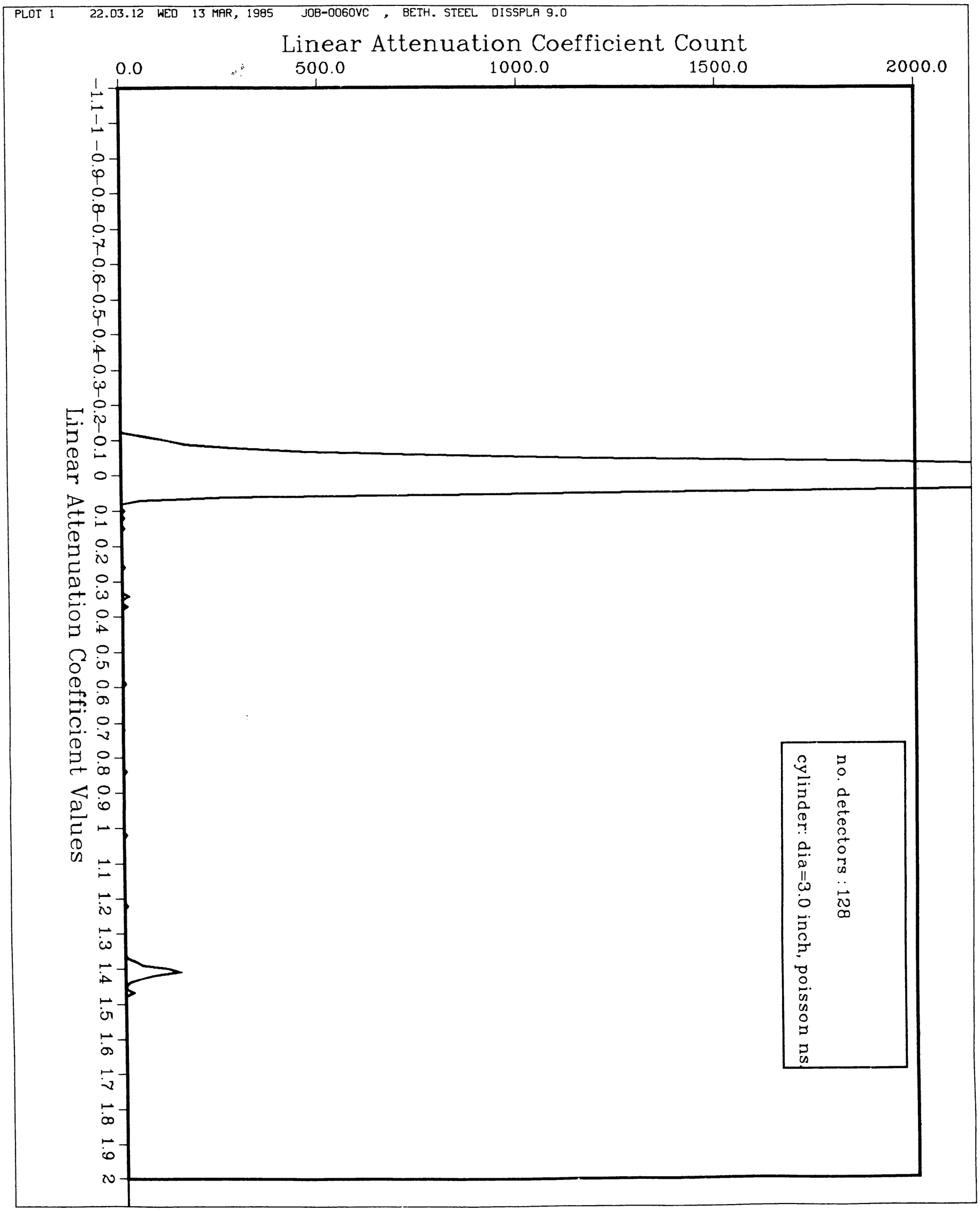
PLOT 1 22.03.12 WED 13 MAR, 1985 JOB-0060VC , BETH. STEEL DISSPLA 9.0
Linear Attenuation Coefficient Count
0.0
500.0
1000.0
1500.0
2000.0
Linear Attenuation Coefficient Values
-1.1 -1 -0.9 -0.8 -0.7 -0.6 -0.5 -0.4 -0.3 -0.2 -0.1 0 0.1 0.2 0.3 0.4 0.5 0.6 0.7 0.8 0.9 1 1.1 1.2 1.3 1.4 1.5 1.6 1.7 1.8 1.9 2
no. detectors : 128
cylinder: dia=3.0 inch, poisson ns

row profile no.: 129

no. detectors : 128

cylinder: dia=3.0 inch, poisson ns.

Linear Attenuation Coefficient

2.0
1.8
1.6
1.4
1.2
1.0
0.8
0.6
0.4
0.2
0.0
−0.2
−0.4
−0.6

−15 −14 −13 −12 −11 −10 −9 −8 −7 −6 −5 −4 −3 −2 −1 0 1 2 3 4 5 6 7 8 9 10 11 12 13 14

Horizonal Position In Gage − inches

PLOT 1 22.01.50 WED 13 MAR, 1985 JOB-0060VC , BETH. STEEL DISSPLA 9.0

PLOT 1 22.08.41 WED 13 MAR, 1985 JOB-0060VC , BETH. STEEL DISSPLA 9.0

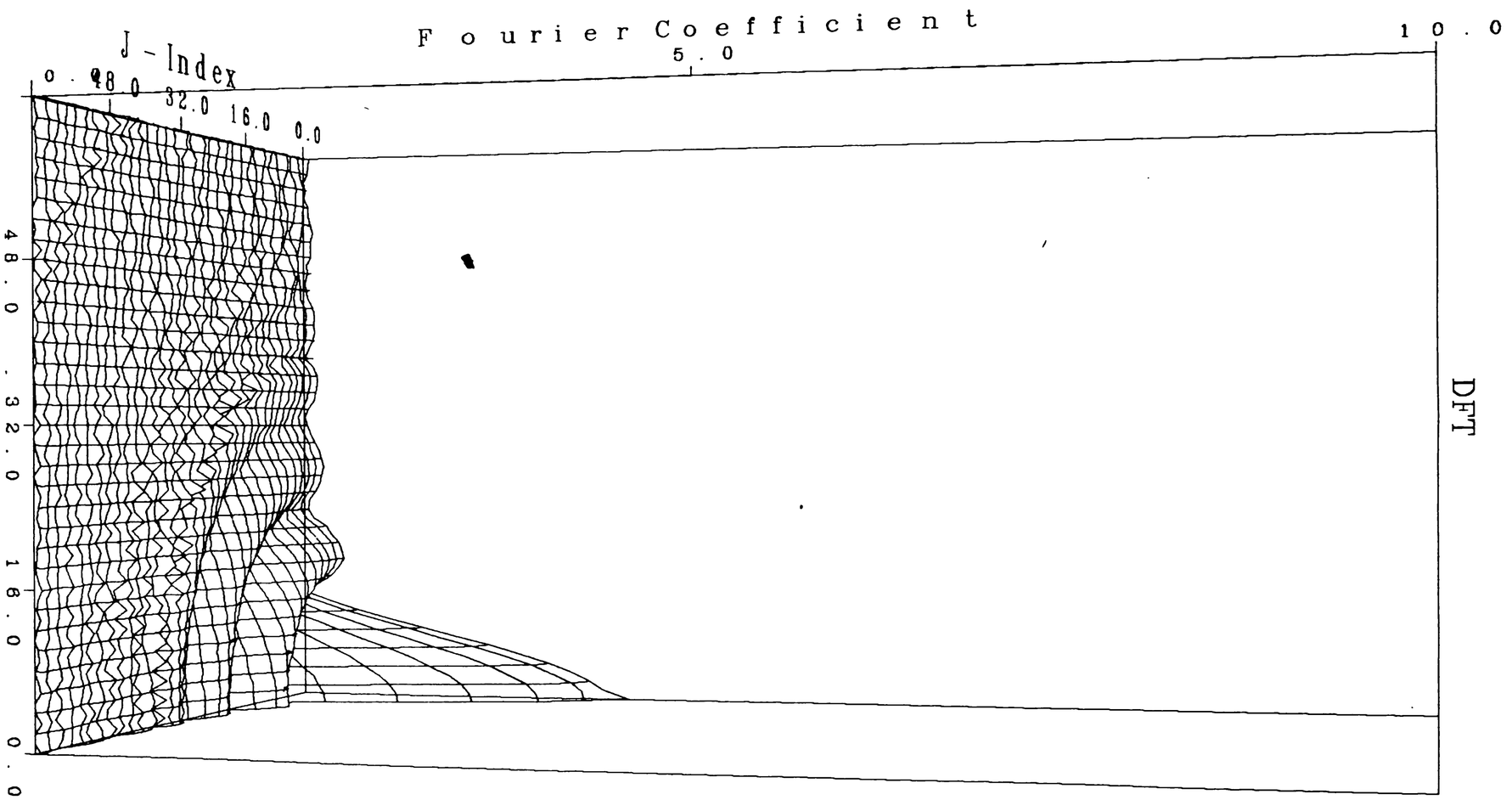

191

Vita

I was born in Harrisburg, Pennsylvania on November 11, 1955 to Daniel and Veronica Calderon.

I attended Millersville State College receiving a Bachelor of Arts in Mathematics in 1977. I attended Lehigh University receiving a Masters of Science in Electrical Engineering in 1985.